AN ABSTRACT OF THE DISSERTATION OF

Lauren Fullmer for the degree of Doctor of Philosophy in Chemistry presented on November 1, 2016.

Title: Exploring the Distinct Solution Behavior of Isostructural Polycoltanates

Abstract approved:

_____

May Nyman

Polyoxometalates are a rapidly growing class of discrete metal oxide clusters with a wide range of applications including functional materials. These anionic clusters of the group V and VI transition metals are inexpensive and non-toxic. Within group V polyoxometalates, niobium and tantalum chemistry has been underdeveloped owing to their unique solubility and speciation in alkaline conditions compared to the acidic group VI polyoxometalates. This thesis compares the solution behavior of analogous hexacoltanate structures $[Ta_6O_{19}]^{8-}$ and $[Nb_6O_{19}]^{8-}$, their association with counterions, and their potential as thin film precursors. Tetramethylammonium hexametalate salts, $[(CH_3)_4N]_{(8-x)}H_xM_6O_{19}$, have been synthesized in an effort to provide a metal-oxide thin film precursor without incorporating counterions into the final film composition. These structurally identical analogues differ only by a single proton, which affects the behavior of these clusters in solution and in turn, the quality of the thin films that are obtained. Furthermore, these tetramethylammonium hexametalates react with hydrogen peroxide, exchanging terminal multiply bound oxygens with peroxide which yields $[(CH_3)_4N]_{(8-x)}[H_xM_6(O_2)_6O_{13}]$. Small and wide angle x-ray scattering is utilized

to analyze the hexametalates in solution and determine any interactions between these highly charged species. Polyoxometalates are ideal to study with x-ray scattering since the high Z metals in the cluster provide excellent electron density contrast with low Z solvents such as water. We observe differences in the solution behavior, indicating that hexatantalate and hexaniobate are not as similar as originally expected. Density functional theory calculations have determined the energetics of peroxide addition as well as preferred sites for substitution. This thesis also compares the ion association of the alkali salts of niobium and tantalum hexametalates. The association of clusters with their counterions precedes crystallization and is therefore an important step in structure elucidation. Hexacoltanates exhibit increased solubility with increased ion association, making them an ideal study to understand the fundamentals of ion pairing. Small and wide angle x-ray scattering as well as conductivity are utilized to investigate ion association as a function of counterion, concentration, solvent polarity, and niobium vs. tantalum. Overall, we observe increased ion association with decreasing solvent polarity. While the increasing ion association with increasing alkali size is expected for hexaniobate, there are some discrepancies with hexatantalate which we attribute to the concomitant effects of protonated clusters. This thesis provides evidence that structurally identical species do not necessarily exhibit the same behavior in solution. Differences in stability, protonation, and electrostatic interactions with counterions provide some insight into the anomalous solubility of niobium and tantalum polyoxometalates.

Exploring the Distinct Solution Behavior of Isostructural Polycoltanates

by
Lauren Fullmer

A DISSERTATION

submitted to

Oregon State University

in partial fulfillment of
the requirements for the
degree of

Doctor of Philosophy

Presented November 1, 2016
Commencement June 2017

Doctor of Philosophy dissertation of Lauren Fullmer presented on November 1, 2016.

APPROVED:

Major Professor, representing Chemistry

Chair of the Department of Chemistry

Dean of the Graduate School

I understand that my dissertation will become part of the permanent collection of Oregon State University libraries. My signature below authorizes release of my dissertation to any reader upon request.

Lauren Fullmer, Author

ACKNOWLEDGEMENTS

To my advisor Dr. May Nyman, for providing the opportunity to work with her and join the polyoxometalate community. May, thank you for being such a fun and interesting person while providing advice and guidance during the last 4 years. I am proud to be your first student.

To the Nyman research group members past and present for friendship, support, and impromptu conversations. Especially:

Dr. Pedro Molina-Sanchez- for your constant support and guidance and proof reading this thesis.

Harrison Neal-for always being open to any kind of conversation, whether gossip, football, or my random stupid questions. For being my work-husband and doing the heavy lifting.

Omid Sadeghihosseinabadi- for always putting a smile on my face no matter what.

To the Keszler research group for being helpful in so many ways, professionally and personally.

To the people in the chemistry department, for always having someone to smile at and chat with in the hallway.

Ryan- for loving and supporting me even when I've felt like I've gone crazy. You are my rock.

My family and friends have always been at my side encouraging me to succeed in everything. For that I am always grateful.

CONTRIBUTION OF AUTHORS

M.N. provided significant guidance on all experimental design, insights on the result discussions and manuscript writing. In Chapter 5, all authors contributed to the manuscript writing and editing. R. M. assisted in film deposition, and analysis of all film characterization. L.N.Z. performed single crystal x-ray diffraction. D.A.K. and M.N. provided valuable insights and suggestions. In Chapter 6, all authors contributed to the manuscript writing and editing. L.A.W. and C.M. performed computations on energetics and Raman spectra. P.H-Y.C. provided insight on the computational work. In Chapter 7, all authors contributed to the manuscript writing and editing. M.N. contributed to interpretation of results and discussion.

TABLE OF CONTENTS

Page

TABLE OF CONTENTS (Continued)

Page

TABLE OF CONTENTS (Continued)

Page

LIST OF FIGURES

LIST OF FIGURES (Continued)

LIST OF FIGURES (Continued)

LIST OF TABLES

LIST OF TABLES (Continued)

LIST OF APPENDIX FIGURES

LIST OF APPENDIX FIGURES (Continued)

LIST OF APPENDIX TABLES

LIST OF APPENDIX TABLES (Continued)

LIST OF ABBREVIATIONS

POM	Polyoxometalate
PONb	Polyoxoniobate
POTa	Polyoxotantalate
SWAXS	Small and wide angle X-ray scattering
PDDF	Pair distance distribution function
R_g	Radius of gyration
TMA	Tetramethylammonium
ESI-MS	Electrospray ionization mass spectrometry
XRD	X-ray diffraction
XRR	X-ray reflectivity
AFM	Atomic force microscopy
SEM	Scanning electron microscopy
TGA/DSC	Thermogravimetric analysis/differential scanning calorimetry
DFT	Density functional theory

1 AN INTRODUCTION TO POLYOXOMETALATES

The scientific definition of "cluster" usually refers to a metal-metal bonded molecule of more than 3 atoms, but there is an entire world of metal-oxide "clusters" known in the scientific community. In 1826, Swedish chemist, Jacob Berzelius, published a paper describing the newly recognized element molybdenum and his preparation of the dodecamolybdophosphate anion, $[PMo_{12}O_{40}]^{3-}$.[1] While many similar compounds were synthesized by a number of chemists, it was more than a hundred years before the structure was solved. In 1933, Keggin provided the first definitive explanation of a tungsten analogue of the $M_{12}O_{40}$ structure: WO_6 octahedral units connected by both corners and edges. [2–5] So began the field of polyoxometalate and related polyoxocation chemistry.

Polyoxometalates, or POMs, are water soluble metal oxide clusters formed from groups 5 and 6 transition metals primarily in their highest oxidation state. POMs are composed of metal-oxygen octahedra that can be corner, edge, or face sharing. This leads to a plethora of different structures, some of the most diverse contributions from molybdenum and tungsten. A unique feature of POMs is their discrete, monodisperse nature, which differentiates them from similarly sized nanoparticles. POMs lie in the realm between an infinite solid metal oxide and metal oxo/hydroxo monomers. Related to POMs are the polyoxocations from group 13. While these are not classified as polyoxometalates, they are very similar in structure and less so in their chemistry. However, these positively charged metal-oxo clusters are outside the scope of this thesis.

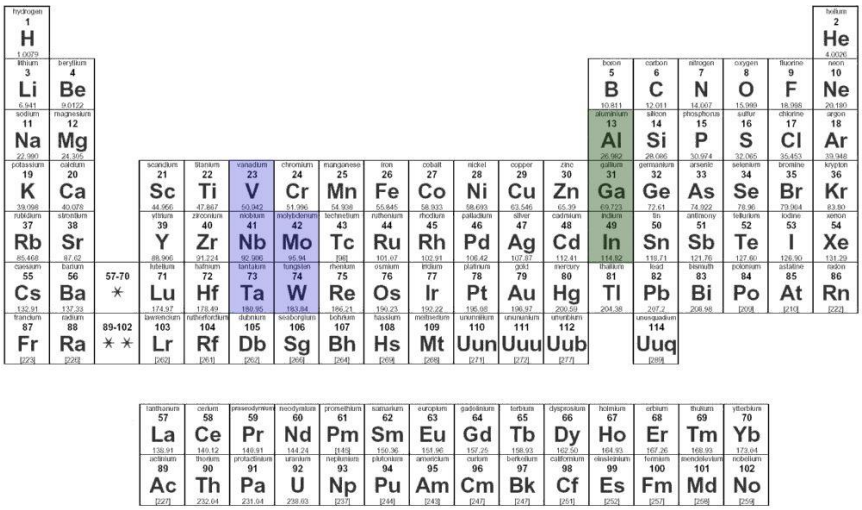

Figure 1.1. Periodic table of the elements. Those elements that form polyoxometalates are in blue, and polyoxocations in green.

There are many other cluster forming elements on the periodic table that are not considered polyoxometalates (examples: U, Np, Pu, group IV, etc.). However, we will focus on polyoxoniobates and tantalates, more recently referred to as polycoltanates. This name is derived from coltan, the metallic ore from which niobium and tantalum are extracted.[6,7]

1.1 THE CHEMISTRY OF POLYOXOMETALATES

The solution speciation of niobium and tantalum differ from the group VI metals as well as vanadium. In more alkaline solutions, the group VI metals exist as mononuclear metal oxo anions, MO_4^{n-} (n = 2, 3). Upon acidification of the solution, the metal oxoanion undergoes protonation, expands its coordination sphere, and condenses via water elimination, forming bound MO_6 octahedra. The polymerization of the metal oxide is halted by a multiply bonded oxygen with decreased basicity, also known as the -yl oxygen. The unoccupied d-orbitals in fully oxidized group V and VI transition metals allows significant overlap with oxygen orbitals and causes a distortion in the MO_6 octahedra. Since the -yl oxygen is multiply bonded and stronger, it's bond length is shortened. Therefore the M-O bond trans to the -yl oxygen is lengthened[2] as shown

in **figure 1.2**. The lengthening of the M-O bond reduces the oxygen's negative charge, inducing condensation to satisfy bond valence.[8]

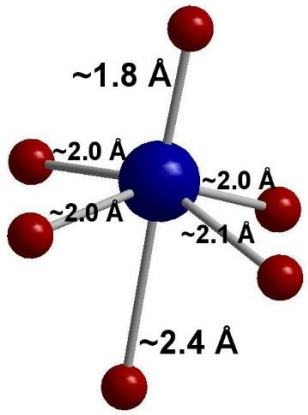

Figure 1.2. Distorted MO_6 octahedron from the Nb Lindqvist ion.

The linking of oxoanions/MO_6 octahedra can form isopolyanions, $[M_6O_{19}]^{n-}$, or heteropolyanions, $[XM_{12}O_{40}]^{n-}$, such as the Keggin ion. The MO_6 octahedra can link via corners, edges, or faces (**figure 1.3**). The ability of the octahedra to bond in various geometries as well as templating around heteroatoms or incorporating mixed addenda atoms, yields a plethora of structures. The variety of polyoxometalate compositions and structures, as well as development of structure solving instrumentation, have led to a rapid expansion in this field of chemistry, as well as increasingly interesting applications.

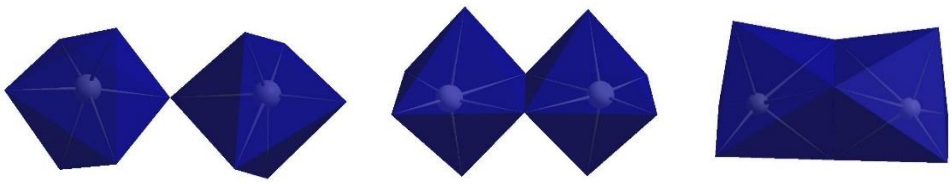

Figure 1.3. From left to right: Corner sharing, edge sharing, and face sharing octahedra in polyoxometalates.

The majority of polyoxometalate structures are composed of molybdenum or tungsten. Polyoxometalates of Nb and Ta and also V are limited in number. This is due

to the inability of these metals to form different coordination geometries with oxygen.[2,8] Nb and Ta prefer the octahedral coordination state, while Mo, W, and V prefer tetrahedral coordination until protonation causes an elongation of the M-O bonds in the oxoanion. This elongation allows the metal to form an octahedral coordination. Vanadium's behavior diverges from the other polyoxometalates forming metals due to its smaller size and strong tendency to protonate causing much larger species to form such as decavanadate.[8]

Synthetic procedures for polyoxometalates can be deceptively simple, the majority of which are "one pot" methods. Aqueous solutions of metal-oxo groups can be manipulated in these "one pot" reactions by adjusting 1) concentration/ratio of counterions or other metals, 2) pH, 3) temperature, and 4) solvent. These factors can vastly affect speciation in solution with the slightest change in synthetic procedures.[2,4]

The synthesis of polycoltanates differs from the group VI and vanadium POMs, due to the inability of Nb and Ta to form monomeric oxoanions.[9] Therefore, starting materials are more commonly the hydrous metal oxides or a peroxo bound metal, $[M(O_2)_4]^{3-}$.[10–12] Polycoltanates are synthesized in alkaline solutions and predominantly exist as the hexametalate Lindqvist ion. The Lindqvist ion, $[M_6O_{19}]^{n-}$, is a superoctahedron composed of six structurally identical, edge sharing MO_6 octahedra[13] as shown in **figure 1.4**.

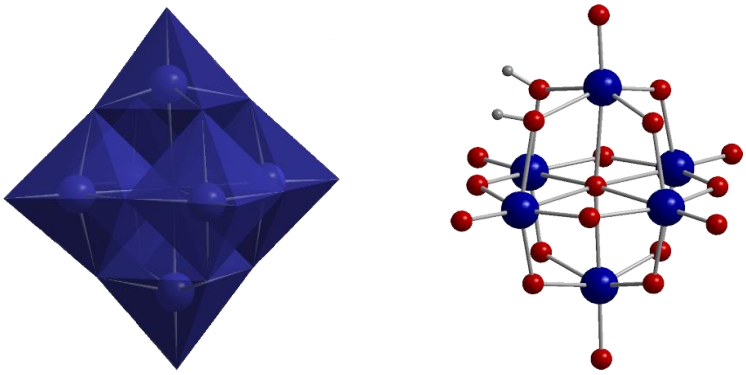

Figure 1.4. Polyhedral representation of the hexametalate Lindqvist ion (left), skeletal structure with protonation of bridging oxygens (right).

Due to the lanthanide contraction, Ta and Nb are identical in size,[14] which also renders their hexametalate structures almost indistinguishable.[12] Hexaniobate and hexatantalate are charge dense and require eight counterions and/or protons to balance the high charge. Common counterions are the alkali metals, or small organics such as tetramethylammonium or tetrabutylammonium. Polycoltanates exhibit an anomalous trend in solubility that differs from the other POMs. The alkali salts of hexaniobate and hexatantalate are increasingly soluble from Li<Na<K<Rb/Cs. This is unusual due to the notorious trend that Cs salts of larger anions are more insoluble while Li salts have increased solubility.[15]

Polyoxometalates can be protonated in solution and in the solid state. There has been some debate on the basicity of the types of oxygens in a POM (terminal -yl oxygen and bridging oxygens). However, through numerous studies, it has been determined that site of protonation is predominantly the bridging oxygens (**figure 1.4**) due to the negative ionic charge concentrating at these sites. This renders the bridging oxygens the most basic oxygens in the structure.[8,16,17] Only in rare cases has a protonated terminal bound oxygen been identified.[18–21] While the protonation sites in the solid state are determined with x-ray crystallography, it is also possible to confirm protonation in solution with techniques such as NMR and x-ray scattering,[2] either by direct or indirect means, probing the effect of that protonation.

1.2 CHARACTERIZATION OF POLYOXOMETALATES

The characterization of polyoxometalates can be carried out in the solid state or in solution, and a number of various methods can be employed. One of the most common and easily employed techniques is spectroscopy. Vibrational spectroscopy can be used to quickly identify if expected M-O bonds exist. There are distinct regions where terminally bound and bridging oxygen peaks can be found (see **figure 1.5**). Infrared and ultraviolet-visible spectroscopy were first reported as POM characterization methods in the 1960s.[22–26]

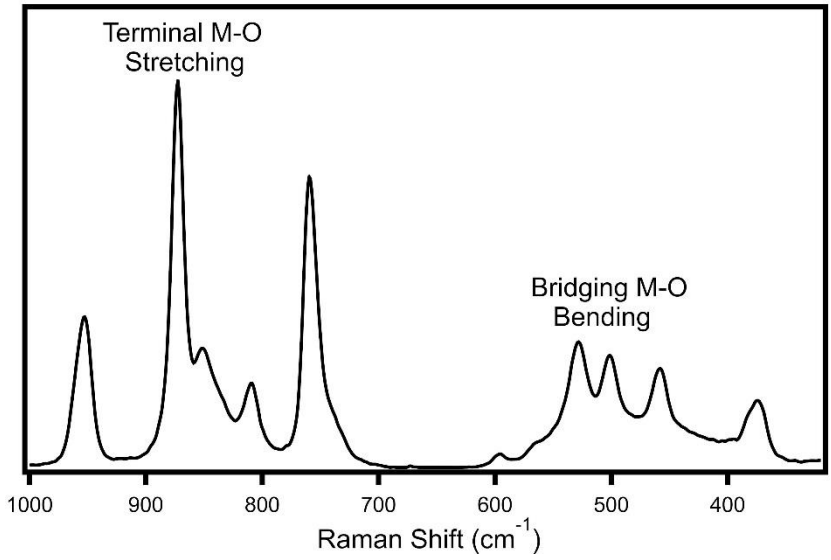

Figure 1.5. Raman spectrum of $((CH_3)_4N)_6H_2Ta_6O_{19}$ as an example of terminal and bridging M-O peak regions.

Nuclear magnetic resonance (NMR) spectroscopy is used for determining the environments of specific atoms in a polyoxometalate either in solution or solid state. ^{31}P NMR is utilized for identifying POMs such as the phosphotungstates and phosphomolybdates. ^{29}Si NMR is also available for identifying Keggin structures that include Si instead of P as the heteroatom. Polyoxometalates can be characterized with their corresponding nuclei such as ^{51}V NMR and ^{183}W NMR. Unfortunately, there are some nuclei with quadrupole moments that cause line broadening and therefore makes characterization extremely difficult (tantalum and molybdenum for example). Related to NMR is EPR, or electron paramagnetic resonance spectroscopy. EPR can detect and identify free radical and paramagnetic centers. It can also provide information on an atom's coordination geometry either in solution or in the solid state.[27]

X-ray photoelectron spectroscopy (XPS) has been gaining popularity in recent years for characterization of POMs. XPS is a surface technique for measuring elemental compositions and the electronic states of elements. This technique can be employed for identifying substitution of elements into a cluster as well as analyzing the surface of films deposited from POMs.[28]

With high resolution transmission electron microscopy (TEM), it is possible to observe individual polyoxometalate clusters. Sample preparation can include placing a drop of solution containing POMs onto a TEM grid, as well as adsorbing POMs onto a surface in an ordered array, where the periodicity may be observed. Scanning electron microscopy (SEM) can be used to observe crystallites or probe bulk powders. Utilizing energy dispersive x-ray spectroscopy (EDS) paired with microscopy can aid in determining elemental compositions. However, more reliable elemental analysis from a commercial laboratory or by atomic absorption is still necessary for complete confidence in the results.

Polyoxometalates can be studied in the solution state via scattering techniques such as light scattering, neutron scattering, and x-ray scattering.[27] The size, molecular weight, and relative shape of the clusters can be determined, as well as interactions between the species in solution such as ion association. X-ray scattering has been used extensively in the work reported in this thesis and a full description will be provided in a later chapter.

Mass spectrometry is a useful technique for identifying species present in solution by separating them in order of their mass to charge ratio.[29] Some POMs are more easily characterized by this technique, such as W, due to the isotopic envelope. Metals with less abundant isotopes are more difficult to characterize with mass spectrometry, but higher resolution instruments can make this easier. Relative percentages of each species can also be determined. Mass spectrometry can be coupled with various techniques such as chromatography, thermogravimetric analysis, capillary electrophoresis, electrospray ionization, inductively coupled plasma, etc.

Computational chemistry provides valuable information to complement characterization of polyoxometalates. Simulated data can be produced for a number of different methods such as vibrational spectroscopy, NMR, scattering data, etc. Computations can also determine energetics of the clusters in various conditions, and can help us to understand speciation and formation of these interesting metal oxide clusters.[27,30]

1.3 APPLICATIONS OF POLYOXOMETALATES

The applications of polyoxometalates are far reaching due to their wide range of properties and ability to incorporate virtually every element lighter than Cf with exception of the noble gases.[2] The group VI and vanadium POMs possess extensive redox properties relevant to catalysis and electron transfer processes. Therefore, the silico- and phospho- tungstates and molybdates are the most referenced examples for applications. For all POMs, salts that are incorporated into the synthesis to provide charge balancing cations can be both water soluble and organic soluble, allowing applications in both media.

A recent and very common area of application for polyoxometalates involves the use of functionalized POMs for various catalytic reactions. Inorganic-organic hybrid POMs can be applied to designing novel multi-functional materials. These amphiphilic functionalized clusters can be formed electrostatically via counterion association, or covalently by replacing terminal or bridging oxygens with other atoms or organic groups. Hybrid POMs may find unique applications in enantioselective catalysis and separation by incorporating chiral organic molecules into the structure. Combining amino acids or peptides with POMs can provide biological functionality.[31] Photo-induced electron transfer in POM-porphyrin hybrids provides photosensitive systems for catalysis, photovoltaics, and for environmental applications such as depollution and recovery of valuable or toxic metals.[32,33]

Another photocatalytic application of inorganic-organic hybrid POMs is the construction of layer-by-layer thin films. Adsorbing anionic clusters onto cationic dye molecules provides distinctive electronic and optical properties, allowing the material to absorb visible light.[34]

Catalysis can also be achieved by POMs without the need of organic components. Due to the redox properties of Mo and W, hetero- and isopolyanions of group VI POMs are excellent candidates for catalysis. The properties can be tailored and tuned by incorporating other metals into the structure such as Co, which can participate in water oxidation.[35]

The redox active POMs have the potential to store electrons for metal-insulator semiconductor devices, as well as electrochromics and electro-switchable fluorescence. Intercalation of POMs into graphene oxide has attracted much attention, as well as covalently attaching POMs to nanocarbon materials for electron transfer and storage processes.[36,37]

Polyoxometalates also have applications in the life sciences. Heptamolybdate displays anti-tumor activities and can bind with DNA, while other molybdates and tungstates can inhibit enzymatic activities, and bind with biomolecules for bioimaging.[37] POMs can also aid in precipitation and crystallization of proteins due to electrostatic interactions.

While individual POMs can be grafted onto surfaces by various methods, they can also be annealed to yield simple metal-oxide films.[38] By annealing POMs, the structure is broken down into amorphous metal oxides, which are excellent candidates for electrochromic coatings. Motivation for some of the work presented in this thesis stems from this potential application. Metal oxide films, specifically of Nb_2O_5 and Ta_2O_5 composition, are of interest for antireflective coatings, and corrosion/diffusion barriers.[28] The advantages of utilizing POMs for metal-oxide thin film formation will be discussed in another chapter.

(1) Berzelius, J. J. *Ann. Phys.* **1826**, *82*, 369–392.
(2) Borras-Almenar, J. J.; Coronado, E.; Muller, A.; Pope, M. T.; Müller, A.; Pope, M. T. *Polyoxometalate Molecular Science*; Kluwer Academic Publishers, 2003.
(3) Moffat, J. B. *Metal-Oxygen Clusters: The Surface and Catalytic Properties of Heteropoly Oxometalates*; Kluwer Academic/Plenum Publishers: New York, New York, 2001.
(4) Sécheresse, F. *Polyoxometalate Chemsitry: Some Recent Trends*; World Scientific Puublishing, 2013.
(5) Keggin, J. F. *Proc. R. Soc. A Math. Phys. Eng. Sci.* **1934**, *144*, 75–100.
(6) Sures, D. J.; Molina, P. I.; Miró, P.; Zakharov, L. N.; Nyman, M. *New J. Chem.* **2016**.
(7) Molina, P. I.; Sures, D. J.; Miró, P.; Zakharov, L. N.; Nyman, M. *Dalt. Trans.* **2015**.
(8) Tytko, K. H.; Mehmke, J.; Kurad, D.; Fischer, S. *Bonding and Charge Distribution in Polyoxometalates- A Bond Valence Approach*; Mingos, D. M. P.,

Ed.; Springer, 1999.
(9) Baes, C. F.; Mesmer, R. E. *The Hydrolysis of Cations*; John Wiley & Sons, Inc., 1976.
(10) Nyman, M.; Alam, T. M.; Bonhomme, F.; Rodriguez, M. A.; Frazer, C. S.; Welk, M. E. *J. Clust. Sci.* **2006**, *17*, 197–219.
(11) Alam, T. M.; Nyman, M.; Cherry, B. R.; Segall, J. M.; Lybarger, L. E. *J. Am. Chem. Soc.* **2004**, *126*, 5610–5620.
(12) Anderson, T. M.; Rodriguez, M. A.; Bonhomme, F.; Bixler, J. N.; Alam, T. M.; Nyman, M. *Dalton Trans.* **2007**, *9226*, 4517–4522.
(13) Lindqvist, I. *Ark. Kemi* **1953**, *5*, 247.
(14) Shannon, R. D. *Acta Cryst.* **1976**, *A32*, 751–767.
(15) Nyman, M. *Dalt. Trans.* **2011**, *40*, 8049–8058.
(16) Matsumoto, M.; Ozawa, Y.; Yagasaki, A. *Inorg. Chem. Commun.* **2011**, *14*, 115–117.
(17) Day, V. W.; Klemperer, W. G.; Maltbie, D. J. *J. Am. Chem. Soc.* **1987**, *109*, 2991–3002.
(18) Isobe, M.; Marumo, F. *Acta Cryst.* **1978**, *34*, 2728–2731.
(19) Deshlahra, P.; Iglesia, E. *J. Phys. Chem. C* **2014**, *118*, 26115–26129.
(20) Kaledin, A. L.; Duin, A. C. T. Van; Hill, C. L.; Musaev, D. G. **2013**, 4–11.
(21) Cruywagen, J. J. *Adv. Inorg. Chem.* **2000**, *49*.
(22) Brown, D. H. *J. Chem. Soc.* **1962**, 3322.
(23) Brown, D. H. *J. Chem. Soc.* **1962**, 4408.
(24) Brown, D. H. *Spectrochim. Acta* **1963**, *19*, 1683–1685.
(25) Tsigdinos, G. A.; Hallada, C. J. *Inorg. Chem.* **1968**, *7*, 437–441.
(26) Sharpless, N. E.; Munday, J. S. *Anal. Chem.* **1957**, *29*, 1619–1622.
(27) Jackson, M. N.; Kamunde-Devonish, M. K.; Hammann, B. A.; Wills, L. A.; Fullmer, L. B.; Hayes, S. E.; Cheong, P. H.-Y.; Casey, W. H.; Nyman, M.; Johnson, D. W. *Dalt. Trans.* **2015**, *44*, 16982–17006.
(28) Mansergh, R. H.; Fullmer, L. B.; Park, D.-H.; Nyman, M.; Keszler, D. A. *Chem. Mater.* **2016**, acs.chemmater.6b00078.
(29) Ohlin, C. A. *Chem. An Asian J.* **2012**, *7*, 262–270.
(30) López, X.; Carbó, J. J.; Bo, C.; Poblet, J. M. *Chem. Soc. Rev.* **2012**, *41*, 7537–7571.
(31) Li, D.; Yin, P.; Liu, T. *Dalt. Trans.* **2012**, *41*, 2853–2861.
(32) Schaming, D.; Ruhlmann, L. In *Trends in Polyoxometalates Research*; 2015; pp. 237–264.
(33) Proust, A.; Matt, B.; Villanneau, R.; Guillemot, G.; Gouzerh, P.; Izzet, G. *Chem. Soc. Rev.* **2012**, *41*, 7605–7622.
(34) Gao, S.-Y.; Lu, J.; Cao, R. In *Trends in Polyoxometalates Research*; 2015; pp. 265–280.
(35) Soriano-López, J.; Goberna-Ferrón, S.; Vigara, L.; Carbó, J. J.; Poblet, J. M.; Galán-Mascarós, J. R. *Inorg. Chem.* **2013**, *52*, 4753–4755.
(36) Ji, Y.; Huang, L.; Hu, J.; Streb, C.; Song, Y.-F. *Energy Environ. Sci.* **2015**, *8*,

776–789.
(37) Omwoma, S.; Chen, W.; Gore, C. T.; Song, Y. F. In *Trends in Polyoxometalates Research*; 2015; pp. 281–354.
(38) Fullmer, L. B.; Mansergh, R. H.; Zakharov, L. N.; Keszler, D. A.; Nyman, M. *Cryst. Growth Des.* **2015**, *15*, 3885–3892.

2 AN INTRODUCTION TO SMALL AND WIDE ANGLE X-RAY SCATTERING

Small and wide angle X-ray scattering (SWAXS) is an analytical technique used to extract structural information about particles in solution or as solid materials of very small or large macromolecular systems.[1,2] This technique has been employed since the 1950's to study colloidal nano-scale materials.[3,4] SWAXS is fundamentally similar to X-ray crystallography insofar as in both techniques a sample is irradiated by a monochromatic beam of X-rays providing data from which we can determine structural information. Small-angle (and same for wide-angle) scattering is utilized for characterizing larger distances as in the size of molecules as a whole while wide angle scattering, also known as x-ray diffraction, is used for smaller interatomic distances. As shown in **figure 2.1**, the information gained from structural characterization is dependent on the capabilities of the instrument. Scattering can be used to probe the microstructure of materials and falls between the realm of crystal structure determination and overall structural morphology.

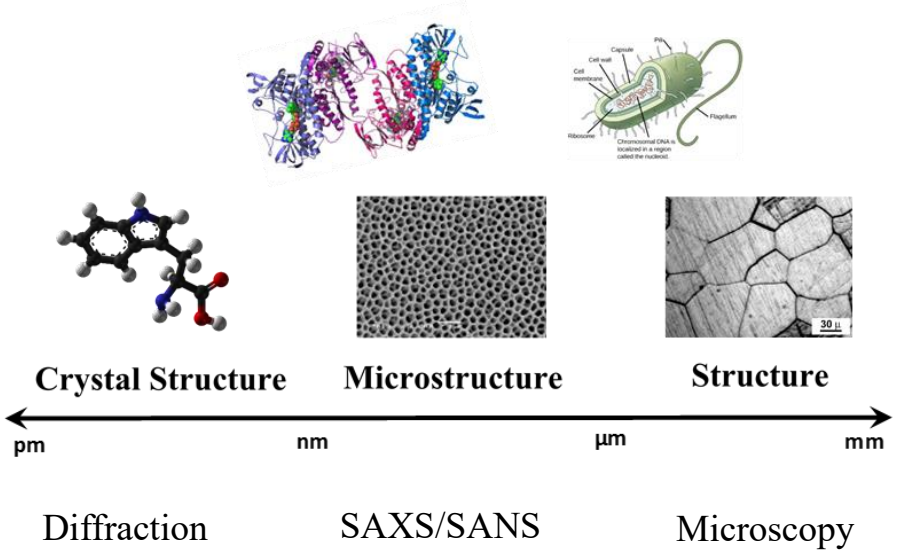

Figure 2.1. Comparison of the length scale of scattering techniques to other structural characterization.

Scattering experiments can differ depending on the x-ray source used in the instrument. In-house bench-top SWAXS instruments typically use sealed tube copper or molybdenum sources. Synchrotron radiation is an appealing option since it provides x-rays of all wavelengths. X-ray scattering techniques have grown in popularity due to the recent development of synchrotron x-ray sources. SWAXS is a non-destructive technique that requires minimal sample preparation. The applications of this analysis range from metals and nanocomposites to biological materials, food science, and pharmaceuticals.[1] There are variations of the scattering technique that include transmission mode for analyzing solids and solutions, and grazing incidence for surface characterization. This discussion will focus on transmission mode SWAXS for studying particles in solution.

2.1 General Theory

When X-rays interact with a material, a fraction of the radiation will be absorbed, some of it will pass through the sample, and some will be scattered. Analytical X-ray techniques can measure the scattered radiation with a detector which absorbs the photons. In an x-ray scattering experiment, the X-ray beam interacts with the particles causing electrons to oscillate at the same frequency as the incoming radiation. This emits X-rays with the same wavelength as the incident beam.[5] These coherent X-rays can interfere with each other causing constructive or destructive interference patterns at the detector that give rise to structural information about the particles.[1,2] X-ray scattering is characterized by reciprocity, providing an inverse relationship between particle size and scattering angle.[5] In other words, the scattering of x-rays at the nanometer scale from contrasting electron densities will occur at low angles. The scattering at the atomic scale occurs at high angles, or the wide-angle scattering region.

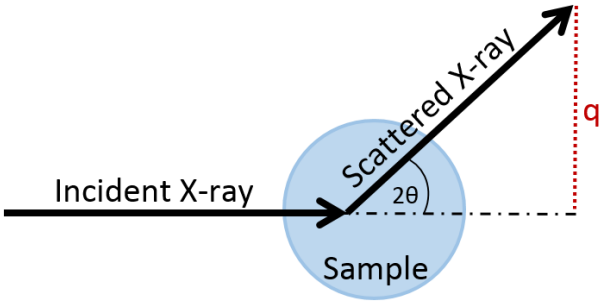

$$q = \frac{4\pi}{\lambda} \cdot \sin(\theta)$$

Figure 2.2. Scattering of X-rays by a single particle. *Q* is the scattering length vector derived from the wavelength of the incoming radiation and the scattering angle.[3]

The scattering measurement is a continuous, isotropic average of the signals from particles in all orientations relative to one another and to the experimental apparatus.[2] Solvent molecules also scatter and therefore careful data processing is required to subtract out background solvent scattering. The intensity of the scattering is proportional to the number of x-rays measured by the detector and is affected by a number of factors including sample transmittance, concentration, and electron density. X-ray scattering is a contrast technique where the more electrons present in a sample volume, the more x-rays are scattered. The overall scattering is the contrast in electron densities between solute molecules of interest and the bulk solvent. Larger intensities are the result of larger differences in electron densities between solute and solvent[1,5]; thus high Z elements in the material of interest and low Z elements in the solvent provide the optimal scenario.

2.2 INSTRUMENTATION

There are five basic components of an x-ray scattering instrument; the source of radiation, a collimation system, sample holder, beam stop, and a detector (See **figure 2.3)**. X-ray sources include synchrotron radiation, rotating anodes, or sealed x-ray tubes.[1] In order to correctly interpret scattering data, the incoming radiation must be monochromatic. This can be accomplished with filters or reflecting mirrors.[5] For laboratory based instruments, sealed x-ray tubes with either a copper or molybdenum

source are most common. The K lines are generally utilized due to their higher intensity.[6]

The divergence of the primary x-ray beam must be kept to a minimum to avoid overpowering the relatively weak intensity of the scattering pattern from the sample. To separate the incoming beam from the scattered radiation, a collimation system is required. In front of the x-ray source, a point or line collimation system is employed to narrow the beam of the incident radiation. Point collimation uses circular or elliptical pinholes to confine the beam. This allows only a small section of the sample to be irradiated causing low intensity. The resolution also suffers but can be improved with much longer exposure times on the order of hours. Line collimation provides a narrow more intense primary beam that is confined in only one direction. Resolution is significantly increased compared to the point collimation instrument, although this is under debate.[7] A disadvantage of line collimation is slit smearing effects or broadening of the scattering pattern. Therefore, it is essential that the profile of the incident beam be measured and incorporated into the data processing as "desmearing" to negate these distortions.[1,3,6]

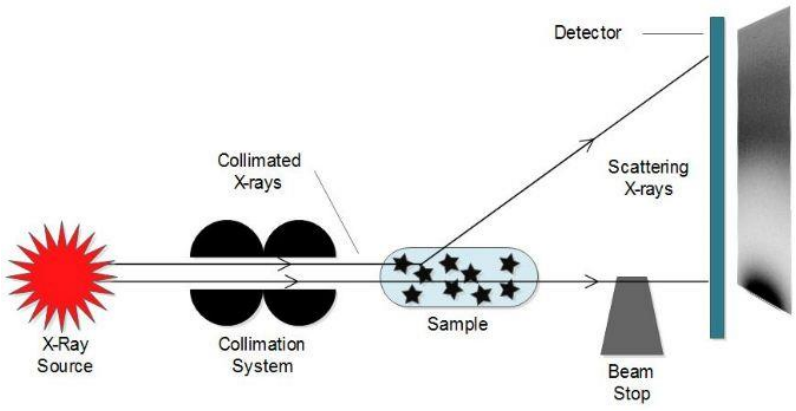

Figure 2.3. The components of a SWAXS instrument including a typical two-dimensional scattering image (right) obtained from a laboratory SAXSess instrument.

The sample holder component of a SWAXS instrument can vary greatly depending on the type of instrument, the type of sample, and the information to be acquired. Laboratory based instruments require the sample holder to be evacuated to eliminate

background scattering from air, therefore sealed capillaries or a flow system are common. Other sample holders can vary greatly and are outside the scope of this discussion.

The beam stop of the instrument is necessary for preventing the intense direct beam from hitting the detector which can both overpower the scattering from the sample, and damage the detector. Beam stops can be a material that blocks the incident beam entirely such as lead or tungsten, or a material like nickel that simply attenuates the beam to a more manageable intensity. Common detectors used with SWAXS instruments include charge coupled device (CCD) detectors, imaging plates, and solid state detectors.[1]

The instrument setup varies from laboratory sources to synchrotron beamlines. The radiation source, collimation, sample holder, and detector can all be adjusted depending on the type of experiment. The needs of every scientist are different and this is reflected in the instrumentation available. An advantage of having an in-house SWAXS instrument is the ability to screen samples year-round to determine which systems require the synchrotron source. The quality of data can be considerably better from a synchrotron source due to higher energy x-rays. With synchrotron radiation, more challenging systems can be explored; for example, highly absorbing solutions, very low concentrations, or sub-nanometer species.

2.3 DATA INTERPRETATION

Interpreting SWAXS data is a matter of extracting information about a three-dimensional particle from one-dimensional data. Some common parameters which can be determined include the particle's radius of gyration (R_g), as well as the size distribution, particle shape, and interactions between particles. The following equation defines the intensity and encompasses form factors (size, shape and scattering contrast) and structure factors (interactions between particles):

$$\frac{d\Sigma}{d\Omega}(Q,r) = V_s^{-1}|\Delta\rho(r)|^2\left|V_p(r)F_p(Q,r)\right|^2$$

Where $\frac{d\Sigma}{d\Omega}(Q,r)$ is the absolute intensity, V_s is the volume of the sample, $|\Delta\rho(r)|^2$ represents the difference in scattering length densities. $V_p(r)$ is the volume of the scatterer while $F_p(Q,r)$ is the form factor of the scatterer.[5]

The scattering curve is typically represented by a plot of Log(Intensity) vs Log(q) (see **figure 2.4)**. Q is the length of the scattering vector that is determined from the x-ray wavelength and the scattering angle.

$$q = \frac{4\pi}{\lambda} \cdot \sin(\theta)$$

The scattering vector is in reciprocal space, therefore the unit for q is inverse length, for example, Å^{-1}. There are some who prefer to use s instead of q because of the application in crystallography to determine distances between crystal lattice planes.[1]

$$s = \frac{q}{2\pi}$$

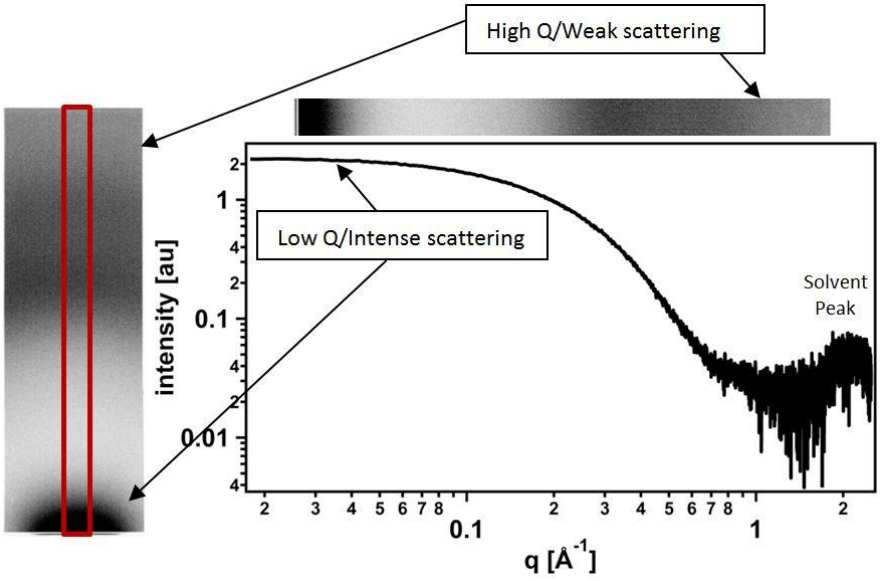

Figure 2.4. One-dimensional scattering curve extracted from the two-dimensional scattering pattern. Low Q region is where the most intense scattering occurs while weaker scattering occurs at higher Q.

The scattering of a single particle creates a scattering pattern which oscillates in a way characteristic of the shape of that particle. This characteristic oscillation is referred

to as the form factor. When irradiating a sample, the overall scattering would be the sum of all irradiated particles averaged to create a scattering pattern. Therefore, data from monodisperse samples, or samples of all the same size and shape, are more true to the form factor. Polydisperse samples no longer contain well-defined form factors due to the various shapes and sizes that are average together. This creates difficulty in analyzing polydisperse samples, as the shape information may be lost. Another contributor to the intensity of a scattering pattern is the structure factor. When the distances between particles are the same magnitude as the distances within the particle, the neighboring particles contribute to the scattering pattern.

Interferences between particles in solution greatly contribute to the scattering curve, especially in the low q region. Interparticle interactions cause a decrease in the scattering intensity in the low q region[5] as shown in the green curve in **figure 2.5.** If the particles in solution are forming aggregates or larger molecular arrangements, an increase in the intensity at low q will be observed. In order to observe these larger species, ultra-small angle X-ray scattering is needed so that the q range extends to even smaller angles.

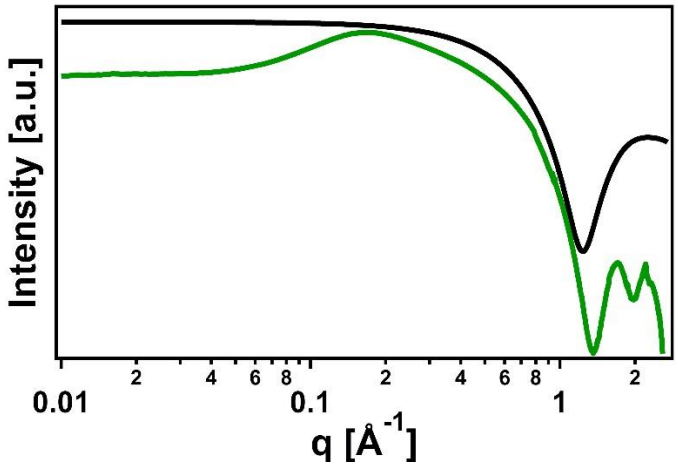

Figure 2.5. An example of features in an experimental scattering curve (green) compared to a simulated scattering curve (black).

While some important information about the scattering particles can be determined from SWAXS, the averaging of all particles leads to a loss of information on the atomic scale. While the structure of the particles cannot be determined by this technique, it is

possible to roughly characterize particles by shape and size, and interactions between them.

From scattering data, a radius of gyration (R_g) can be calculated. R_g is a shape independent root-mean-square measure of all mass-weighted vectors in the cluster from the center of mass.[1,2,5] R_g is model independent meaning it does not provide information about the shape of the particle. If the shape of the particles is known (i.e. from another characterization technique), the radius can be calculated using a corresponding formula.[1,2] See **figure 2.6** for some examples.

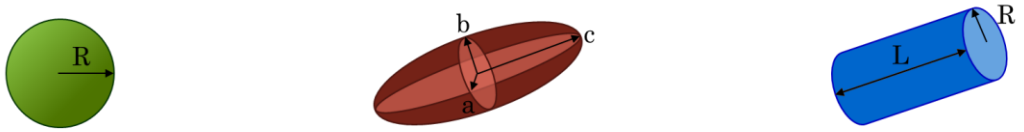

Sphere | Ellipsoid | Cylinder

$$R_g{}^2 = \frac{3}{5}R^2 \qquad R_g{}^2 = \frac{1}{5}(a^2 + b^2 + c^2) \qquad R_g{}^2 = \frac{L^2}{12} + \frac{R^2}{2}$$

Figure 2.6. Common formulae for determination of radius from radius of gyration.

The R_g only has true meaning in the case of a monodisperse system. The degree of order in a system greatly affects the scattering pattern and in turn the ability to extract structural information from the data. I must quote Feigin and Svergun: "The less ordered an object, the less informative the scattering pattern.[6]" It is also vital that other techniques are employed to corroborate any conclusions based on scattering data.

Since scattering data is obtained in reciprocal space, a useful modeling method for SWAXS data is the pair distance distribution function or PDDF, which is represented in real space. The pair distance distribution function can be obtained through an inverse Fourier transform of the scattering intensity,[1,5]

$$P(q) = 4\pi \int_0^\infty (p) r \frac{\sin(qr)}{qr}\, \mathrm{d}r$$

to yield a P(r) vs r plot, that represents probability of electron density as a function of radius. The r term is the distance from any point within the particle to the edge of that

particle. The probability of electron density is related to the number of equivalent length vectors with the particle. The point at which the P(r) goes to zero is the maximum linear extent or likely the diameter of the particle. PDDF is similar to the pair distribution function analysis used in neutron and x-ray total scattering, but instead of acquiring atom-atom distances, we can only detect distances between areas of high electron density, such as molecule to molecule. The shape of the PDDF plot is indicative of the shape of the scattering particle as seen in **figure 2.7**. From this information we can understand more about the shape and size of the particles in real space.

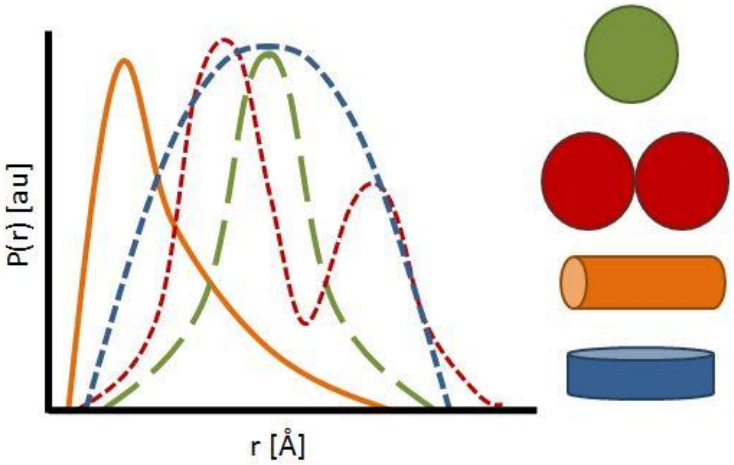

Figure 2.7. Pair distance distribution functions with corresponding shapes.[8]

A less commonly used procedure for laboratory SWAXS experiments is the conversion from arbitrary units by an absolute calibration. A standard, such as glassy carbon, can be supplied by a synchrotron source with known differential scattering cross section and thickness. By measuring the same sample on a laboratory source, taking into account the transmission and thickness of the sample, it is possible to obtain a scaling factor that can be used to scale all experimental data to absolute units. However, this can be quite difficult due to the lower flux of laboratory based instruments. While it is possible to obtain form factor, structure factor, and size information from scattering data in arbitrary units, calibration to absolute units provides

the ability to determine molecular weights, number densities of particles in multiphase systems, specific surface area, and volumes.[9]

2.4 POLYOXOMETALATES AND SMALL ANGLE X-RAY SCATTERING

Polyoxometalates (POMs) are intriguing aqueous species for study by small and wide angle x-ray scattering. POMs are stable, discrete clusters that are monodisperse allowing full characterization of the scattering data. The size and shape can be easily characterized in these monodisperse solutions and compared with solid state data. It is always necessary to complement SWAXS data with other analytical techniques such as transmission electron microscopy, mass spectrometry, nuclear magnetic resonance and vibrational spectroscopies.

POMs are composed of group V and VI high Z transition metals. Since they are water soluble, these systems provide excellent electron density contrast between the cluster and the solvent. As SWAXS relies on the difference in electron densities, aqueous POM solutions are ideal systems to study with x-ray scattering. POMs can also interact with each other and with their counterions which can affect the scattering curve. From these types of interactions, POMs are model solutions from which the information learned can be applied to other areas of scattering research.

The increasing popularity of x-ray scattering has allowed the polyoxometalate community to expand into this area of characterization. There are a number of books and reviews that detail the latest research in polyoxometalates, where we see more x-ray and neutron scattering in recent years.[8,10,11] Some examples include the ion association of hexametalates ($M_6O_{19}^{-8}$) with their counterions,[12–14] the effect of counterion association on base hydrolysis of the clusters,[15] dimerization of clusters via hydrogen bonding,[16] chain formation of heteropolyniobates, $[(Nb{=}O)GeNb_{12}O_{40}]^{16-}$,[17] speciation and stability of Co-POMs,[18] speciation and interactions of Hf clusters,[19,20] and the formation of larger macromolecules composed of smaller POMs.[21]

Simulating scattering curves from a POM's crystal structure provides the opportunity to directly compare solid state and solution species. There are a few

programs that are able to convert the single crystal x-ray structure into a simulated scattering curve.[22,23] These simulated curves can be analyzed and modeled in the same way as the experimental data. This provides a greater confidence in the conclusions drawn from SWAXS data.

SWAXS has been more frequently utilized in nanomaterial research, as well as biomolecules, but there is a growing number of chemists in the field of metal-oxo clusters who are exploring this technique. While there are many different applications of x-ray scattering, this thesis will focus on SWAXS studies of group V polyoxometalates to understand their behavior in the solution state.

(1) Schnablegger, H.; Singh, Y. *The SAXS Guide*; Second Rev.; Anton Paar, 2011.
(2) Putnam, C. D.; Hammel, M.; Hura, G. L.; Tainer, J. A. *Q. Rev. Biophys.* **2007**, *40*, 191–285.
(3) Guinier, A.; Fournet, G. *Small-Angle Scattering of X-rays*; 1955.
(4) Turkevich, J.; Hopkins Hubbell, H. *J. Am. Chem. Soc.* **1951**, *73*.
(5) Glatter, O.; Kratky, O. *Small Angle X-ray Scattering*; 1982.
(6) Feigin, L. A.; Svergun, D. I. *Structure Analysis by Small-Angle X-Ray and Neutron Scattering*; Springer Science: New York, New York, 1987.
(7) Pauw, B. R. Looking at Nothing-A weblog about small-angle scattering http://www.lookingatnothing.com/index.php/archives/1309.
(8) Nyman, M.; Fullmer, L. B. In *Trends in Polyoxometalates Research*; Ruhlmann, L.; Schaming, D., Eds.; Nova Science Publishers, Inc., 2015; pp. 151–170.
(9) Fan, L.; Degen, M.; Bendle, S.; Grupido, N.; Ilavsky, J. *J. Phys. Conf. Ser.* **2010**, *247*, 012005.
(10) Sécheresse, F. *Polyoxometalate Chemsitry: Some Recent Trends*; World Scientific Puublishing, 2013.
(11) Jackson, M. N.; Kamunde-Devonish, M. K.; Hammann, B. A.; Wills, L. A.; Fullmer, L. B.; Hayes, S. E.; Cheong, P. H.-Y.; Casey, W. H.; Nyman, M.; Johnson, D. W. *Dalt. Trans.* **2015**, *44*, 16982–17006.
(12) Fullmer, L. B.; Molina, P. I.; Antonio, M. R.; Nyman, M. *Dalt. Trans.* **2014**, *43*, 15295–15299.
(13) Antonio, M. R.; Nyman, M.; Anderson, T. M. *Angew. Chemie* **2009**, *48*, 6136–6140.
(14) Sures, D. J.; Sahu , S. K.; Molina, P. I.; Navrotsky, A.; Nyman, M. *ChemistrySelect* **2016**, *1*, 1858–1862.
(15) Kinnan, M. K.; Creasy, W. R.; Fullmer, L. B.; Schreuder-Gibson, H. L.; Nyman, M. *Eur. J. Inorg. Chem.* **2014**, 2361–2367.
(16) Kojima, T.; Antonio, M. R.; Ozeki, T. *J. Am. Chem. Soc.* **2011**, *133*, 7248–7251.

(17) Hou, Y.; Zakharov, L. N.; Nyman, M. *J. Am. Chem. Soc.* **2013**, *135*, 16651–16657.
(18) Goberna-Ferrón, S.; Soriano-López, J.; Galán-Mascarós, J. R.; Nyman, M. *Eur. J. Inorg. Chem.* **2015**, *2015*, 2833–2840.
(19) Goberna-Ferrón, S.; Park, D.-H.; Amador, J. M.; Keszler, D. A.; Nyman, M. *Angew. Chemie Int. Ed.* **2016**, 1–5.
(20) Ruther, R. E.; Baker, B. M.; Son, J.-H.; Casey, W. H.; Nyman, M. *Inorg. Chem.* **2014**, *53*, 4234–4242.
(21) Pigga, J. M.; Teprovich, J. A.; Flowers, R. A.; Antonio, M. R.; Liu, T. *Langmuir* **2010**, *26*, 9449–9456.
(22) Zuo, X.; Goshe, A.; Zhang, R.; Tiede, D. M. *J. Appl. Crystallogr.*
(23) Svergun, D. I. *Biophys. J.* **1999**, 2879–2886.

3 NIOBIUM AND TANTALUM

The transition metals niobium and tantalum were discovered at the turn of the 19th century, by English chemist Charles Hatchett, in the form of impure oxides, which he named Columbium. Initially, it was thought that tantalum and columbium were one and the same. A half century later, niobium and tantalum were isolated and recognized as separate elements. Swedish chemist Anders Gustaf Ekeberg named tantalum after the son of Zeus, Tantalus, in Greek mythology. Niobium was named by Heinrich Rose for Niobe, the daughter of Tantalus.[1,2]

In 1905, tantalum was prepared in a ductile form for the first time, where it garnered attention for its commercial use as filaments and chemically-resistant coatings. Around 1940 niobium found its use as an additive in stainless steel manufacturing, and as a superconducting alloy.[1,2]

As neighbors in group V of the periodic table, niobium and tantalum share many similarities, especially owing to the lanthanide contraction. Niobium and tantalum are the second most similar elements after zirconium and hafnium, in relation to insertion of the lanthanide elements between the 4d and 5d rows. Despite the molar mass of tantalum being nearly two times larger than niobium (180.9 and 92.9 g/mol respectively), the atomic radius is identical (1.45 Å). They exist in the same 5^+ oxidation state in aqueous solution and have similar electronegativities (1.5 and 1.6 for Nb and Ta respectively).[3] Nb and Ta can be found in nature together in the mineral coltan (**figure 3.1**).

Figure 3.1. A piece of coltan, the metallic ore from which niobium and tantalum are extracted.[4]

3.1 NIOBIUM AND TANTALUM IN SOLUTION

Niobium and tantalum metals can be dissolved in nitric and hydrofluoric acid mixtures, as well as hydrochloric acid, which are classical routes to extract the metals from the natural ores.[5,6] Extraction with hydrofluoric acid separates the elements by forming the fluoro-salts K_2TaF_7 and K_2NbOF_5, which are quite insoluble and crystallize separately. In pure hydrochloric acid, chloro- complexes such as MCl_6^-, MCl_5 and MCl_3 are formed. With the addition of water, these chlorides hydrolyze to form hydrous niobic and tantalic acids, $M_2O_5 \cdot nH_2O$, with very limited solubility.[1,6]

In the early 1900's, Balke discovered that niobium and tantalum pentoxides were soluble in alkaline media with hydrogen peroxide. It was determined that the species in solution were fully peroxylated metal anions, $[M(O_2)_4]^{3-}$.[1,7,8] Since the peroxometalate discovery, a wide range of such compounds have been reported. This is partially due to the diversity of available counterions but also the ability to incorporate other ligands alongside the peroxide. Speciation includes halide complexes, mono- to multi-dentate substituted complexes, carboxylates, and heterocyclic complexes. A complete summary of niobium and tantalum peroxometalate compounds can be found in the review by Bayot and Devillers.[5]

The aqueous chemistry of niobium and tantalum is quite limited outside of the alkaline pH range due to insolubility. Baes and Mesmer report Pourbaix diagrams (**figure 3.2**) for the metals which indicate a lack of NbO_4^{3-} and TaO_4^{3-} salts since the Nb^{5+} and Ta^{5+} ions are too small to remain in a tetrahedral configuration in solution.[9,10] Niobium and tantalum prefer the V+ oxidation state in solution and form octahedral coordination complexes. In alkaline solutions, the predominant species for both metals are the hexanuclear $[M_6O_{19}]^{8-}$ ion, of which the solid state structure was first determined by Lindqvist in 1953[11] and later observed in solution by Nelson and Tobias.[12]

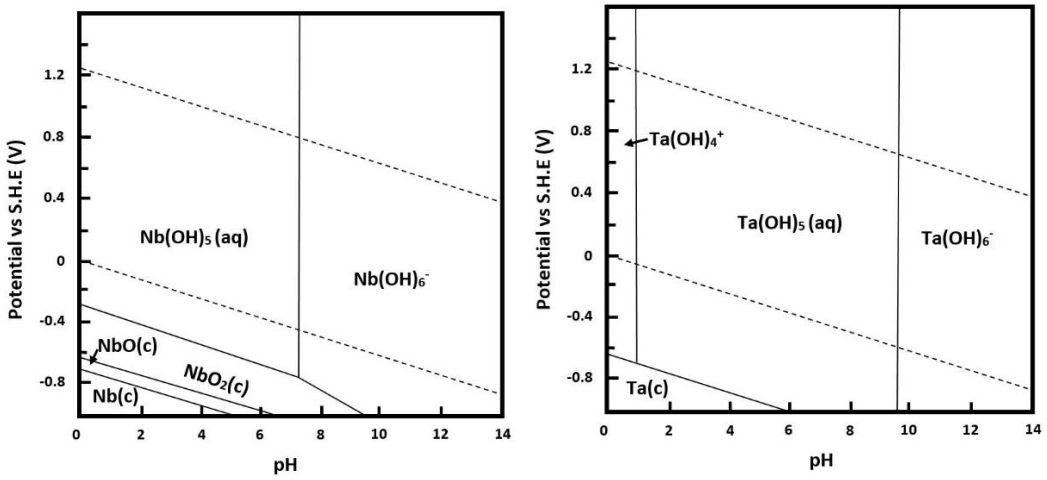

Figure 3.2. Pourbaix diagrams of potential (with respect to the standard hydrogen electrode) vs pH for aqueous niobium and tantalum at 10^{-6} m.

Niobium solution chemistry has been drastically expanded in recent years due to its greater solubility compared to tantalum. By altering the pH, among other solution conditions, additional polynuclear species can be formed other than the hexametalate Lindqvist ion. Polynuclear metal oxide species, such as $Ta_{10}O_{28}^{6-}$, $Nb_{10}O_{28}^{6-}$, $H_xNb_{24}O_{72}^{x-24}$, and $XNb_{12}O_{40}$, are classified as polyoxometalates. As discussed in a previous chapter, these clusters require counter cations for charge balancing. The counter cations can have vastly different effects on the solubility, ranging from aqueous to organic. Precursors to the metal oxide clusters of Nb and Ta include the hydrous pentoxides, pentachlorides, peroxides, and alkoxides. The speciation is primarily limited to the alkaline range since below neutral pH the oxides will precipitate.

3.2 NIOBIUM AND TANTALUM IN THE SOLID STATE

When niobium and tantalum metals are fully oxidized in the presence of excess oxygen and high temperatures, the end products are the pentoxides Nb_2O_5 and Ta_2O_5 which are the most common and thermodynamically stable compounds of these metals. The structures of these oxides have been a matter of some debate as there are many polymorphs. It is generally accepted that both pentoxides have two distinct phases: low

temperature and high temperature.[1,13] Niobium pentoxide and tantalum pentoxide have shown great potential in many technological applications.

Niobium pentoxide is a wide band gap semiconductor or insulator with a band gap around 3.4 eV. It has a high dielectric constant making it a candidate for metal-oxide-semiconductor (MOS) or metal-insulator-metal (MIM) devices.[14] Nb_2O_5 also has photochromic and electrochromic properties, meaning it can change colors by applying a voltage. This property can be applied to "smart windows" or dynamic tintable windows,[14] where the solar factor and/or radiation transmission can be changed in response to an electric current or changing environmental conditions. These tintable windows can help reduce the energy consumption of buildings by reducing the cooling and heating needs.[15] Hydrated niobium pentoxide has been used as a catalyst in reactions such as esterification, alkylation, and condensation/dehydration. Other applications include lithium batteries, sensors, coatings, optics, and more recently for resistive random access memory (ReRAM) or memristors.[14,16]

Tantalum pentoxide started receiving attention nearly 50 years ago due to its antireflective properties but became more popular in the 1990's as the development of electronics started taking off. Ta_2O_5 is an electrical insulator with a high dielectric constant. In its crystalline form, tantalum pentoxide thin films have piezoelectric properties.[17] The films are very stable, and can be used to make camera lenses due to a high index of refraction.[2] Ta_2O_5 can also be used as a pH-sensitive membrane in ion-sensitive field effect transistors, and as a detector for proteins utilizing immunochemical binding reactions.[17] The stability of these metal oxide films finds use in resistive switching memory.[18] Tantalum is extremely resistant to corrosion and inert to body fluids, therefore it can be used in materials for surgical uses such as bone repair and internal sutures.[5]

(1) Fairbrother, F. *The Chemistry of Niobium and Tantalum*; Elsevier Publishing Company, 1967.
(2) *CRC Handbook of Chemistry and Physics*; Lide, D. R.; Haynes, W. M., Eds.; 90th ed.; CRC Press (Taylor and Francis Group): Boca Raton, FL, 2009.

(3) www.materialsproject.org.
(4) Wikipedia Contributors. Coltan https://en.wikipedia.org/w/index.php?title=Coltan&oldid=736973211 (accessed Sep 9, 2016).
(5) Bayot, D.; Devillers, M. *Coord. Chem. Rev.* **2006**, *250*, 2610–2626.
(6) Gates, J. M.; Sudowe, R.; Stavsetra, L.; Ali, M. N.; Calvert, M. G.; Dragojević, I.; Ellison, P. A.; Garcia, M. A.; Gharibyan, N.; Gregorich, K. E.; Nelson, S. L.; Neumann, S. H.; Parsons-Moss, T.; Nitsche, H. *Radiochim. Acta* **2009**, *97*, 167–172.
(7) Balke, C. W.; Smith, E. F. *J. Am. Chem. Soc.* **1908**, 1637–1668.
(8) Balke, C. W. *J. Am. Chem. Soc.* **1905**, 1689–1699.
(9) Baes, C. F.; Mesmer, R. E. *The Hydrolysis of Cations*; John Wiley & Sons, Inc., 1976.
(10) Nyman, M. *Dalt. Trans.* **2011**, *40*, 8049–8058.
(11) Lindqvist, I. *Ark. Kemi* **1953**, *5*, 247.
(12) Nelson, W. H.; Tobias, R. S. *Can. J. Chem.* **1964**, *42*, 731.
(13) Reisman, A.; Holtzberg, F. In *High Temperature Oxides Part II: Oxides of Rare Earths, Titanium, Zirconium, Hafnium, Niobium, and Tantalum*; Alper, A. M., Ed.; Academic Press Inc: New York, New York, 1970; pp. 217–255.
(14) Nico, C.; Monteiro, T.; Graça, M. P. F. *Prog. Mater. Sci.* **2016**, *80*, 1–37.
(15) Baetens, R.; Jelle, B. P.; Gustavsen, A. *Sol. Energy Mater. Sol. Cells* **2010**, *94*, 87–105.
(16) Rani, R. A.; Zoolfakar, A. S.; O'Mullane, A. P.; Austin, M. W.; Kalantar-Zadeh, K. *J. Mater. Chem. A* **2014**, *2*, 15683–15703.
(17) Chaneliere, C.; Autran, J. L.; Balland, B.; Devine, R. A. B.; Balland, B. *Reports A Rev. J.* **1998**, *22*, 269–322.
(18) Prakash, A.; Jana, D.; Maikap, S. *Nanoscale Res. Lett.* **2013**, *8*, 418.

4 INORGANIC THIN FILMS

A thin film is defined as a nanometer to micrometer thick layer of a material that can be deposited onto a substrate for various applications. Thin films are utilized in many different aspects of our lives, including the metallic layer on glass forming a mirror that we look at daily; corrosion resistant coatings on tools; semiconductors, insulators, and integrated circuits found in all of our electronic devices; and solar cells.

In the microelectronics industry, integrated circuits have been scaling down as consumers demand smaller and more compact electronics, but the minimum size limit is being reached. There is a need for high dielectric insulators which can be scaled down to increase the packing density of devices.[1] The design of capacitors has moved from planar to three dimensional structures, allowing the chip area to increase as the feature size decreases.[1] In the 1960's, Moore noted that the dimensions of the chip are reduced by 50% every year and a half , and predicted that this doubling of the transistor density will continue to scale in this manner. This became known as Moore's law.[2]

4.1 MOTIVATION FOR SOLUTION PROCESSING

Thin films can be fabricated by a number of methods, some of which include anodic or thermal oxidation, vacuum evaporation, sputtering, chemical vapor deposition, atomic layer deposition, ion-assisted deposition, and sol-gel.[1] Evaporation and sputtering deposition techniques require the system to be under vacuum at low pressure. Sputtering involves bombarding a target with ions which causes atoms at the surface of the target to be released and transported to the substrate. Chemical vapor deposition (CVD) involves thermal decomposition or reaction of gases to deposit the material directly from the gas phase onto the surface of a substrate. CVD can be performed under reduced pressures or atmospheric pressure with high temperature, or in a plasma reactor.[3] There is a need to develop more energy efficient, cost effective, sustainable methods for thin film fabrication.

The Center for Sustainable Materials Chemistry (CSMC) is a Phase-II National Science Foundation Center for Chemical Innovation, where eight academic institutions

collaborate in materials chemistry research. The CSMC conducts curiosity driven and use-inspired research to address the need of scaling down for semiconductor industry. Researchers in the CSMC are exploring solution based methods for processing thin films of high quality, with the goal of producing leading-edge results for the next generation of semiconductor products.[4]

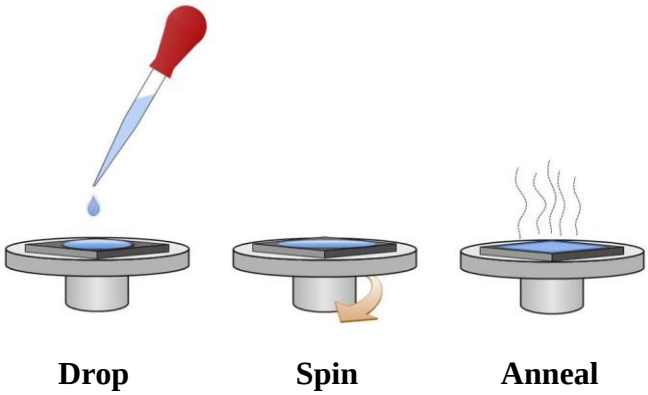

Figure 4.1. Graphical depiction of the spin coating method where a precursor solution is added dropwise onto a substrate, spun to evenly distribute the solution, and annealed to drive off the solvent.

Solution processing such as spin coating, dip coating, or mist deposition is a low cost, low energy consuming method that can easily be scaled up to mass produce films in a more sustainable manner. A large component of the research in the CSMC utilizes metal oxide/hydroxide clusters, with a focus on groups 4, 5, 6, 13, and 14 metals as the precursors to forming metal oxide thin films.[5–8]

4.1.1 Metal-Oxide Clusters as Precursors

Metal oxide/hydroxide clusters such as polyoxometalates and polyoxocations can be dissolved in nontoxic solvents such as water and deposited on a substrate via spin coating. Upon solvent evaporation and annealing, the metal oxide/hydroxide clusters are converted into an amorphous or crystalline metal oxide film. Controlling the anneal temperature and conditions affects the final film morphology and properties. By using a metastable oxo/hydroxo framework, smooth hydrated films can dehydrate and condense to form amorphous networks that are free of defects and pores.

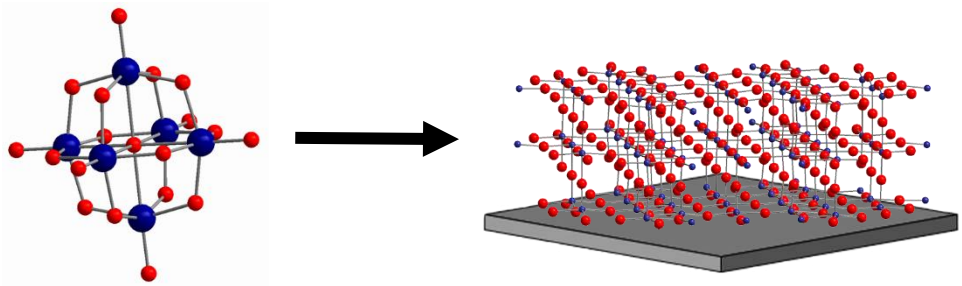

Figure 4.2. Representation of metal oxide cluster to metal oxide thin film.

Some examples of work to emerge from CSMC research include various doped aluminum oxide films for dielectrics[9–11], hafnium/zirconium oxide sulfate for photoresists[12], cobalt iron oxide for magneto-electric devices[13], indium-gallium-zinc-oxide for thin film transistors[14], as well as the work reviewed in this thesis on niobium and tantalum oxide films.[15,16]

Solution processing for amorphous metal oxide films is preferred over classical deposition techniques because it is a low temperature process, it can be applied to flexible substrates, and the performance and quality can surpass those from vapor deposition.[17,18] Polyoxometalates provide control over the film's morphology and composition because they can be produced without impurities and contain only the metal-oxide cluster and counterions. Counterions can either be incorporated into the film composition or removed during annealing through decomposition or with various treatments such as acidification. A precursor solution of lithium hexaniobate ($Li_{(8-x)}H_xNb_6O_{19}\cdot nH_2O$) can be annealed to form a thin film of Li_3NbO_4 or $LiNbO_3$ depending on the protonation state of the cluster and subsequent number of lithium counterions.[19] Small organic counterions can be removed during the annealing process and are therefore not incorporated into the final film composition. Tetramethylammonium hexaniobate and hexatantalate are examples of this type of film formation, where the final thin film is amorphous M_2O_5 after decomposition of tetramethylammonium.[15,16]

(1) Chaneliere, C.; Autran, J. L.; Balland, B.; Devine, R. A. B.; Balland, B. *Reports A Rev. J.* **1998**, *22*, 269–322.
(2) Seshan, K. *Handbook of Thin Fim Deposition: Techniques, Processes, and Technologies*; William Andrew, 2012.
(3) Jaeger, R. C. *Introduction to Microelectronic Fabrication*, 2nd ed.; Prentice Hall: Upper Saddle River, NJ, 2002.
(4) Center for Sustainable Materials Chemistry http://sustainablematerialschemistry.org/ (accessed Jun 28, 2016).
(5) Meyers, S. T.; Anderson, J. T.; Hong, D.; Hung, C. M.; Wager, J. F.; Keszler, D. A. *Chem. Mater.* **2007**, *19* (16), 4023–4029.
(6) Anderson, J. T.; Munsee, C. L.; Hung, C. M.; Phung, T. M.; Herman, G. S.; Johnson, D. C.; Wager, J. F.; Keszler, D. A. *Adv. Funct. Mater.* **2007**, *17* (13), 2117–2124.
(7) Son, J.-H.; Park, D.-H.; Keszler, D. A.; Casey, W. H. *Chem. - A Eur. J.* **2015**, *95616*, n/a-n/a.
(8) Oleksak, R. P.; Ruther, R. E.; Luo, F.; Fairley, K. C.; Decker, S. R.; Stickle, W. F.; Johnson, D. W.; Garfunkel, E. L.; Herman, G. S.; Keszler, D. A. *Appl. Mater. Interfaces* **2014**, *6*, 2917–2921.
(9) Anderson, J. T.; Wang, W.; Jiang, K.; Gustafsson, T.; Xu, C.; Garfunkel, E. L.; Keszler, D. A. *ACS Sustain. Chem. Eng.* **2015**, 150508135053001.
(10) Smith, S. W.; Wang, W.; Keszler, D. A.; Conley, J. F. *J. Vac. Sci. Technol. A Vacuum, Surfaces, Film.* **2014**, *32* (4), 41501.
(11) Plassmeyer, P. N.; Archila, K.; Wager, J. F.; Page, C. J. *ACS Appl. Mater. Interfaces* **2015**, *7* (3), 1678–1684.
(12) Amador, J. M.; Decker, S. R.; Lucchini, S. E.; Ruther, R. E.; Keszler, D. A. *Proc. SPIE* **2014**, *9051* (scheme 1), 90511A–90511A–6.
(13) Richter, P.; Plassmeyer, P. N.; Harzdorf, J.; Rüffer, T.; Lang, H.; Kalbacova, J.; Jöhrmann, N.; Schulze, S.; Hietschold, M.; Arekapudi, S. S. P. K.; Albrecht, M.; Zahn, D. R. T.; Page, C. J.; Salvan, G. *Chem. Mater.* **2016**, *28* (14), 4917–4927.
(14) Chiang, T.; Yeh, B.; Wager, J. F. *IEEE Trans. Electron Devices* **2015**, *62* (11), 3692–3696.
(15) Mansergh, R. H.; Fullmer, L. B.; Park, D.-H.; Nyman, M.; Keszler, D. A. *Chem. Mater.* **2016**, acs.chemmater.6b00078.
(16) Fullmer, L. B.; Mansergh, R. H.; Zakharov, L. N.; Keszler, D. A.; Nyman, M. *Cryst. Growth Des.* **2015**, *15* (8), 3885–3892.
(17) Jiang, K.; Zakutayev, A.; Stowers, J.; Anderson, M. D.; Tate, J.; McIntyre, D. H.; Johnson, D. C.; Keszler, D. A. *Solid State Sci.* **2009**, *11* (9), 1692–1699.
(18) Llordés, A.; Wang, Y.; Fernandez-Martinez, A.; Xiao, P.; Lee, T.; Poulain, A.; Zandi, O.; Saez Cabezas, C. A.; Henkelman, G.; Milliron, D. J. *Nat. Mater.* **2016**, *1* (August 2016).
(19) Hou, Y.; Fast, D. B.; Ruther, R. E.; Amador, J. M.; Fullmer, L. B.; Decker, S. R.; Zakharov, L. N.; Dolgos, M. R.; Nyman, M. *J. Solid State Chem.* **2015**, *221*, 418–425.

CHAPTER 5

Nb_2O_5 AND Ta_2O_5 THIN FILMS FROM POLYOXOMETALATE PRECURSORS: A SINGLE PROTON MAKES A DIFFERENCE

Lauren B. Fullmer, Ryan H. Mansergh, Lev N. Zakharov, Douglas A. Keszler, and May Nyman

Cryst. Growth Des. **2015**, *15*(8), Page 3885

5.1 ABSTRACT

Thin film materials from water-based precursors follow the principals of green chemistry, leading to a more sustainable future in the energy intensive era in which we currently reside. While simple in practice, aqueous metal- oxide chemistry is complex at the molecular level. Here we develop the first water-based formation of Nb_2O_5 and Ta_2O_5 thin films; utilizing tetramethylammonium salts of $[H_2Ta_6O_{19}]^{6-}$ and $[H_3Nb_6O_{19}]^{5-}$ polyoxometalates. Although the clusters are structurally identical group V analogues and differ only by a single proton, this difference has a considerable influence on the quality of the films that are obtained. Through characterization of the solid-state precursor (single-crystal X-ray diffraction), the aqueous precursor solution (X-ray scattering), and the thin films (atomic force and scanning electron microscopies, X-ray diffraction, and reflectivity), we rationalize the important roles of cluster protonation that carry through all chemical processes from the precursor to the metal oxide coating.

5.2 INTRODUCTION

Fabricating functional thin films from aqueous metal-oxo cluster precursors embodies several principals of green chemistry. Therefore, development of appropriate chemistries for materials broadly used in data storage, energy storage, and energy generation would provide technologies toward a sustainable future. Metal-oxo cluster chemistry that has been most substantially developed is that of the group V/VI polyoxometalates[1] and the group 13 polyoxocations.[2] Clusters of these chemical families can be isolated in discrete forms without the use of organic ligands to prevent irreversible precipitation of the related oxide. Therefore, these clusters are entirely inorganic, with only H_2O, OH^-, and O^{2-} for ligands. Water-solubility of metal-oxo clusters arises naturally from the positive or negative charge, which requires charge-balancing counterions. By necessity, counterions are incorporated into a film that is spun-cast from aqueous solution, and therefore removal of these counterions must be carried out with enhancement, rather than degradation of the fundamental film characteristics that include density, continuity, compositional and phase purity, interfacial homogeneity, and smoothness. Thus, ideal counterions are preferably small and volatile and/or combustible at a low temperature. Suitable counterions for accomplishing this ideal end-product include cations H^+, NH_4^+, and $N(CH_3)_4^+$; or anions NO_3^-, SO_4^{2-}, or CO_3^{2-}.

Less suitable counterions include bulky organics that would leave large voids in the film upon removal, or that cannot be completely removed; or nonvolatile counterions such as alkalis or halides.

Thin films of group V metal oxides (Ta_2O_5 and Nb_2O_5) are of significant technological relevance owing to their favorable chemical, thermal, and mechanical properties.[3] They have a number of potential uses in advanced electronics as high-κ dielectric materials[4] or as diffusion barriers.[5] More recently, Ta_2O_5 has been coveted as a robust memristive material.[6] Prior solution deposition of Ta_2O_5 and Nb_2O_5 films was achieved by utilizing nonaqueous alkoxide or halide solutions.[7–11] These molecular precursors are moisture sensitive and react with exposure to ambient air; the degree of reaction is variable with temperature, humidity, and time. Therefore, the speciation of these precursors changes with time, which is not amenable to reproducible and reliable thin film deposition. Also starting with tantalum alkoxide, Sone and co-workers prepared an aqueous acidic-peroxide solution for the deposition of Ta_2O_5.[12] However, this solution both requires the decomposition of excess peroxide using platinum and is not stable, as it continuously precipitates tantalum oxide. Again this leads to irreproducibility of film quality and characteristics. Therefore, reliable aqueous routes to Ta_2O_5 and Nb_2O_5 thin films have not yet been realized. The group V Lindqvist ion polyoxometalates ($[H_xTa_6O_{19}]^{(8-x)-}$ and $[H_xNb_6O_{19}]^{(8-x)-}$ -- hexatantalate and hexaniobate, respectively) are robust, highly water-soluble, isostructural clusters featuring a superoctahedron of six mutually edge-sharing octahedra (**figure 5.1**) and are ideal for developing routes to Ta_2O_5 and Nb_2O_5 thin film materials that are (1) entirely water-based and (2) executed in ambient conditions.

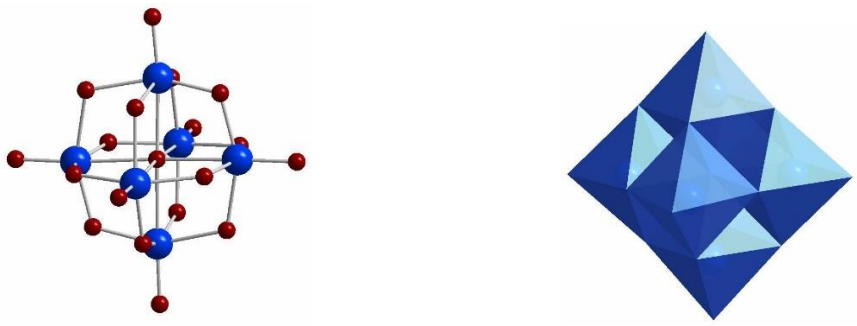

Figure 5.1. Ball and stick model (left) and polyhedral representation (right) of the $[M_6O_{19}]^{8-}$ (M=Nb,Ta) Lindqvist ion. Red spheres are oxygen, blue spheres are Nb or Ta; blue polyhedra are MO_6.

Of the potential countercations listed above, only $N(CH_3)_4^+$ (TMA or tetramethylammonium) or a mixture of $N(CH_3)_4^+$ and H^+ are suitable. NH_4^+ produces an insoluble salt, and due to the limited pH stability range of these clusters (>11), only up to three H^+ counterions are possible.[13,14] While the TMA salt of hexaniobate has been made and structurally characterized,[15] a TMA salt of hexatantalate has not yet been reported. While Matsumoto and co-workers have successfully synthesized tetrabutylammonium salts of hexatantalate and the first decatantalate structure, they were from non-aqueous methods.[16–18] Here, we report synthesis and structural characterization of both TMA-hexatantalate, and a TMA-hexaniobate (modified from the literature procedure). Thin films produced from these analogous cluster precursors differ notably in quality: while hexatantalate produced Ta_2O_5 thin films of remarkable density and smoothness, Nb_2O_5 films produced from hexaniobate were rough. This was surprising, given the similarity of the precursors and the general periodic relationship between Nb and Ta. By small and wide-angle X-ray scattering studies (SWAXS) of aqueous solutions of the clusters, and noting the protonation state of the clusters and the influence on crystallization behavior and subsequent thin film characteristics, we hypothesized the dissimilar results to be simply the differing protonated states of the two group V analogues. More broadly, it is noted that a seemingly innocuous difference can strongly influence chemical processes and, ultimately, performance of functional materials.

5.3 EXPERIMENTAL SECTION

5.3.1 GENERAL METHODS AND MATERIALS

H_2O_2 (30%), isopropyl alcohol (ACS grade), and NH_4OH (28.0−30.0% as NH_3, ACS grade) were purchased from Macron Fine Chemicals. $TaCl_5$ (99.99%), and $(CH_3)_4NOH$ (25% w/w aq. solution, 99.9999%) were purchased from Alfa Aesar. TGA/DSC scans were performed in air as well as argon from 20 to 900 °C with a ramp rate of 10 °C·min^{-1} using a TA Instruments SDT Q600. Infrared spectra (400−3500 cm^{-1}) were collected on a Thermo Scientific Nicolet iS10 with a Smart Orbit Diamond ATR accessory. Small and wide-angle X-ray scattering was collected at beamline 12-ID-B at the Advanced Photon Source at Argonne National Lab. The samples and appropriate backgrounds were collected with a flow through quartz capillary (1.5 mm) cell for 20 scans using incident energy of 14 keV and a sample to detector distance of 2 m. WaveMetrics Igor Pro software with Irena macros was used for analyzing the SWAXS data.[19] SolX software was used for creating simulated scattering curves.[20,21] Radius and interparticle interactions were determined for each sample and the simulated data by using a fitting method of least-squares. Elemental composition was determined by Galbraith Laboratories, Inc. (Knoxville, TN) through the use of inductively coupled plasma atomic emission spectroscopy (ICP-AES; Nb and Ta) and a Thermo Finnigan FLASH 2000 Elemental Analyzer (C, H, N).

Single crystal X-ray diffraction experiments for **Nb6** and **Ta6** were carried out on a Bruker Smart Apex diffractometer at 173(2) K and 150(2) K, respectively, using Mo Kα radiation (λ = 0.71073 Å). Absorption corrections were applied by SADABS.[22] Space groups were determined based on the intensity statistics. The structures were solved using direct methods with calculations of difference Fourier maps and refined with full-matrix least-squares methods based on F2. Non-hydrogen atoms were refined with anisotropic thermal parameters except those in one of the $N(CH_3)_4$ cations in **Nb6** disordered around an inversion center. The H atoms in both structures were treated in calculated positions and refined in a rigid group model. H atoms in the $Nb_6O_{19}H$ anion in **Nb6** were not found. In the structure of **Nb6**, there are five $N(CH_3)_4$ cations: three of them are located in general positions, and two are disordered over two positions around inversion centers. In **Nb6**, there are 13 solvent water molecules, 7 of them are disordered and form a hydrogen-

bonded network. These disordered solvent molecules were treated by SQUEEZE;[23] correction by SQUEEZE is 201 electrons/cell, the required value is 130 electrons/cell. The number of solvent water molecules evaluated based on the single crystal structure agrees with thermal analysis data. All calculations were performed using the SHELXTL (v 6.10) package.[24]

For the film deposition and analysis, n-type silicon (100) wafers, purchased from Sumco, OR USA, were used. The substrates were rinsed in Millipore 18.2 MΩ deionized water, dried in argon, and then ashed in an O_2 plasma for 10 min at 200 W and ~175 mTorr. The films were spun using a CEE Model 100 spin coater at 3000 rpm for 30 s. The films were soft baked on a hot plate at 200 °C for 1 min. The samples were then annealed in air using Neytech Qex furnaces with a 20 °C $\cdot min^{-1}$ ramp rate.

X-ray diffraction (XRD) and X-ray reflectivity (XRR) were both performed on a Rigaku Ultima-IV diffractometer with Cu Kα radiation (λ = 1.5409 Å). For XRR data collection, the instrument was configured with a 5.0° incident Soller slit, a 10 mm divergent height limiting slit, and a 5.0° receiving Soller slit; the divergent slit, scattering slit, and receiving slit were set to 0.2, 0.5, and 0.2 mm, respectively. Out-of-plane scans were performed for phase identification; XRR results were used to determine the appropriate ω value for out-of- plane scans. For these scans, the instrument was configured with a 5.0° incident Soller slit, a 10 mm divergent height limiting slit, and a 0.5° parallel beam slit; the divergent slit was set to 0.2 mm and the scattering slit and receiving slit were left open. The Rigaku software packages PDXL and GlobalFit were used for the analysis of XRD and XRR data, respectively.

Atomic force microscopy (AFM) measurements were performed on a Veeco Innova SPM and a Digital Instruments NanoScope III in tapping mode with silicon AFM probes (300 kHz, 40 $N \cdot m^{-1}$). Initial sample scans were performed on 1 × 1 μm^2 areas and later scans were performed on 20 × 20 μm^2 areas. Root-mean-square roughness values were obtained by analyzing data from multiple 2 × 2 μm^2 sections of the larger 20 × 20 μm^2 scan with Bruker NanoScope Analysis software. Scanning electron microscopy (SEM) images were collected on an FEI NOVA NanoSEM 230 high resolution microscope.

5.3.2 SYNTHESIS.

$(NH_4)_3Ta(O_2)_4$. The synthesis for ammonium peroxotantalate, $(NH_4)_3Ta(O_2)_4$, was adapted from previous methods.[25] $TaCl_5$ (2.4 g) was dissolved in 40 mL of 30% H_2O_2 in an ice water bath. With moderate stirring throughout the entire reaction, the solution was kept between 5 and 15 °C. A total of 12 mL NH_4OH (14.5 M) was added in ~1 mL aliquots. The solution became cloudy with early additions of NH_4OH; however, once the entire 12 mL is added, the solution became clear. Upon addition of ethanol (approximately 150 mL) the solution yielded a white precipitate. This precipitate was then vacuum-filtered with a Büchner funnel and washed with ethanol. The yield is between 97 and 100%.

$[(CH_3)_4N]_6[H_2Ta_6O_{19}]$ $21H_2O$ (Ta6). The synthesis for **Ta6** was adapted from the synthesis of alkali hexatantalates.[26] A 125 mL flask was charged with $(NH_4)_3Ta(O_2)_4$ (1.32 g) and 1.4 M tetramethylammonium hydroxide (8.25 mL). The solution was refluxed for 5 h with the condensing column chilled to approximately 5 °C. The resulting solution was filtered with a 0.45 μm nylon syringe filter. The filtered solution was agitated with isopropyl alcohol (~40 mL) and centrifuged to yield a small denser layer containing the product. Further agitation of the bottom layer with isopropyl alcohol (~30 mL) yielded a white precipitate. The precipitate was washed with isopropyl alcohol and oven-dried under vacuum (~60 °C). The yield is between 38% and 63%. Elemental analysis found C 13.59%, H 4.90%, N 3.62%, and Ta 46.9%.

$[(CH_3)_4N]_5[H_3Nb_6O_{19}]$ $20H_2O$ (Nb6). The synthesis for **Nb6** was adapted from the synthesis of alkali hexaniobates.[27] A 150 mL beaker was charged with tetramethylammonium hydroxide solution (2.8 M, 100 mL) and heated to 90 °C. Hydrous Nb_2O_5 (20 g) was added in small aliquots, allowing full dissolution before addition of new aliquots. After addition of all the niobium oxide, the solution was allowed to cool to room temperature. Isopropyl alcohol was added to precipitate the final product. After excessive washing with isopropyl alcohol, a white crystalline powder is obtained through vacuum filtration. The yield is between 94% and 100%. Elemental analysis found C 16.80%, H 6.63%, N 4.74%, and Nb 25.9%.

5.4 RESULTS AND DISCUSSION

5.4.1 Nb_2O_5 AND Ta_2O_5 THIN FILMS.

Thin films were prepared from spin coating 0.22 M (with respect to the cluster) aqueous solutions of the TMA hexametalate salts on n-type silicon wafers. The films were annealed at 400, 600, and 800 °C and then characterized using various methods including XRD, XRR, SEM, and AFM. These anneal temperatures were chosen based on TGA/DSC analysis of the powder samples. Thermal analysis revealed that all water and TMA is mostly driven out of the samples by 400 °C and predominantly metal oxide remains. However, Nb_2O_5 crystallizes at 600 °C, accompanied by a sharp weight-loss event; Ta_2O_5 crystallizes at 800 °C with a similar weight-loss event (**figure 5.2**). Prior to the sharp weight loss is a symmetric shallow decrease/increase in weight (in air). This is a result of a complicated decomposition of the TMA cation, which will be published elsewhere. When the samples are heated in an oxygen-free, inert atmosphere such as argon, we do not see this behavior, and a black powder is obtained, as opposed to the white powder from air calcination. The volatilization of water and TMA are associated with endothermic peaks, while crystallization of the oxide is an exothermic reaction.

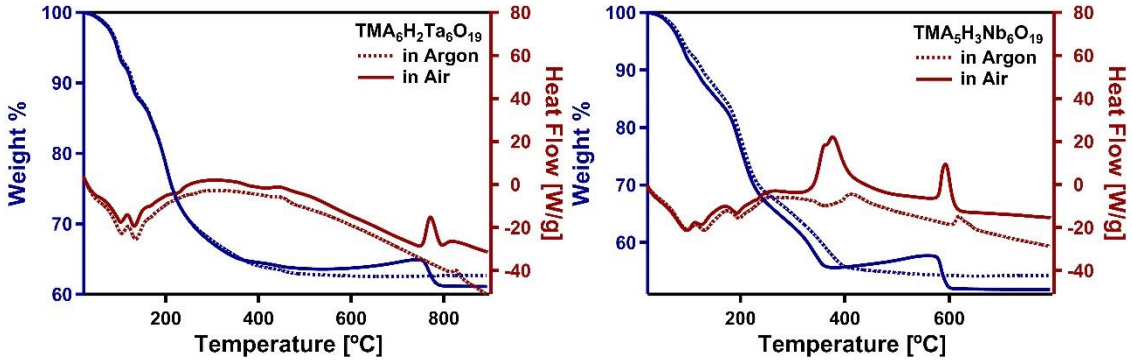

Figure 5.2. TGA-DSC analysis of powder **Ta6** (left) and **Nb6** (right). Red lines correspond with heat flow, blue lines correspond with weight percent. Dotted line is experimental data in argon gas while solid line is in air.

Thermal analysis of the samples revealed 17 water molecules for **Ta6** and 18 water molecules for **Nb6** which agrees closely with the crystallographic structure. Grazing incidence XRD revealed that the Nb_2O_5 and Ta_2O_5 films are crystalline at 600 and 800 °C, respectively (**figure A.1**), consistent with exothermic peaks at similar temperatures in the DSC analyses. Both Ta_2O_5 and

Nb_2O_5 films crystallize in the orthorhombic phase, with space groups Pmm2 (25) and Pbam (55) respectively. These crystallization temperatures are higher than what has been reported for Nb_2O_5 and Ta_2O_5 films from other deposition methods. Films deposited via plasma enhanced chemical vapor deposition crystallize at ~600−700 °C for Ta_2O_5 and ~400−500 °C for Nb_2O_5.[28]

The films were imaged using scanning electron microscopy (SEM) in order to visually determine relative thickness and roughness (**figure 5.3a**). Ta_2O_5 films were shown to have continuous, atomically smooth surfaces regardless of anneal temperature, while Nb_2O_5 film roughness varied with anneal temperature. The 400 °C annealed film for Nb_2O_5 has roughness values comparable with the Ta_2O_5 film despite observable differences by eye. However, at higher temperatures the quality of the films degraded and the change in morphology was noticeable. The 600 and 800 °C anneals of Nb_2O_5 had a considerable increase in roughness.

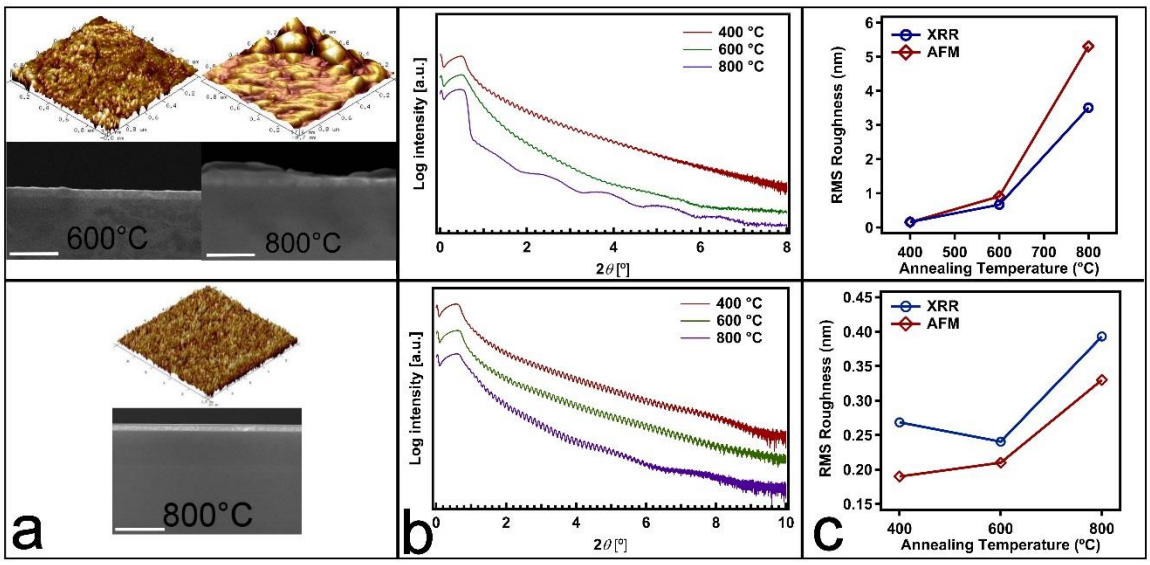

Figure 5.3. Nb_2O_5-Top, Ta_2O_5-bottom **a.** AFM and SEM. The white scale bar is 500 nm. **b.** X-ray reflectivity **c.** Comparison of XRR derived and AFM roughness values

The qualitative observations from SEM were verified quantitatively with atomic force microscopy (AFM) and X- ray reflectivity (XRR). Through modeling XRR data, values for roughness, density, and thickness are generated. The period of oscillations of the Kiessing fringes is dependent on film thickness, where the shorter the period the thicker the film. The amplitude of

the oscillations depends on the difference between the densities of the film and its substrate. The roughness of a film can be determined by the 2θ angle at which the fringes decay. A decay of the reflected X-rays at lower 2θ means the film has a larger surface roughness.[29] By comparing the XRR for Ta_2O_5 and Nb_2O_5 in **Figure 5.3b**, it is apparent that the Nb_2O_5 films are less dense and considerably rougher. The fringes in the Ta_2O_5 films are distinguishable until 2θ values of 8−9° in some cases. However, in the Nb_2O_5 films the fringes decay much earlier, around 5−6°. The roughness values obtained from XRR and AFM are compared in **Figure 5.3c**; both methods quantitatively show greater roughness in the Nb_2O_5 films.

5.4.2 TA6 AND NB6 CLUSTERS.

Both **Ta6** and **Nb6** are obtained as single crystals by dissolution in water followed by slow evaporation. The experimental powder X-ray diffraction patterns of the bulk samples of **Ta6** and **Nb6** (**figures A.5 and A.6**) are consistent with the simulated patterns from the single crystal data (**figures A.3 and A.4**), indicating the single crystals that were analyzed are representative of the bulk. The single crystal structure of **Ta6** revealed a diprotonated hexametalate Lindqvist ion, $[H_2Ta_6O_{19}]^{6-}$, which is charge- balanced by six TMA countercations, all identified in the structure. On the other hand, **Nb6** consists of a triprotonated Lindqvist ion $[H_3Nb_6O_{19}]^{5-}$, balanced by five TMA counter- ions. Table 1 summarizes the crystallographic data for **Nb6** and **Ta6**. The central oxygen is bonded to the metal atoms via long M−O bonds of ∼2.4 Å. The terminal M−O bonds are all multiply bonded and therefore shorter (∼1.8 Å).

Table 5.1. Summary of crystallographic data and structure refinement for **Ta6** and **Nb6**.

Complex	**Ta6**	**Nb6**
Empirical Formula	$Ta_6O_{42.5}C_{24}H_{74}N_6$	$Nb_6O_{32}C_{24}H_{77}N_5$
Formula Weight (g/mol)	2212.55	1331.21
Crystal System	triclinic	triclinic
Space Group	P -1 (2)	P -1 (2)
a (Å)	12.7073(7)	13.719(6)
*b (*Å)	14.0596(7)	14.024(7)
c (Å)	20.903(1)	16.390(8)
α (˚)	71.310(1)	67.008(8)
β (˚)	76.972(2)	76.671(8)
γ (˚)	72.889(1)	84.904(9)
V (Å^3)	3345.40(32)	2825(2)
Z	2	2
T (K)	150	173
d (g·cm^{-3})	2.196	1.565
λ (Å)	0.71073	0.71073
μ (mm^{-1})	9.865	1.263

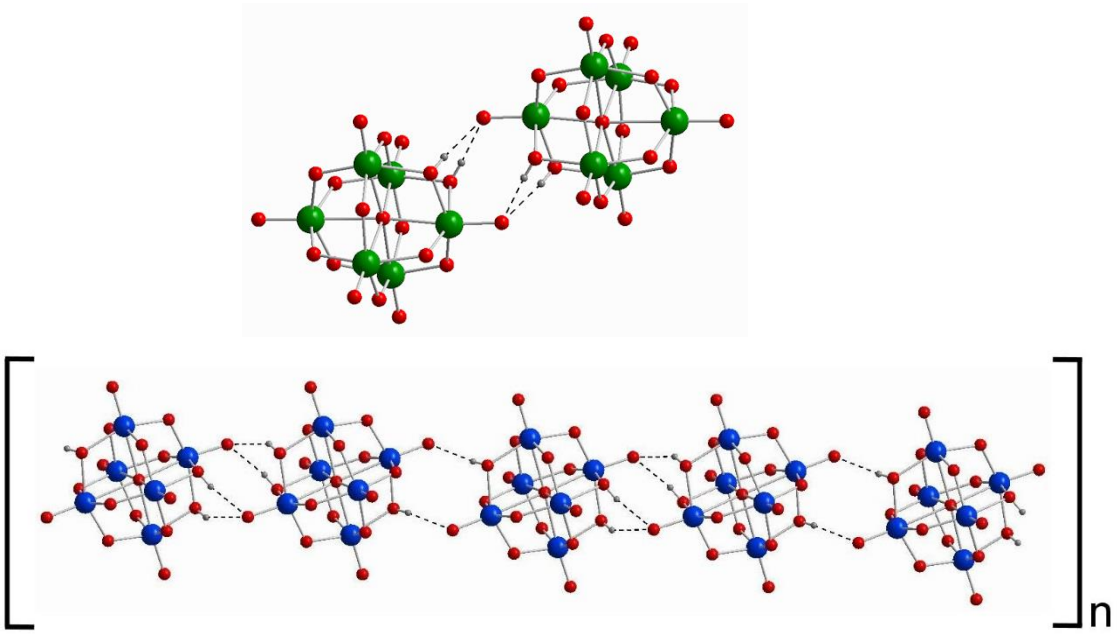

Figure 5.4. Representation of the hydrogen bonded clusters of **Ta6** (top) and **Nb6** (bottom).

Bridging oxos (M-O-M) typically exhibit bond lengths of 2.0 Å, but protonation is identified in both Ta6 and Nb6 with bridging M-O-M bond lengths of 2.1−2.2 Å. Ta6 has two protons which reside on neighboring bridging oxygens. For **Nb6**, there are likewise two protons on neighboring bridging oxygens and a third on an oxygen on the face trans to this doubly protonated face. The locations of these protons were determined by both bond length of the bridging oxygens and by bond valence sum (BVS) calculations (**tables 5.2 and 5.3**). Protonation of these clusters leads to characteristic dimeriza- tion via mutual hydrogen bonding of the protonated faces (**figure 5.4**). Finally, the third proton on the face trans to the doubly protonated face of **Nb6** results in assembly of the clusters into chains in the lattice. Reflecting this ion- arrangement macroscopically, the crystals of **Nb6** grow as long needles.

Table 5.2. Bond lengths and bond valence sum of oxygens in **Ta6** structure. * indicates protonated oxygens.

Bridging Oxygen	***Bond Lengths (Å)***		***BVS***
Ta2-O2-Ta1	1.922(2)	1.991(2)	1.879
Ta3-O3-Ta2	2.137(2)	2.157(2)	1.118*
Ta4-O4-Ta3	2.031(2)	1.900(2)	1.855
Ta4-O5-Ta1	1.971(2)	1.979(2)	1.779
Ta5-O6-Ta1	1.923(2)	1.992 (3)	1.874
Ta2-O7-Ta5	1.987(3)	1.995(2)	1.704
Ta3-O8-Ta5	2.128(3)	2.157(2)	1.132*
Ta5-O9-Ta4	1.961(2)	1.992(3)	1.774
Ta6-O10-Ta1	1.973(2)	1.984(3)	1.762
Ta2-O11-Ta6	1.956(3)	2.005(2)	1.757
Ta3-O12-Ta6	1.894(3)	2.030(2)	1.874
Ta6-O13-Ta4	1.963(2)	1.970 (3)	1.821
Terminal Oxygen	***Bond Length (Å)***		***BVS***
Ta1-O14	1.802(2)		1.420
Ta2-O15	1.805(2)		1.409
Ta3-O16	1.818(2)		1.360
Ta4-O17	1.799(2)		1.432
Ta5-O18	1.805(3)		1.409
Ta6-O19	1.801(3)		1.424

Table 5.3. Bond lengths and bond valence sum of oxygens in **Nb6** structure. * indicates protonated oxygens.

Bridging Oxygen	***Bond Length (Å)***		***BVS***
Nb1-O2-Nb2	1.957(6)	1.974(6)	1.79
Nb2-O3-Nb3	1.981(4)	1.981(4)	1.717
Nb3-O4-Nb4	1.938(6)	2.004(5)	1.79
Nb4-O5-Nb1	1.989(5)	1.990(6)	1.679
Nb5-O6-Nb1	1.902(4)	1.976(4)	1.932
Nb2-O7-Nb5	2.158(5)	2.142(5)	1.088*
Nb3-O8-Nb5	2.146(5)	2.138(4)	1.111*
Nb5-O9-Nb4	1.874(4)	2.054(4)	1.849
Nb6-O10-Nb1	2.119(5)	2.114(5)	1.19*
Nb2-O11-Nb6	1.923(4)	1.982(4)	1.859
Nb3-O12-Nb6	1.941(4)	1.931(4)	1.939
Nb6-O13-Nb4	1.949(5)	1.949(5)	1.873
Terminal Oxygen	***Bond Length (Å)***		***BVS***
Nb1-O14	1.771(6)		1.513
Nb2-O15	1.771(6)		1.513
Nb3-O16	1.774(5)		1.501
Nb4-O17	1.771(6)		1.516
Nb5-O18	1.786(5)		1.456
Nb6-O19	1.772(5)		1.510

This simple difference of diprotonation leading to dimers of **Ta6** vs triprotonation resulting in chains of **Nb6** may in fact have a significant effect on the film growth from these aqueous precursor solutions. While both solutions yield crystals through slow evaporation, rapid evaporation yields different results. A rotary evaporator was used to simulate the rapid evaporation of the solution upon spin-coating films. The Nb6 solution formed crystallites while **Ta6** formed a sticky gel (**figure 5.5**). This visual observation can be extended to hypothesize that **Ta6** forms a gelled

network upon film deposition, whereas **Nb6** crystallizes. We do observe that films deposited from **Ta6** retain a continuous appearance long after spin coating, while films deposited from **Nb6** must be immediately placed on the hot plate to prevent a breakdown of film continuity (**figure A.8**). We propose that the **Nb6** films on standing readily reorganize into a crystalline state. We note that multiple syntheses of the clusters lead to this very reproducible result of triprotonation of the hexaniobate and diprotonation of the hexatantalate, likely driven by combined effects of lattice energy and basicity of the clusters.

Figure 5.5. Rotary evaporated solutions of **Ta6** (left) and **Nb6** (right).

The AFM and XRR results, however, are somewhat inconsistent with this explanation. With an immediate hot- plate treatment, the **Nb6** films are found to be quite smooth at low temperatures. The greatest divergence in film roughness between Nb_2O_5 and Ta_2O_5 occurs at elevated annealing temperatures, where the original assembly of ions in the coating upon deposition should have lesser impact. At 800 °C, where Nb_2O_5 exhibits maximum roughness, the counterions have been completely eliminated, and the film has crystallized. At the same temperature, Ta_2O_5 films derived from **Ta6** remain very smooth. Either grains of Nb_2O_5 grow with a lower activation energy than those of Ta_2O_5, or H-bonding of **Nb6** into chains (**figure 5.6**) favors low-temperature nucleation, which translates to enhanced grain growth at higher temperatures. Additional studies are required to further evaluate the factors contributing to grain growth in these systems.

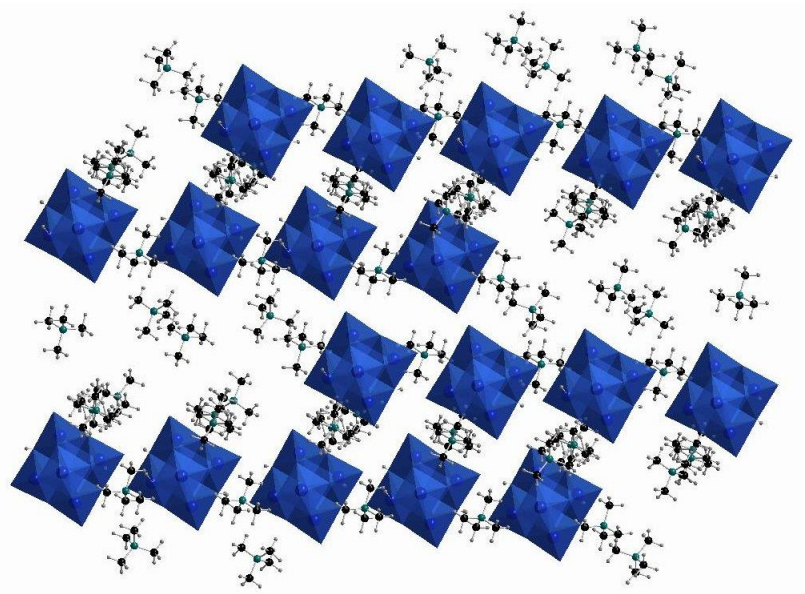

Figure 5.6. Representation of **Nb6** clusters linked by H-bonding, along with their TMA counterions.

Small and wide-angle X-ray scattering (SWAXS) was used to investigate aqueous solutions of **Nb6** and **Ta6**, and determine if the structural arrangements of ions observed in the solid state (that may be influencing film morphology) is translated from solution behavior. The simulated data for a single Lindqvist ion produced a modeled fit with a radius of 3.27 Å. This is smaller than the expected radius of 4.2 Å based on the solid-state structure. The size discrepancy is due to the apparent lack of contrast between the oxygens in the water (solvent is included in the simulation) and the oxygens on the outside of the cluster. However, in many other studies, the entire cluster including external ligands actually is "observed", and this could be due to a combination of effects, including the solvent/counterion molecules located in the first-coordination sphere of the cluster.[30]

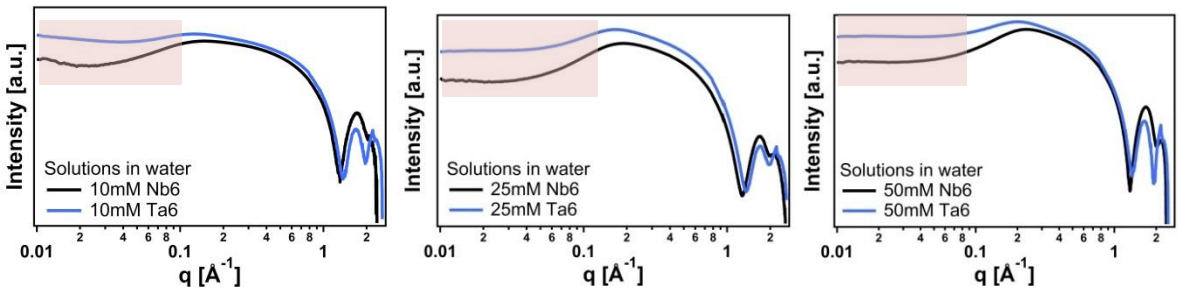

Figure 5.7. Scattering curves of **Ta6** (blue) and **Nb6** (black) in water. Pink box at low q indicates structure factor region.

Analysis of the scattering curves was performed through two modeling techniques which identify size distributions within a system: Size Distribution and Modeling II. The fit derived from Modeling II in Irena can also determine the extent of interactions between clusters. It was found that in water, **Nb6** has more extensive interaction between clusters in water than **Ta6** (**table 5.4**). This is evident in the larger structure factor in the scattering curves for the niobium system (**figure 5.7**). The structure factor consists of a decrease in intensity at low q which gives rise to a Coulombic peak around 0.1−0.2 Å−1. Particle−particle interactions can lead to short-range order where there is an increased probability to find a neighboring particle at a specific distance. For the niobium system in water we see consistently larger structure factors indicating that **Nb6** is more ordered in solution than **Ta6**. The structure factor is modeled by two parameters, describing the distance between clusters (smaller distance means more interaction) and the number of nearest neighbor clusters in solution (more neighbors means more interaction). The radii of scatterers were determined from modeled fits (**table 5.4**) which indicate that both clusters partially aggregate in water to form a second population of dimeric species, as we expect for protonated Lindqvist ions.

Table 5.4. Radii for simulated and experimental samples in water, along with interparticle interferences.

Water	*Pop. 1 Radius*	*Pop. 2 Radius*	*Distance to Nearest Neighbors (Å)**	*Number of Nearest Neighbors**
Simulated Lindqvist	3.27	--	--	--
10mM **Nb_6**	3.37	7.66	31.8	2.2
10mM **Ta_6**	3.27	8.61	42.9	1.2
25mM **Nb_6**	3.38	7.30	26.0	4.5
25mM **Ta_6**	3.32	8.14	32.7	1.9
50mM **Nb_6**	3.41	7.37	30.0	4.1
50mM **Ta_6**	3.33	8.18	25.1	2.9

**these values were averaged for the two populations of scatterers. Values determined using Modeling II in Irena.*[19]

These systems were also studied in dilute tetramethylammonium hydroxide (TMAOH) solutions. The cluster behavior is dependent on the solvent, as we see with a difference in scattering curves for solutions in water and solutions in TMAOH. Neat water provides an environment in which protonation of the clusters is predominant. TMAOH inhibits protonation as seen from the scattering curves (**figure 5.8**) and the resulting size distributions. At 10 and 25 mM both **Nb6** and **Ta6** exist as monomeric species with radii ~3.5 Å. This is consistent with deprotonated monomeric clusters. At higher concentrations, however, there is evidence of dimerization. Another difference between these systems in water versus TMAOH is a smaller structure factor. In the 10 mM solutions, there is almost no evidence of interparticle interactions. When a structure factor emerges at higher concentrations, the degree of interaction is the same for both **Ta6** and **Nb6**, as can be seen in **table 5.5**.

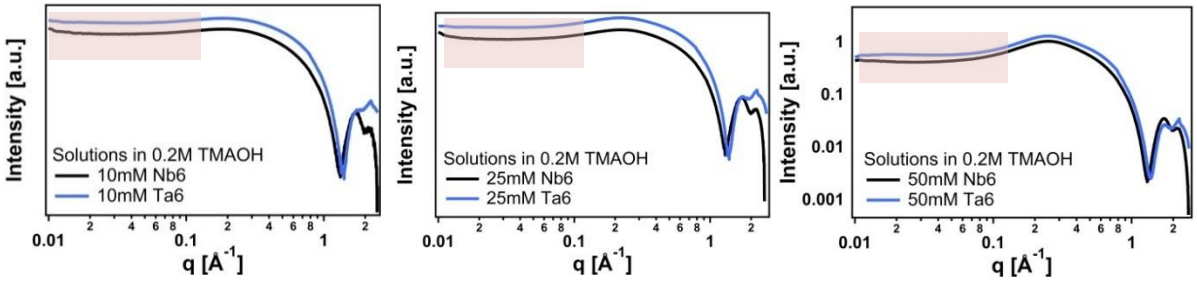

Figure 5.8. Scattering curves of **Ta6** (blue) and **Nb6** (black) in 0.2M TMAOH. Pink box indicates structure factor region.

Table 5.5. Radii and interparticle interactions of samples in 0.2M TMAOH solutions.

0.2M TMAOH	***Pop. 1 Radius***	***Pop. 2 Radius***	***Distance to Nearest Neighbors (Å)***	***Number of Nearest Neighbors***
Simulated Lindqvist	3.27	--	--	--
10mM **Nb_6**	3.67	--	22.2	0.4
10mM **Ta_6**	3.40	--	23.4	0.3
25mM **Nb_6**	3.63	--	21.3	0.7
25mM **Ta_6**	3.23	--	23.1	0.7
50mM **Nb_6**	3.43	6.61	20.4	1.4
50mM **Ta_6**	3.36	7.86	21.2	1.4

Values determined from Modeling II in Irena.[18]

Finally, scattering data were also collected for **Nb6** and **Ta6** in $TMANO_3$ solution, to provide an equivalent electrolyte as the TMAOH solution, but without inhibiting protonation. These data clearly show a structure factor in the **Nb6** solutions, and no structure factor in the **Ta6** solutions, with the exception of the highest concentration solution (**figure 5.9**).

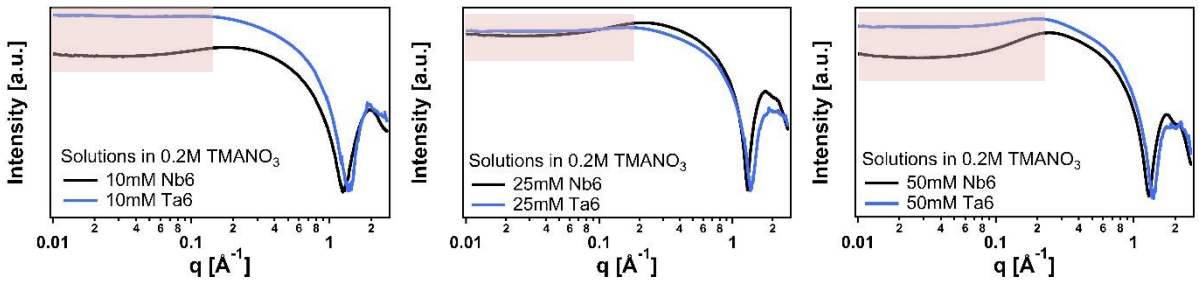

Figure 5.9. Scattering curves of **Ta6** (blue) and **Nb6** (black) in 0.2M $TMANO_3$. Pink box indicates structure factor region.

The difference in solution behavior between **Ta6** and **Nb6** could lead to the difference in film quality. As seen from rapid evaporation using the rotatory evaporator, **Ta6** gels while **Nb6** mostly crystallizes. This gel state is crucial to the formation of atomically smooth, high quality, dense films. The mechanism of forming the intermediate gel state is not yet known. The SWAXS results could lead to some insight on this matter. Clusters that aggregate into dimers without any further directional ordering could prevent crystallization, and instead the solution evaporates to give an amorphous gel containing cluster dimers, TMA, and water. The disordered aggregation exhibited in the **Ta6** solutions promotes formation of a gel, while **Nb6** crystallizes because of the ordering, promoted by chain formation. Finally, these X-ray scattering studies with varying solution electrolyte confirm that cluster−cluster association is driven by hydrogen-bonding of protonated faces.

5.5 CONCLUSIONS

Given the periodic table position of Nb and Ta, next to Zr and Hf that are virtually identical in structure and behavior due to the lanthanide contraction, we expect Nb and Ta to likewise be very similar. Indeed, in solid-state structures, coordination geometries are nearly indistinguishable,[26] but in solution, important differences have been recognized in prior studies and have also emerged in the current study. Previous DFT calculations and oxygen isotope exchange rates have led to the findings that hexatantalate has a smaller affinity toward protonation than hexaniobate, the terminal η=O is more labile than the bridging μ_2-O, and less energy is required to move a proton from μ_2-O to η=O.[13] These differences have merely been owed to the relativistic effect of the 4f electrons

of Ta, without a thorough understanding. The enthalpy of formation for Nb_2O_5 and Ta_2O_5 are, respectively, −1899 and −2046 kJ/mol:[31] perhaps reflecting the greater strength of a Ta−O bond, which may result in a weaker O−H bond, upon protonation. The pH values for solutions of identical concentrations of **Nb6** (10.36) and **Ta6** (9.95) indicate that **Ta6** is indeed less basic than its niobium analogue. Previous studies[13,30]have demonstrated that hexatantalate is also less stable in solution than hexaniobate. Upon decreasing the pH of a hexatantalate solution, the cluster will decompose to a hydrous tantalum oxide before it accommodates a third proton. This partial decomposition could also be a factor of gel formation: while disadvantageous for discrete cluster formation, it may be advantageous for formation of infinite solids of both powder and thin films. This study provides the first aqueous route to both Nb_2O_5 and Ta_2O_5 thin films. But also important, the fundamental science of this study illustrates the following: (1) the organization of ions in water correlates to similar order in a solid-state lattice, (2) H-bonding between metal-oxo clusters in water is very important in controlling precipitation behavior, and (3) acid−base behavior of metal-oxo species in water is very sensitive to the identity of the metal. While the latter point cannot always be neatly predicted by periodic trends of the transition metals, studies such as this can bring us closer to a more global understanding of relativistic and other effects on aqueous speciation of metal cations.

(1) Borras-Almenar, J. J.; Coronado, E.; Muller, A.; Pope, M. T. *Polyoxometalate Molecular Science*; Kluwer Academic Publishers, 2003.
(2) Mensinger, Z. L.; Wang, W.; Keszler, D. A.; Johnson, D. W. *Chem. Soc. Rev.* **2012**, *41*, 1019–1030.
(3) Chaneliere, C.; Autran, J. L.; Devine, R. A. B.; Balland, B. *Reports A Rev. J.* **1998**, *22*, 269–322.
(4) Ezhilvalavan, S.; Tseng, T.-Y. *J. Mater. Sci. Mater. Electron.* **1999**, *10*, 9–31.
(5) Lintanf-Salaün, A.; Mantoux, A.; Djurado, E.; Blanquet, E. *Microelectron. Eng.* **2010**, *87*, 373–378.
(6) Miao, F.; Strachan, J. P.; Yang, J. J.; Zhang, M.-X.; Goldfarb, I.; Torrezan, A. C.; Eschbach, P.; Kelley, R. D.; Medeiros-Ribeiro, G.; Williams, R. S. *Adv. Mater.* **2011**, *23*, 5633–5640.
(7) Epifani, M.; Zamani, R.; Arbiol, J.; Fabrega, C.; Andreu, T.; Pace, G. B.; Siciliano, P.; Morante, J. R. *Thin Solid Films* **2014**, *555*, 39–41.
(8) Lenzmann, F.; Shklover, V.; Brooks, K.; Atzel, M. G. R. *J. Sol-Gel Sci. Technol.* **2000**, *19*, 175–180.
(9) Lee, G. R.; Crayston, J. A. *J.Mater.Chem.* **1991**, *1*, 381–386.

(10) Velten, D.; Eisenbarth, E.; Schanne, N.; Breme, J. *J. Mater. Sci. Mater. Med.* **2004**, *15*, 457–461.
(11) Joshi, P. C.; Cole, M. W. *J. Appl. Phys.* **1999**, *86*, 871.
(12) Sone, Y.; Kishimoto, A.; Kudo, T.; Ikeda, K. *Solid State Ionics* **1996**, *83*, 135–143.
(13) Balogh, E.; Anderson, T. M.; Rustad, J. R.; Nyman, M.; Casey, W. H. *Inorg. Chem.* **2007**, *46*, 7032–7039.
(14) Hou, Y.; Fast, D. B.; Ruther, R. E.; Amador, J. M.; Fullmer, L. B.; Decker, S. R.; Zakharov, L. N.; Dolgos, M.; Nyman, M. *J. Solid State Chem.* **2014**, *Accepted*.
(15) Ohlin, C. A.; Villa, E. M.; Casey, W. H. *Inorganica Chim. Acta* **2009**, *362*, 1391–1392.
(16) Matsumoto, M.; Ozawa, Y.; Yagasaki, A.; Zhe, Y. *Inorg. Chem.* **2013**, *52*, 7825–7827.
(17) Matsumoto, M.; Ozawa, Y.; Yagasaki, A. *Inorg. Chem. Commun.* **2011**, *14*, 115–117.
(18) Matsumoto, M.; Ozawa, Y.; Yagasaki, A. *Inorg. Chem.* **2012**, *51*, 5991–5993.
(19) Ilavsky, J.; Jemian, P. R. *J. Appl. Crystallogr.* **2009**, *42*, 347–353.
(20) Zuo, X.; Goshe, A.; Zhang, R.; Tiede, D. M. *J. Appl. Crystallogr.*
(21) O'Boyle, N.; Banck, M.; James, C. A.; Morley, C.; Vandermeersch, T.; Hutchinson, G. R. *J. Cheminform.* **2011**, *3*.
(22) Sheldrick, G. M. *Bruker/Siemens Area Detector Absorption Correction Program*; Bruker AXS: Madison, WI, 1998.
(23) Van der Sluis, P.; Spek, A. L. *Acta Cryst. Sect. A* **1990**, *A46*, 197–201.
(24) SHELXTL-6.10. *Program for Structure Solution, Refinement and Presentation*; Bruker AXS Inc: Madison, WI.
(25) Selezneva, K. I.; Nisel'son, L. A. *Russ. J. Inorg. Chem.* **1968**, *13*, 45–47.
(26) Anderson, T. M.; Rodriguez, M. A.; Bonhomme, F.; Bixler, J. N.; Alam, T. M.; Nyman, M. *Dalt. Trans.* **2007**, *9226*, 4517–4522.
(27) Nyman, M.; Alam, T. M.; Bonhomme, F.; Rodriguez, M. a.; Frazer, C. S.; Welk, M. E. *J. Clust. Sci.* **2006**, *17*, 197–219.
(28) Masse, J. P.; Szymanowski, H.; Zabeida, O.; Amassian, A.; Klemberg-Sapieha, J. E.; Martinu, L. *Thin Solid Films* **2006**, *515*, 1674–1682.
(29) Yasaka, M. *Rigaku J.* **2010**, *26*, 1–9.
(30) Fullmer, L. B.; Molina, P. I.; Antonio, M. R.; Nyman, M. *Dalt. Trans.* **2014**, *43*, 15295–15299.
(31) www.materialsproject.org.

CHAPTER 6

REACTIONS OF HEXATANTALATE AND HEXANIOBATE WITH HYDROGEN PEROXIDE

Lauren B. Fullmer, Lindsay A. Wills, Chris Malmberg, Paul Cheong, May Nyman

To be submitted to *Dalton Transactions*

6.1 ABSTRACT

The terminal oxygens on hexaniobate and hexatantalate can be exchanged for peroxide, which affects the chemistry of these clusters. The peroxylation of hexatantalate is more kinetically favored than for hexaniobate, while peroxohexaniobate is less stable over time. The peroxide substitution reactions were monitored via small and wide angle x-ray scattering, Raman spectroscopy, and electrospray ionization mass spectrometry. Density functional theory was utilized to determine the energetics of peroxide addition, as well as preferred sites for substitution (cis vs. trans).

6.2 INTRODUCTION

Metal oxide clusters that include polyoxometalates and polyoxocations and their thin film derivatives [1–5] are currently being investigated for applications in catalysis, corrosion resistant coatings, electronic materials, and more.[6–11] Recently, metal-oxide clusters of hafnium/zirconium,[12–16] tin,[17] and niobium peroxophosphate[2] have been recognized to provide dimensional control for nanolithography. The Hf/Zr and niobium peroxophosphate aqueous chemistries developed for lithography exploit radiation sensitive peroxide which disproportionates to O_2 plus O^{2-} upon exposure to electrons or light.[15] The O^{2-} then forms intercluster bonds, rendering the exposed film insoluble. One disadvantage, however, of the Hf/Zr chemistry is the inability to introduce more than one peroxide ligand per two Hf/Zr^{IV} cations, providing poor sensitivity.[15] On the other hand, the niobium peroxophosphate clusters,[2] with one peroxide per niobium, demonstrate that rich peroxo-metalate chemistry can be achieved with group V polyoxometalates (POMs),containing Nb, or perhaps the chemically similar heavier congener, Ta.

Recently we reported deposition of M_2O_5 thin films from tetramethylammonium salts of the hexatantalate and hexaniobate Lindqvist ion $[H_xM_6O_{19}]^{(8-x)-}$ (M=Nb,Ta; see **figure 6.1**).[4,18] In these studies, we noted significant differences in film roughness, directly related to the protonated state of the clusters. The triprotonated state of the Nb-

analogue promoted crystallization by linking into chains through H-bonding of the clusters. The Ta-analogue, on the other hand, is diprotonated, so such chains leading to crystallization could not form, therefore dense and high quality films could be made. A dense, adherent, and smooth film is the first criteria to obtain small features from lithography.

Ohlin, et al showed via ^{17}O NMR, mass spectral studies and solid-state structure that replacement of the terminal oxygens in the Nb-Lindqvist ion is readily accomplished (**figure 6.1**). This cluster has one peroxide per metal, twice as many as the Hf/Zr-based chemistries on a per metal basis, and moreover, the peroxide ligands are positioned such that they may serve to link clusters together in the film deposition process.

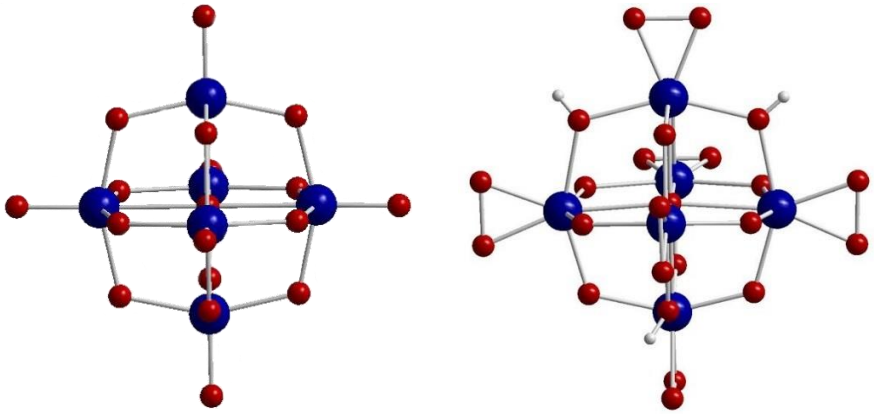

Figure 6.1. The Lindqvist structure (left) and the tri-protonated peroxohexaniobate (right). Blue atoms are the metals (Nb, Ta), red atoms are oxygen, and white atoms are protons.

Meanwhile, the analogous formation of $[H_xTa_6(O_2)_6O_{13}]^{(x-8)}$ has not been investigated. Here we document the formation of $[H_xTa_6(O_2)_6O_{13}]^{(x-8)}$ in solution, and expound on its solution phase behavior, especially in comparison to the established niobate analogue. $[H_xTa_6(O_2)_6O_{13}]^{(x-8)}$ is readily isolated as a solid by precipitation with isopropanol for further solid-state and solution characterization, yet it always is isolated at an amorphous material, and numerous crystallization attempts were not successful. While Raman spectroscopy, and electrospray ionization mass spectrometry (ESI-MS)

do not indicate any differences in peroxylation of hexatantalate and hexaniobate, X-ray scattering shows considerable difference in the arrangement of the ions in solution. The current working model of the X-ray scattering data is the hexatantalate clusters link via bridging of the bound peroxide, perhaps in random directions, which would explain the challenges of crystallizing these clusters. Raman spectra of solutions aged up to 8 months indicate the niobium analogue reverts back to the oxo-cluster, while the tantalate analogue is minimally changed. Computational studies were performed to elucidate both the stability of the oxo-clusters compared to the peroxo-clusters, and to compare the niobate and tantalate analogues. Density functional theory (DFT), was used to both examine the energetics of the step-wise replacement of oxo with peroxide on the hexametalate, and to identify the vibrational modes obtained in Raman spectroscopy.

6.3 General Methods and Materials

6.3.1 Synthesis

$[(CH_3)_4N]_6H_2Ta_6O_{19} \cdot 21H_2O$ (referred to as hexatantalate) and $[(CH_3)_4N]_5H_3Nb_6O_{19} \cdot 20H_2O$ (referred to as hexaniobate) were synthesized as previously reported.[17] A solution of 0.35 g of $[(CH_3)_4N]_6H_2Ta_6O_{19} \cdot 21H_2O$ (0.25 g of $[(CH_3)_4N]_5H_3Nb_6O_{19} \cdot 20H_2O$) in 5 mL of 18.2 MΩ deionized water was stirred in an ice water bath. Hydrogen peroxide (30% stock solution) was added in stoichiometric equivalents from one to six (ie: 16 µL H_2O_2 for monoperoxylated hexatantalate). The final product can be precipitated through addition of isopropanol. Thorough washing with isopropanol yields a hygroscopic, amorphous, white powder which can be dissolved in water or methanol for characterization.

For all characterization, samples were prepared in a series of one to six equivalents of peroxide for both hexatantalate and hexaniobate.

6.3.2 RAMAN

Raman spectroscopy was carried out on a Thermo Scientific DXR spectrometer with a 780 nm laser source, 400 lines/mm grating, and 50 μm slit. Eight exposures were collected at eight seconds each.

6.3.3 SWAXS

Small and wide angle x-ray scattering was collected on an Anton Paar SAXSess with Cu-Kα radiation (1.54 Å) and line collimation with a q range from 0.018-2.5 Å-. The instrument is equipped with a 2-dimensional image plate detector with a sample to image plate distance of 26.1 cm. Solutions were prepared in 1.5 mm borosilicate glass capillaries, and exposed to x-rays for 30 minutes. Solutions for background subtraction were prepared and measured in the same manner. SAXSquant software was used for data collection and initial processing. Igor Pro software utilizing the Irena macros was used for the data analysis to determine structure and form factors.[19]

6.3.4 ESI-MS

Electrospray ionization mass spectrometry (negative mode) was carried out using an Agilent 6230 TOF mass spectrometer with fragmentation voltage, cone voltage, and octapole voltages set to 100, 50 and 750 V respectively. Measurements were performed on 3mM solutions.

6.3.5 DENSITY FUNCTIONAL THEORY CALCULATIONS

All computations were performed in Gaussian 09. Geometry optimizations, Raman frequencies, and amplitudes were computed using B3LYP with the lal2dz basis set and effective core potential for Ta and 6-311++G(2df,p) basis set for all other atoms. CPCM solvation was used for all systems. Computed frequencies were scaled with a constant scaling factor using the experimental spectrum.

6.4 RESULTS AND DISCUSSION

Due to the amorphous nature of the peroxohexatantalate powders, a crystal structure has yet to be determined. We can initially assume that peroxide substitutes on the hexatantalate in the same fashion that we observe in the hexaniobate structure, with supporting evidence from ESI-MS and experimental and computed Raman spectra. While we expect the cluster species to be similar in the peroxide substitution, the arrangement of the clusters within a putative crystalline lattice and the protonation state of the solid form of peroxohexatantalate is not known.

Raman spectroscopy was used to monitor the reaction of peroxide with the hexametalate solution. According to previous work on the peroxohexaniobate, the peroxide exchange takes approximately 100 minutes to complete.[20] Time resolved ESI-MS was used in the aforementioned study, but Raman can be used qualitatively to observe changes in peak intensity and emergence of new peaks. Comparing the Raman spectra of the hexametalate solutions containing six equivalents of peroxide per cluster (**figures B.1 and B.3**), we observed semi quantitatively a faster rate of peroxylation for hexatantalate than for hexaniobate. The stretching mode of the terminal multiply bonded oxygen, M=O, is observed at 879 and 849 cm^{-1} for hexatantalate and hexaniobate respectively. As the peroxylation reaction occurs, this peak diminishes while the metal-bonded O-O peroxide peak at 846 and 865 cm^{-1} (hexatantalate and hexaniobate respectively) emerges and grows in intensity. We also observe both the symmetric and asymmetric metal-peroxide stretching vibrations, $M(O_2)$, in the 500-620 cm^{-1} range. These frequencies have been confirmed computationally (**figure B.2 and B.4**). The rate of peroxylation is likely directly related to the lability of the terminal oxygen site. Balogh et al. has shown that the terminal oxygen sites in hexatantalate have a faster oxygen-isotope exchange rate than those same sites in hexaniobate;[21] Therefore it follows that we can expect the same relative rates of exchange of the oxo-ligands for peroxide ligands for hexaniobate compared to hexatantalate.

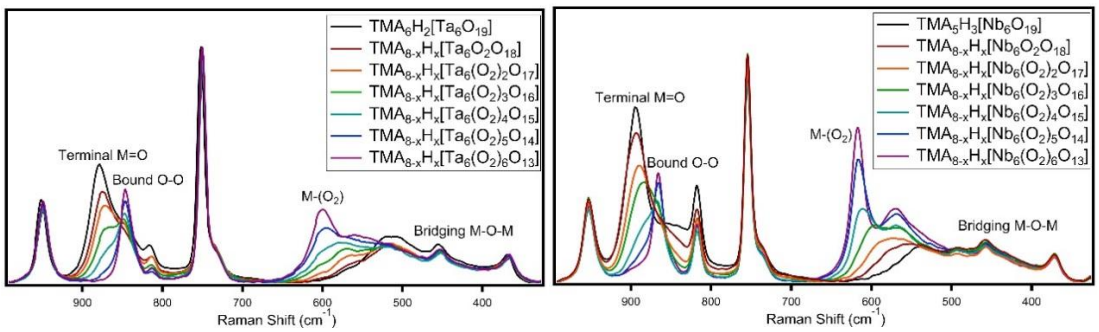

Figure 6.2. Raman spectra for the hexametalates and mono- to hexaperoxide substituted hexametalates. The peaks at ~950 and ~750 cm-1 are due to the TMA counterions.

In addition to solutions with six equivalents of peroxide per cluster, we prepared solutions with 1, 2, 3, 4 and 5 equivalents. Once the reactions were complete as indicated by Raman, the solutions were kept open overnight to allow any excess free peroxide to decompose. After one day, the Raman scattering of the series of both hexametalate/peroxide solutions were measured (**figure 6.2**). From these spectra, we see that with each equivalent of peroxide, there is a decrease in the M=O peak and an increase in the O-O and M(O_2) peaks, which is due to the exchange of one terminal oxygen for one peroxide with each additional equivalent. Since we observe the same trend for the peroxylation of hexaniobate, this provides strong evidence for the successful peroxylation of hexatantalate. All Raman peak assignments along with the calculated frequencies can be found in **tables 6.1 and B.1**.

Table 6.1. Theoretical and experimental Raman frequencies for peroxohexatantalate.

Mode	Observed Frequency [cm^{-1}]	Calculated Frequency [cm^{-1}]	Scaled Calc. Frequency [cm^{-1}]
M=O stretching	879, 815	866, 834	872, 840
O_2 vibration	846	912	844
M-O_2 stretching	599	594	550
M-O bending	452, 366	514, 404	475, 373

Small and wide angle x-ray scattering (SWAXS) was utilized to; 1) confirm the clusters persist in the presence of peroxide rather than convert to

tetraperoxomonomers,[22,23] $M(O_2)_4^{3-}$; and 2) determine the association between the clusters in the peroxylated form, and evaluate how it differs from the parent clusters.

Without a crystal structure of peroxohexatantalate, we based our x-ray scattering and Raman simulations on the niobium analogue. Comparing the crystal structures of hexaniobate and the hexa-peroxylated hexaniobate, the bonds between Nb and the central oxygen and Nb and the terminal oxygen are slightly longer while the Nb bonds to the bridging oxygen are shortened. These structural differences arise in an increased diameter of peroxohexaniobate.[24] However the resolution of SWAXS does not allow us to observe this small difference in size. Therefore, we cannot distinguish between the very similar-sized clusters in solution. We can, however, verify that the hexametalates are present in solution, with or without peroxide, and we observe cluster-cluster interactions in solution, discussed below.

X-ray scattering data for reaction solutions with 1-6 equivalents of peroxide per cluster are shown in **figure 6.3**, for both tantalate and niobate. For both the niobium and tantalum series, there are interactions between scattering species, identified by the structure factor located at q = 0.018-0.1 $Å^{-1}$. For the hexaniobate reaction solutions, there is minimal difference in the scattering curves for each subsequent peroxide addition. The solution with three peroxide equivalents exhibits higher background scattering at q = 1 – 2.5 $Å^{-1}$, the location of the solvent peak and the first oscillation, which is due to imperfect background subtraction for this particular sample. The modeled radius of the peroxohexaniobate species, agrees reasonably well with the expected radius of 3.25 Å (from simulated scattering curve) to 4.2 Å (crystal structure). The discrepancy in radii between the simulated scattering curve and the solid-state crystal structure is due to the lack of electron density contrast between the oxygens on the outside of the cluster and water (the solvent).

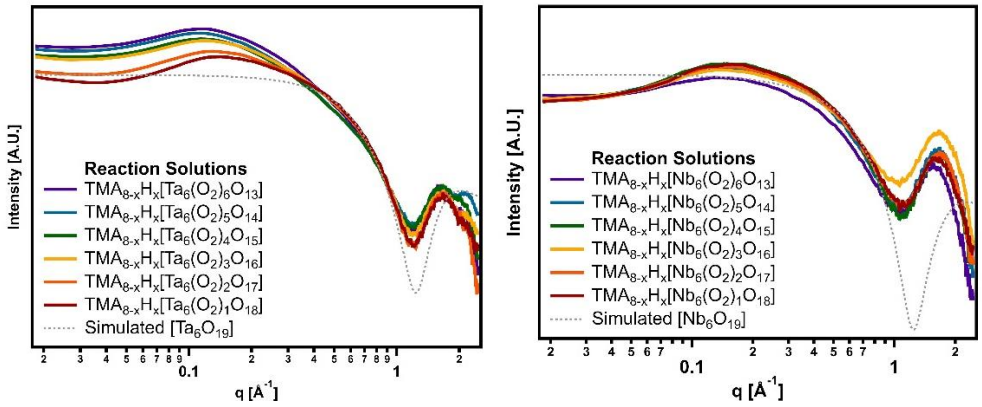

Figure 6.3. Scattering curves of the reaction solutions of hexatantalate (left) and hexaniobate (right). Data were intensity-normalized for easier comparison.

For the hexatantalate reaction solutions, there is a distinct trend within the series. Each scattering curve has two Guinier regions (q = 0.1-0.3 and 0.4-0.9 $Å^{-1}$) corresponding to the size of hexatantalate and a dimer of hexatantalates, as seen in previous studies.[18] From one equivalent of peroxide to six equivalents, the Guinier region of the dimers increases in intensity while the monomer region becomes less distinctive. The dimerization could be due to hydrogen bonding of protonated hexametalates or intercluster bridging by peroxide. Further evidence of increased protonation or aggregation, the peroxylated hexatantalate reaction solutions were very slightly cloudy due to the lower stability of hexatantalate with subsequent protonation.

There is also a decrease in the structure factor with subsequent peroxylation of hexatantalate, indicated by shallowing of low-q side of the coulombic peak at ~0.1 $Å^{-1}$. Further addition of peroxide induces either more protonation (see equations in **table 6.6** ahead) or more peroxide bridging. Both would lead to more extensive cluster linking. Linking of the clusters, regardless of the mechanism, decreases the charge density on each cluster, and therefore less repulsive interaction. This is how we explain the loss of the structure factor in the tantalate solutions.

Table 6.2. Fitting parameters for x-ray scattering data of peroxohexametalates including form (radii) and structure (cluster interactions) factors.

	Peroxylated Hexatantalate				Peroxylated Hexaniobate			
M_6O_{19}:H_2O_2 Ratio	Radius q=0.1-0.3 ($Å^{-1}$)	Radius q=0.4-0.9 ($Å^{-1}$)	Distance to Nearest Neighbors (Å)*	Number of Nearest Neighbors*	Pop One Radius	Radius q=0.3-0.7 ($Å^{-1}$)	Distance to Nearest Neighbors (Å)	Number of Nearest Neighbors
1:1	7.39	3.05	39.57	1.13	---	3.51	35.60	0.77
1:2	8.11	3.07	40.07	0.92	---	3.50	35.78	0.67
1:3	8.18	2.88	40.86	0.72	---	3.33	36.87	0.61
1:4	8.09	2.69	40.46	0.67	---	2.99	33.29	0.54
1:5	7.66	2.56	43.37	0.68	---	2.99	36.38	0.63
1:6	7.56	2.73	42.60	0.68	---	3.15	36.31	0.43
Simulated M_6O_{19}	---	3.27	---	---	---	3.25	---	---
Simulated Dimer	7.91	3.15	---	---	8.10	3.28	---	---

*These values were averaged for the two populations of scatterers.

Since the structure factor creates difficulties in modeling the data, we investigated other solution conditions. The peroxylated hexametalates were precipitated with isopropyl alcohol and dissolved in 1 M tetramethylammonium nitrate ($TMANO_3$) solution. It is known that electrolytes reduce electrostatic interactions between charged species in solution by shielding the charge, and therefore reduces the structure factor.[25] Electrolytes may also affect the protonation of the clusters, since they both affect hydration and provide an alternate means to neutralize local charge.

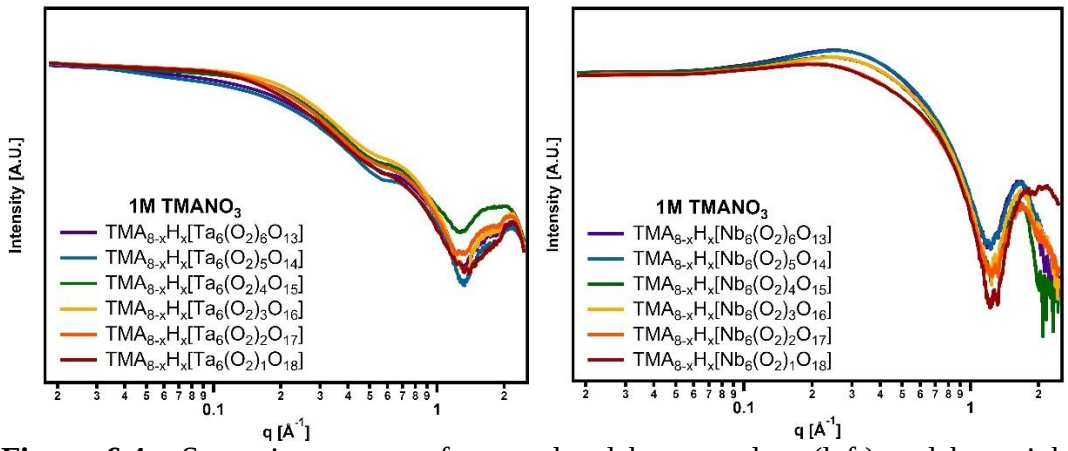

Figure 6.4. Scattering curves of peroxylated hexatantalate (left) and hexaniobate (right) dissolved in 1 M $TMANO_3$. Data were normalized to the same intensity for easier comparison.

The peroxylated hexatantalates, when dissolved in $TMANO_3$, show stronger evidence of linking (**figure 6.4**). Pair distance distribution function (PDDF) analysis of the scattering data indicates formation of aggregates upwards of 25 Å in size (**figure B.5**). Furthermore, in the scattering curves of penta- and hexaperoxohexatantalate, there is a slope in the scattering data below q = 0.3 $Å^{-1}$, which suggests aggregation. The structure factor is no longer apparent and we observe almost identical behavior from mono to hexaperoxohexatantalate that has been precipitated and dissolved in $TMANO_3$ solution.

Dissolving the peroxylated hexaniobates in $TMANO_3$ does not change the behavior of the clusters in solution. Monomeric clusters dominate as before, and the structure factor still exists. This observation is in agreement with the previous solution studies on hexaniobate.[18] There is also an increase in the structure factor with additional peroxide, which is opposite for what was observed in the peroxohexatantalate reaction solutions.

Table 6.3. Fitting parameters for x-ray scattering data of peroxohexametalate including form (radii) and structure (cluster interactions) factors.

	Peroxylated Hexatantalate				Peroxylated Hexaniobate			
M_6O_{19}:H_2O_2 Ratio	Radius *q*=0.1-0.3 ($Å^{-1}$)	Radius *q*=0.6-0.9 ($Å^{-1}$)	Distance to Nearest Neighbors (Å)	Number of Nearest Neighbors	Pop. One Radius	Radius *q*=0.3-0.8 ($Å^{-1}$)	Distance to Nearest Neighbors (Å)	Number of Nearest Neighbors
1:1	8.29	2.97	---	---	---	3.41	23.21	0.39
1:2	8.82	2.90	---	---	---	3.35	22.93	0.41
1:3	8.67	3.00	---	---	---	3.47	18.77	0.69
1:4	8.46	2.73	---	---	---	3.49	18.65	0.62
1:5	8.16	2.77	---	---	---	3.47	18.03	0.86
1:6	7.53	2.71	---	---	---	3.51	18.44	0.86
Simulated M_6O_{19}	---	3.27	---	---	---	3.25	---	---
Simulated Dimer	7.91	3.15	---	---	8.10	3.28	---	---

Electrospray ionization mass spectrometry was utilized to determine exact species in the reaction solutions and verify the trend observed by Raman spectra. With each additional equivalent of peroxide, the expected peroxylated cluster is observed as the dominant species. The dominant species for all peroxylated hexametalate solutions can be found in **tables 6.4 and 6.5**. A full list of identified peaks along with the spectra can be found in the supporting information. Even without a crystal structure, we have verified that peroxohexatantalate does indeed form with mono- to hexa-substitutions. A contradiction between the X-ray scattering data and ESI MS analysis could be perceived. That is, we observe only isolated clusters by mass spectrometry, whereas there is distinct evidence for cluster linkage in solution. Prior studies on Hf-speciation provide similar observations.[12,26] We interpret this similarly to the prior studies. That is, as mass increases and charge decreases of linked species, the m/z of these larger aggregates extend beyond the detection range of the instrument. Therefore, ESI MS is really most useful for identifying the primary cluster, or other smaller species.

Table 6.4. Most abundant species found by ESI-MS for peroxylated hexatantalate.

	Species	Experimental m/z	Calculated m/z	Relative Abundance (%)
Mono-peroxylated	$TMA_2H_5Ta_6O_{19}^{-1}$	1542.788	1542.825	100
	$TMA_2H_5Ta_6(O_2)O_{18}^{-1}$	1558.782	1558.819	56.89
	$TMA_3H_4Ta_6(O_2)O_{18}^{-1}$	1631.872	1631.909	75.71
Di-Peroxylated	$TMA_2H_4Ta_6(O_2)_2O_{17}^{-2}$	786.880	786.903	78.31
	$TMA_3H_4Ta_6(O_2)O_{18}^{-1}$	1631.870	1631.888	71.83
	$TMA_3H_4Ta_6(O_2)_2O_{17}^{-1}$	1647.865	1647.904	100
Tri-peroxylated	$TMA_2H_4Ta_6(O_2)_2O_{17}^{-2}$	786.880	786.903	97.30
	$TMA_2H_4Ta_6(O_2)_3O_{16}^{-2}$	794.877	794.901	80.61
	$TMA_3H_4Ta_6(O_2)_2O_{17}^{-1}$	1647.865	1647.904	100
	$TMA_3H_4Ta_6(O_2)_3O_{16}^{-1}$	1663.859	1663.898	75.37
Tetra-peroxylated	$TMAH_3Ta_6(O_2)_3O_{15}^{-2}$	749.328	749.351	62.78
	$TMA_2H_4Ta_6(O_2)_3O_{16}^{-2}$	794.877	794.901	100
	$TMA_2H_4Ta_6(O_2)_4O_{15}^{-2}$	802.874	802.898	61.31
	$TMA_3H_4Ta_6(O_2)_3O_{16}^{-1}$	1663.860	1663.898	79.39
Penta-Peroxylated	$TMAH_3Ta_6(O_2)_5\ O_{13}^{-2}$	765.323	765.346	61.41
	$TMA_2H_2Ta_6(O_2)_6O_{12}^{-2}$	809.863	809.888	69.45
	$TMA_2H_4Ta_6(O_2)_5O_{14}^{-2}$	810.871	810.896	100
	$TMA_2H_4Ta_6(O_2)_6O_{13}^{-2}$	818.869	818.893	88.69
Hexa-peroxylated	$TMA_2H_2Ta_6(O_2)_6O_{12}^{-2}$	809.865	809.888	70.95
	$TMA_2H_4Ta_6(O_2)_6O_{13}^{-2}$	818.870	818.893	100

Table 6.5. Most abundant species found by ESI-MS for peroxylated hexaniobate.

	Species	Experimental m/z	Calculated m/z	Relative Abundance (%)
Mono-peroxylated	$TMAHNb_6(O_2)O_{16}^{-2}$	460.212	460.226	100
	$TMA_2HNb_6(O_2)O_{16}^{-1} \cdot 2H_2O$	1030.535	1030.570	69.63
Di-Peroxylated	$TMAHNb_6(O_2)_2O_{15}^{-2}$	468.210	468.223	84.04
	$TMA_2H_3Nb_6(O_2)_2O_{16}^{-1} \cdot H_2O$	1046.537	1046.565	100
	$TMA_2HNb_6(O_2)_3O_{14}^{-1} \cdot 2H_2O$	1062.533	1062.559	81.32
Tri-peroxylated	$TMAHNb_6(O_2)_2O_{15}^{-2}$	468.210	468.223	62.50
	$TMAHNb_6(O_2)_3O_{14}^{-2}$	476.206	476.221	100
	$TMA_2HNb_6(O_2)_3O_{14}^{-1} \cdot 2H_2O$	1062.533	1062.559	97.21
Tetra-peroxylated	$TMAHNb_6(O_2)_3O_{14}^{-2}$	476.206	476.221	100
	$TMAHNb_6(O_2)_4O_{13}^{-2}$	484.203	484.218	82.39
	$TMA_2Nb_6(O_2)_4O_{13}^{-2}$	520.747	520.763	71.09
	$TMA_2HNb_6(O_2)_4O_{13}^{-1} \cdot 2H_2O$	1078.527	1078.554	73.68
Penta-Peroxylated	$TMAHNb_6(O_2)_3O_{14}^{-2}$	476.206	476.221	80.09
	$TMAHNb_6(O_2)_4O_{13}^{-2}$	484.203	484.218	100

	$TMA_2Nb_6(O_2)_5O_{12}^{-2}$	528.744	528.763	65.25
	$TMA_2Nb_6(O_2)_6O_{11}^{-2}$	536.741	536.758	74.53
	$TMA_2H_2Nb_6(O_2)_6O_{12}^{-2}$	545.746	545.763	66.51
Hexa-peroxylated	$TMAHNb_6(O_2)_4O_{13}^{-2}$	484.204	484.218	81.34
	$TMA_2Nb_6(O_2)_6O_{11}^{-2}$	536.742	536.758	70.68
	$TMA_2HNb_6(O_2)_6O_{11}^{-1} \cdot 2H_2O$	1110.517	1110.544	100

The stabilities of peroxohexatantalate and peroxohexaniobate were monitored by Raman over eight months. The fully peroxylated hexametalates were dissolved in water and left in a loosely closed vial on the benchtop (to allow pressure release from evolved O_2 gas). According to the Raman, peroxohexatantalate is more stable than its niobium analogue. There is a slight decrease in intensity of the peroxide associated peaks, as well as an emerging shoulder corresponding to the terminal -yl oxygen. While this indicates some loss of bound peroxide, the peak corresponding with peroxylation is still dominant. Therefore, most of the peroxide remains bound to the hexatantalate. On the other hand, peroxohexaniobate slowly evolves back to the parent Lindqvist ion. By five months, the metal-bound O_2 peaks at 865 cm^{-1} and 617 cm^{-1} are reduced to shoulders. By eight months the spectrum is almost identical to the original hexaniobate, prior to peroxylation. (**figures B.6 and B.7**) The apparent instability of the peroxylated hexaniobate compared to hexatantalate, taken together with the SWAXS data in $TMANO_3$ solution might suggest the Ta-bound peroxide tends to link clusters together via bridging, while Nb-bound peroxide simply caps clusters. This bridging of clusters stabilizes both the peroxide links, as well as the aggregates formed by the bridging behavior. This would also explain the difficulty in crystallizing the peroxylated hexatantalate, even though the niobate analogue is readily crystallized, and peroxide replacement of the terminal -yl oxygens on hexatantalate clearly occurs, as evidenced by ESI MS and Raman spectroscopy.

DFT computations were used to determine the energetics associated with each addition of peroxide to the hexametalate clusters. The computed thermodynamics showed that the peroxylation of hexatantalate and hexaniobate are energetically favored. While there is some variation, on average, the free energy associated with each

addition of peroxide is circa –12 kcal/mol. Peroxides favored *cis*-additions to both the hexatantalate and hexaniobate clusters, creating a *fac*-like arrangement after adding three peroxides to the structure (**figure 6.5**). A majority of the lowest energy configurations were ones in which the peroxides preferred to adopt perpendicular orientations to each other as seen in **figure 6.5**. The free energies of each stepwise addition, as well as the free energies to form each cluster from the hexatantalate are shown below in **table 6.6**.

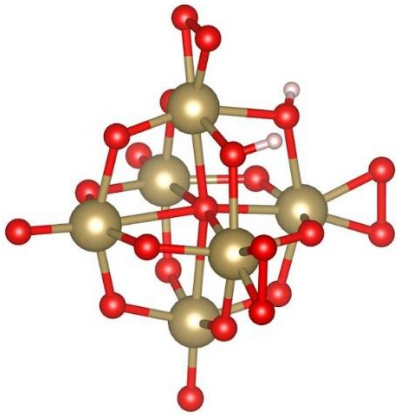

Figure 6.5. Hexametalate with peroxide addition in *fac*-like arrangement. Peroxides prefer to arrange perpendicularly to each other.

Table 6.6. Energetics of peroxylation of hexatantalate. Stepwise addition of peroxide as well as full peroxylation in a single step are included, with and without the protons included in the structure.

Reaction	**ΔH, kcal/mol (x = 0)**	**ΔH, kcal/mol (x = 2)**
$H_2O_2 + H_xTa_6O_{19}^{(8-x)-} \rightarrow H_2O + H_xTa_6(O_2)O_{18}^{(8-x)-}$	-12.8	-12.9
$H_2O_2 + H_xTa_6(O_2)O_{18}^{(8-x)-} \rightarrow H_2O + H_xTa_6(O_2)_2O_{17}^{(8-x)-}$	-13.4	-14.2
$H_2O_2 + H_xTa_6(O_2)_2O_{17}^{(8-x)-} \rightarrow H_2O + H_xTa_6(O_2)_3O_{16}^{(8-x)-}$	-11.5	-13.6
$H_2O_2 + H_xTa_6(O_2)_3O_{16}^{(8-x)-} \rightarrow H_2O + H_xTa_6(O_2)_4O_{15}^{(8-x)-}$	-15.1	-11.7
$H_2O_2 + H_xTa_6(O_2)_4O_{15}^{(8-x)-} \rightarrow H_2O + H_xTa_6(O_2)_5O_{14}^{(8-x)-}$	-13.3	-10.8
$H_2O_2 + H_xTa_6(O_2)_5O_{14}^{(8-x)-} \rightarrow H_2O + H_xTa_6(O_2)_6O_{13}^{(8-x)-}$	-14.4	-12.7

$H_2O_2 + H_xTa_6O_{19}^{(8-x)-} \rightarrow H_2O + H_xTa_6(O_2)O_{18}^{(8-x)-}$	-12.8	-12.9
$2H_2O_2 + H_xTa_6O_{19}^{(8-x)-} \rightarrow 2H_2O + H_xTa_6(O_2)_2O_{17}^{(8-x)-}$	-26.2	-27.1
$3H_2O_2 + H_xTa_6O_{19}^{(8-x)-} \rightarrow 3H_2O + H_xTa_6(O_2)_3O_{16}^{(8-x)-}$	-47.6	-40.8
$4H_2O_2 + H_xTa_6O_{19}^{(8-x)-} \rightarrow 4H_2O + H_xTa_6(O_2)_4O_{15}^{(8-x)-}$	-52.7	-52.5
$5H_2O_2 + H_xTa_6O_{19}^{(8-x)-} \rightarrow 5H_2O + H_xTa_6(O_2)_5O_{14}^{(8-x)-}$	-66.0	-63.3
$6H_2O_2 + H_xTa_6O_{19}^{(8-x)-} \rightarrow 6H_2O + H_xTa_6(O_2)_6O_{13}^{(8-x)-}$	-80.4	-76.0

Table 6.7. Energetics of peroxylation of hexaniobate. Stepwise addition of peroxide as well as full peroxylation in a single step are included, with and without the protons included in the structure.

Reaction	**ΔH, kcal/mol (x = 0)**	**ΔH, kcal/mol (x = 2)**
$H_2O_2 + H_xNb_6O_{19}^{(8-x)-} \rightarrow H_2O + H_xNb_6(O_2)O_{18}^{(8-x)-}$	-14.4	-15.2
$H_2O_2 + H_xNb_6(O_2)O_{18}^{(8-x)-} \rightarrow H_2O + H_xNb_6(O_2)_2O_{17}^{(8-x)-}$	-15.1	-13.6
$H_2O_2 + H_xNb_6(O_2)_2O_{17}^{(8-x)-} \rightarrow H_2O + H_xNb_6(O_2)_3O_{16}^{(8-x)-}$	-12.1	-13.9
$H_2O_2 + H_xNb_6(O_2)_3O_{16}^{(8-x)-} \rightarrow H_2O + H_xNb_6(O_2)_4O_{15}^{(8-x)-}$	-17.0	-13.2
$H_2O_2 + H_xNb_6(O_2)_4O_{15}^{(8-x)-} \rightarrow H_2O + H_xNb_6(O_2)_5O_{14}^{(8-x)-}$	-14.2	-10.9
$H_2O_2 + H_xNb_6(O_2)_5O_{14}^{(8-x)-} \rightarrow H_2O + H_xNb_6(O_2)_6O_{13}^{(8-x)-}$	-9.4	-12.2
$H_2O_2 + H_xNb_6O_{19}^{(8-x)-} \rightarrow H_2O + H_xNb_6(O_2)O_{18}^{(8-x)-}$	-14.4	-15.2
$2H_2O_2 + H_xNb_6O_{19}^{(8-x)-} \rightarrow 2H_2O + H_xNb_6(O_2)_2O_{17}^{(8-x)-}$	-29.5	-28.8
$3H_2O_2 + H_xNb_6O_{19}^{(8-x)-} \rightarrow 3H_2O + H_xNb_6(O_2)_3O_{16}^{(8-x)-}$	-41.6	-42.7
$4H_2O_2 + H_xNb_6O_{19}^{(8-x)-} \rightarrow 4H_2O + H_xNb_6(O_2)_4O_{15}^{(8-x)-}$	-58.6	-55.9
$5H_2O_2 + H_xNb_6O_{19}^{(8-x)-} \rightarrow 5H_2O + H_xNb_6(O_2)_5O_{14}^{(8-x)-}$	-72.8	-66.7
$6H_2O_2 + H_xNb_6O_{19}^{(8-x)-} \rightarrow 6H_2O + H_xNb_6(O_2)_6O_{13}^{(8-x)-}$	-82.2	-78.9

6.5 CONCLUSIONS

Peroxylation of the hexametalates affects the chemistry of the clusters. Exchanging peroxide for the terminal multiply bonded -yl oxygen causes a lengthening of the central and terminal oxygen bonds, while the bridging oxygen bonds are shortened. This increases the diameter of the cluster, making peroxohexaniobate slightly larger

than the non-peroxylated hexaniobate.[24] We expect the same structural changes for the peroxohexatantalate, even though there is no crystal structure to verify. There are also more surface atoms in the peroxohexametalates, which lowers the surface charge density of the cluster. This lowers the basicity of the bridging oxygens, decreasing the affinity for protons. Due to this change in basicity, the peroxohexametalates are stable in a wider pH range (6<pH<12).[2]

While we have yet to obtain crystals for a structural analysis, we have confirmed the existence of mono- to hexa-peroxotantalate via ESI-MS, SWAXS, and Raman. We note that the substitution of peroxide is a faster reaction for hexatantalate than for hexaniobate. Peroxohexatantalate also shows greater stability than its niobium analogue.

Thin film work is underway to determine if the peroxylated hexametalates are comparable precursors to the non-peroxylated systems. Thin films made from TMA hexatantalate are atomically smooth and are promising candidates for device fabrication.[4,18] Preliminary results indicate even film morphology for both peroxylated hexametalates, as well as radiation sensitivity for lithography applications.

6.6 ACKNOWLEDGEMENTS

This work was supported by the National Science Foundation CCI grant through the Center for Sustainable Material Chemistry (CHE-1102637).

(1) Llordés, A.; Wang, Y.; Fernandez-Martinez, A.; Xiao, P.; Lee, T.; Poulain, A.; Zandi, O.; Saez Cabezas, C. A.; Henkelman, G.; Milliron, D. J. *Nat. Mater.* **2016**, *1* (August 2016).

(2) Son, J.-H.; Park, D.-H.; Keszler, D. A.; Casey, W. H. *Chem. - A Eur. J.* **2015**, *95616*, n/a-n/a.

(3) Hou, Y.; Fast, D. B.; Ruther, R. E.; Amador, J. M.; Fullmer, L. B.; Decker, S. R.; Zakharov, L. N.; Dolgos, M. R.; Nyman, M. *J. Solid State Chem.* **2015**, *221*, 418–425.

(4) Mansergh, R. H.; Fullmer, L. B.; Park, D.-H.; Nyman, M.; Keszler, D. A. *Chem. Mater.* **2016**, acs.chemmater.6b00078.

(5) Busche, C.; Vilà-Nadal, L.; Yan, J.; Miras, H. N.; Long, D.-L.; Georgiev, V. P.; Asenov, A.; Pedersen, R. H.; Gadegaard, N.; Mirza, M. M.; Paul, D. J.; Poblet, J. M.; Cronin, L. *Nature* **2014**, 1–5.

(6) Coronado, E.; Gómez-García, C. J. *Chem. Rev.* **1998**, *98* (1), 273–296.
(7) Katsoulis, D. E. *Chem. Rev.* **1998**, *98* (1), 359–388.
(8) Yamase, T. *Chem. Rev.* **1998**, *98* (1), 307–326.
(9) Miras, H. N.; Yan, J.; Long, D.-L.; Cronin, L. *Chem. Soc. Rev.* **2012**, *41* (22), 7403–7430.
(10) Long, D.-L.; Burkholder, E.; Cronin, L. *Chem. Soc. Rev.* **2007**, *36* (1), 105–121.
(11) Goberna-Ferrón, S.; Park, D.-H.; Amador, J. M.; Keszler, D. A.; Nyman, M. *Angew. Chemie Int. Ed.* **2016**, 1–5.
(12) Li, L.; Chakrabarty, S.; Spyrou, K.; Ober, C. K.; Giannelis, E. P. *Chem. Mater.* **2015**, 150701105733005.
(13) Amador, J. M.; Decker, S. R.; Lucchini, S. E.; Ruther, R. E.; Keszler, D. A. *Proc. SPIE* **2014**, *9051* (scheme 1), 90511A–90511A–6.
(14) Oleksak, R. P.; Ruther, R. E.; Luo, F.; Fairley, K. C.; Decker, S. R.; Stickle, W. F.; Johnson, D. W.; Garfunkel, E. L.; Herman, G. S.; Keszler, D. A. *Appl. Mater. Interfaces* **2014**, *6*, 2917–2921.
(15) Anderson, J. T.; Munsee, C. L.; Hung, C. M.; Phung, T. M.; Herman, G. S.; Johnson, D. C.; Wager, J. F.; Keszler, D. A. *Adv. Funct. Mater.* **2007**, *17* (13), 2117–2124.
(16) Cardineau, B.; Del Re, R.; Marnell, M.; Al-Mashat, H.; Vockenhuber, M.; Ekinci, Y.; Sarma, C.; Freedman, D. A.; Brainard, R. L. *Microelectron. Eng.* **2014**, *127*, 44–50.
(17) Fullmer, L. B.; Mansergh, R. H.; Zakharov, L. N.; Keszler, D. A.; Nyman, M. *Cryst. Growth Des.* **2015**, *15* (8), 3885–3892.
(18) Ilavsky, J.; Jemian, P. R. *J. Appl. Crystallogr.* **2009**, *42* (2), 347–353.
(19) Ohlin, C. A.; Villa, E. M.; Fettinger, J. C.; Casey, W. H. *Angew. Chemie* **2008**, *47* (43), 8251–8254.
(20) Balogh, E.; Anderson, T. M.; Rustad, J. R.; Nyman, M.; Casey, W. H. *Inorg. Chem.* **2007**, *46* (17), 7032–7039.
(21) Selezneva, K. I.; Nisel'son, L. A. *Russ. J. Inorg. Chem.* **1968**, *13* (1), 45–47.
(22) Bayot, D.; Devillers, M. *Coord. Chem. Rev.* **2006**, *250* (19–20), 2610–2626.
(23) Si, Y.-L.; Wang, E.-B. *Mol. Phys.* **2009**, *107* (15), 1521–1526.

CHAPTER 7

PROBING CRYSTALLIZATION PATHWAYS IN GROUP V POLYOXOMETALATE SOLUTIONS

Lauren B. Fullmer, May Nyman

Journal of Cluster Science, **2016**

7.1 ABSTRACT

Structure elucidation is extremely important to understand and control processes in synthetic chemistry, in drug design, and in biomolecular function; and the most important step of structure elucidation is crystallization. Preceding crystallization of ionic compounds is usually ion-association in solution, which can be induced by a variety of ways. Here we study ion-association of hexaniobate and hexatantalate polyoxometalate salts in mixed water-alcohol solutions. These hexametalate clusters have the unusual characteristic of increased solubility with increased ion-association, which makes them ideal candidates to understand the fundamentals of ion-pairing. We utilize direct (X-ray scattering) and indirect (ion-conductivity) methods to document the ion-association as a function of alkali, concentration, alcohol:water ratio, and Nb vs. Ta. The conductivity data coupled with x-ray scattering shows that decreasing solvent polarity increases cluster-alkali association; but decreases any interaction between the alkali-cluster aggregates. Conductivity data show the trend of increasing alkali-cluster association with increasing alkali size as is expected for hexaniobate, but has some discrepancies with hexatantalate. We attribute this to the concomitant effects of protonation of the clusters, with hexaniobate being a stronger base. These studies provide insight into aqueous behaviour of these clusters that exhibit the anomalous behaviour of high solubility with maximum ion-association.

7.2 INTRODUCTION

Polyoxometalates (POMs) are water soluble metal-oxo clusters composed primarily of group V/VI transition metals. POMs have diverse cluster geometries and chemical behaviour in both solution and solid state.[1] Group V POMs of niobium and tantalum are different from other POMs due to their alkaline nature, high charge density, and anomalous solubility trends.[2] The speciation of niobium and tantalum in alkaline pH is dominated by the Lindqvist ion; a superoctahedron composed of six mutually edge sharing MO_6 octahedra.[3] Because they have increased solubility with increased ion-pairing as well as stable speciation in base, group V POMs have been the

focus of recent ion-association studies.[4–7] Ion association is fundamentally important for aqueous systems, whether it be counter cations pairing with an anionic cluster or assembly of macromolecules[8,9]. Ion association can be characterized by direct observation of the paired ions, i.e. by small angle x-ray scattering[4]; or indirectly such as by conductivity/ionic mobility measurements[7,10].

As a first estimation to describe dissolution of inorganic salts, the solid-state lattice homogeneously dissociates into free ions as described by the Debye-Hückel theory. However, there is some degree of ion association even in dilute solutions.[4,5,10] There are three related ion association motifs; contact/direct, solvent-shared, and solvent-separated ion pairing. Counter cations can associate directly to the faces of a Lindqvist polyoxometalate anion which is referred to as contact or direct ion pairing. The Lindqvist ion, $[M_6O_{19}]$ with an 8- charge for M = Nb and Ta, can associate with 8 cations rendering the species essentially neutral. Solvent-shared ion pairing exists when the counter cation and POM are associated with one another via a shared hydration sphere of water molecules. When each ion has its own hydration sphere, this is referred to as solvent-separated ion association.[4]

Ion association between any anion and alkali cations should follow a distinct trend with the alkali metal size, inversely related to the size of the alkali hydration sphere. The degree of ion association increases with increasing size of the alkali (Cs =Rb > K > Na = Li). This is also the trend in solubility for the group V POMs which opposes that of classical POMs such as polytungstates and polymolybdates,[4] as well as other anionic metal-oxo clusters including the uranyl peroxide capsules.[11] The solid state structures of the alkali hexametalates provide a model for counter-cation association with the cluster during crystallization. Larger alkali metals such as Cs and Rb are more closely associated with the cluster with an average number of alkali-oxygen bonds per alkali of 3.75. The lighter alkalis such as K have only 2.38 alkali-oxygen bonds per alkali.[1] From this solid state data, we can interpret that the larger alkalis are more closely associated with the hexametalate, and is also likely the case in solution. The ion association of tetramethylammonium (TMA), $(CH_3)_4N^+$, cations has yet to be discussed

in the literature. However, this relatively small organic is less charge dense than the alkalis and it is suspected that it will undergo very weak ion association if at all. Further support for this weaker ion association is provided by the solid state structure where the TMA cations are located farther from the cluster than in alkali structures (TMA-O average distance is 4.3 Å, whereas K-O average distance is 3.0 Å).[1] Notably, all TMA cluster salts have high aqueous solubility, consistent with minimal ion-association with the anionic cluster.

Association and dissociation of ions in solutions as a function of solvent polarity has been observed by SAXS and NMR studies on the protonation of decavanadates.[12] This work demonstrated that these associations are solvent driven. Moreover, the association of decavanadate ions observed in solution, dimerized via mutual H-bonding of protonated faces, is identical to that observed in a crystalline lattice of decavanadate. [13] All studies thus far of ion-association of the hexametalates has ensued in water. Yet we can crystallize them by introduction of alcohol,[1,14] and there has been noted a correlation between crystallization of protonated clusters and presence of alcohol in the crystallization medium. Here we probe the structuring and ion-association of Lindqvist ions plus their alkali counterions in water-methanol mixtures by direct (SWAXS) and indirect (conductivity) methods.

7.3 MATERIALS AND METHODS

7.3.1 SYNTHESIS

The alkali hexaniobate salts $K_8[Nb_6O_{19}]\cdot 16H_2O$, $Rb_8[Nb_6O_{19}]\cdot 14H_2O$, and $Cs_8[Nb_6O_{19}]\cdot 16H_2O$, and alkali hexatantalate salts $K_8[Ta_6O_{19}]\cdot 14H_2O$, $Rb_8[Ta_6O_{19}]\cdot 14H_2O$, and $Cs_8[Ta_6O_{19}]\cdot 14H_2O$ were synthesized as previously described.[1,15] The syntheses of the TMA salts $TMA_6H_2[Ta_6O_{19}]\cdot 21H_2O$ and $TMA_5H_3[Nb_6O_{19}]\cdot 20H_2O$ are also described elsewhere.[14] Solutions of each were prepared at 15 mM and 50 mM for conductivity and SWAXS studies. Solutions for x-ray scattering were prepared as outlined in **table C.1**.

7.3.2 SMALL AND WIDE ANGLE X-RAY SCATTERING

Scattering data were collected on an Anton Paar SAXSess instrument utilizing Cu-Kα radiation and line collimation. Solutions outlined in **table C.1** were sealed in a 1.5 mm diameter borosilicate capillary and measured under vacuum for 1 hour. Data were processed using SAXSquant software for normalization, background subtraction, desmearing, and smoothing. Analysis of the processed data was carried out using Igor Pro with the Irena macros.[16]

7.3.3 CONDUCTIVITY

Conductivity measurements were carried out using a Thermo Scientific Orion Versastar advanced electrochemistry meter equipped with an Orion 013005MD conductivity cell. The conductivity cell is an epoxy/graphite probe with a nominal cell constant of 0.475 cm^{-1}. Three samples of each solution were prepared for conductivity measurements in order to account for errors. Theoretical conductivities for each solution were calculated by first determining the ion mobility in free solution using:

$$\mu_0 = \frac{q}{6\pi\eta R} \quad (1)$$

where μ_0, η, q, and R are the ion mobility in free solution, solvent viscosity, ion charge, and ion radius respectively. The conductivity can then be calculated using:

$$K = F\sum(q\mu_0 C) \quad (2)$$

Where K, F, and C are conductivity, Faraday's constant, and concentration respectively. Molar conductivity can then be calculated by dividing the conductivity by the molarity.[10].

7.4 RESULTS

Ion mobility, and therefore the conductivity, is most affected by the ion's charge and radius. $TMA_6[H_2Ta_6O_{19}]$, for example, is diprotonated which decreases the charge on the cluster from 8^- to 6^-. This decrease in charge decreases the cluster's calculated mobility in solution from $1.8x10^{-3}$ $cm^2/(V*s)$ to $1.4x10^{-3}$ $cm^2/(V*s)$. Protonated clusters have a tendency to dimerize, in which case the overall charge would be increased, as well as the radius of the unit of dimers. The mobility for the deprotonated hexatantalate ion is $1.8x10^{-3}$ $cm^2/(V*s)$, while a dimer of diprotonated hexatantalates has a calculated

mobility of $1.6x10^{-3}$ $cm^2/(V*s)$. The resulting conductivity would be lower still since the number of ions in solution has decreased by half.

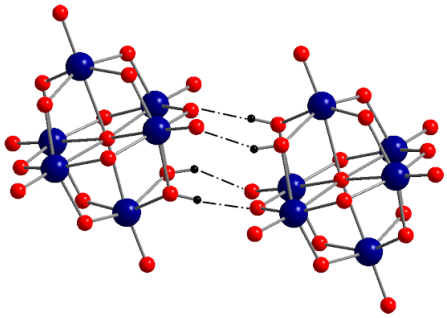

Figure 7.1. Protonated Lindqvist ions associating through hydrogen bonding. Blue spheres are Nb/Ta, red spheres are O, and black spheres are the protons.

Conductivity measurements on a series of $A_8[M_6O_{19}]$ (A = K, Rb, Cs, TMA; M = Nb, Ta) in solution of mixed methanol and water were performed to determine the effect of concentration of the POM salt and the polarity of the solution, controlled by the methanol/water ratio. More concentrated solutions exhibited lower molar conductivity than the less concentrated solutions. When methanol is added to the systems, the molar conductivity likewise decreases (**figure 7.2**).

Experimental molar conductivity was compared with calculated values using equations (1) and (2). Plots of the conductivity of 15 and 50 mM POM salts in methanol/water solutions are shown in **figure 7.2**. Tabulated values for experimental and calculated conductivities for all samples may be found in Appendix C (**tables C.5** through **C.13**)

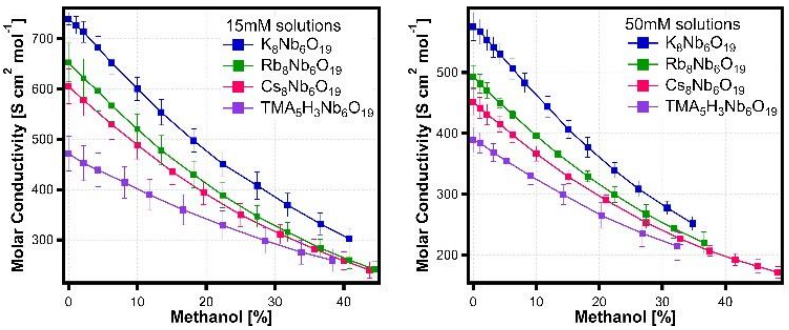

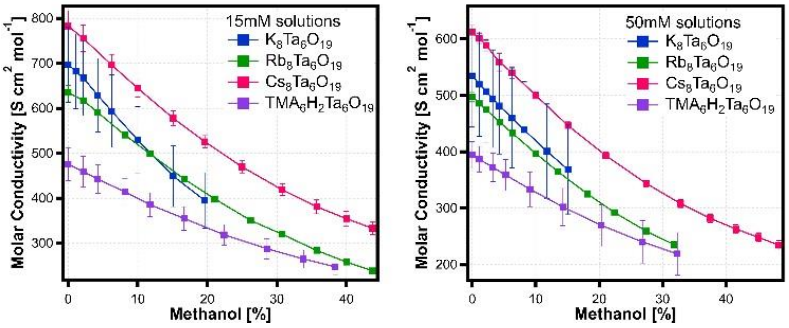

Figure 7.2. Molar conductivity vs. percentage of methanol for 15, and 50 mM $A_8[Nb_6O_{19}]$ on the top and $A_8Ta_6O_{19}$ on the bottom (A = K, Rb, Cs, TMA). Error bars were generated through standard deviation of three measurements.

The individual conductivity contributions of each ion that is not ion-paired were calculated. For solutions in water, the molar conductivity of $[M_6O_{19}]^{8-}$, K^+, Rb^+, Cs^+, and TMA^+ are calculated as 1397.8, 60.3, 55.3, 50.7, and 22.6 $S{\cdot}cm^2/mol$ respectively. Considering the $K_8[Nb_6O_{19}]$ solution for example, with contributions from 8 K^+ ions and one hexaniobate ion, the total molar conductivity should be 1880.6 $S{\cdot}cm^2/mol$. This value is significantly higher than the experimental value of 575.3 $S{\cdot}cm^2/mol$ for the 50mM solution and 739.1 $S{\cdot}cm^2/mol$ for the 15 mM solution. From this we can conclude that not all ions are free in solution, instead some of the alkali cations are associated with anionic POMs and therefore do not contribute to the solution's conductivity. Alternatively, clusters are dimerized by H-bonding. When methanol is added to the solutions, decreasing the solvent polarity, protonation of the clusters and association with alkali cations ensues, ultimately leading to crystallization. Methanol molecules hydrogen-bond with water molecules and prevent a hydration sphere from forming around the ions. This is due to the hydrophobic group in the methanol molecule causing steric inhibition of the water-water hydrogen bonding.[17] This allows cations and anionic clusters to associate more readily. With an increase in the amount of methanol added in the solution, less ionic mobility is observed. This is because there are fewer free ions in solution, and the ions have, on average, larger radii (R) and small charges (q), both diminishing μ_0 in equation 1.

More details about the type of ion associations that occur with addition of methanol can be determined by SWAXS analysis. Solutions were prepared as outlined in table C.1 in Appendix C. Analyzing the structure factor[18] (broad coulombic peak at q ~ 0.05-0.4 Å) of the scattering curves also provides insight into ion association. A structure factor at low q emerges when there is some short-range order of scattering species driven by interactions, such as electrostatic repulsion between two negatively charged clusters. This feature in the scattering data can be fit with two parameters, respectively describing the distance between the interacting species, and the number of species interacting at that distance (**table 7.1**). The structure factor is diminished or eliminated by either shielding cluster interactions through excess electrolyte, or neutralizing the cluster charge by inducing ion association with the counter cations, as observed throughout these studies.

First we discuss the TMA salts of the Lindqvist ions (**figure 7.3, table 7.1**), since there is no alkali-POM association, simplifying the interpretation. We observe a diminishment of the coulombic peak with increasing addition of alcohol. Quantitative fitting of the peak shows an increase in the distance between clusters and a decrease in the number of nearest neighbors.

The TMA hexametalates have the lowest molar conductivity of all counterions in this study. This is not caused by cation-anion pairing, but rather by protonation of the clusters, leading to dimerization, as illustrated in **figure 7.1**. The TMA salts of both hexatantalate and hexaniobate have very similar molar conductivity, with hexatantalate being slightly higher. From the crystal structure of both TMA hexametalates, we know there is a difference in the protonation: TMA hexaniobate is triprotonated, leading to formation of chains in solution; while TMA hexatantalate is diprotonated, leading to cluster dimerization.[14] Protonation of the hexametalate lowers the ion mobility due to increase in size (dimers or bigger) and corresponding decrease in the charge density of the associated clusters. Therefore, we can attribute the slightly higher molar conductivity of TMA hexatantalate to its diprotonated nature compared to triprotonation of TMA hexaniobate. While the scattering curves of the TMA

hexametalates appear to have a second Guinier region (q ~ 0.15-0.25 Å^{-1}), we were unable to fit this data as dimers. This indicates that the monomeric hexametalates is the dominant species in solution while only a small percentage is dimerizing. This dimerization is more evident in the conductivity measurements.

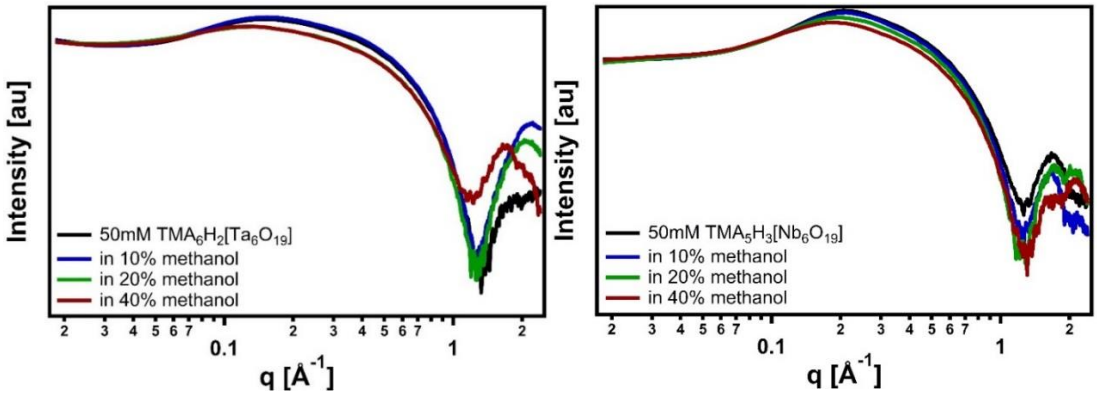

Figure 7.3. Small and wide angle scattering curves for 50 mM $TMA_6H_2[Ta_6O_{19}]$ (left) and $TMA_5H_3[Nb_6O_{19}]$ (right) in water-methanol solutions.

In **figure 7.4**, $Rb_8[Ta_6O_{19}]$ and $Rb_8[Nb_6O_{19}]$ are representative of the minimization of a structure factor through the induction of ion association. Modeled values for the structure factor and radius of 50 mM solutions are provided in **table 7.1**. **Tables C.2** and **C.3** include modeled values for 15 mM solutions. For all systems, regardless of concentration, alkali or Group V metal, the structure factor diminishes as the methanol:water ratio increases. The association of the counterions neutralizes the hexametalates in solution, and therefore ordering is mitigated since partially neutralized clusters have less influence on structuring of neighboring ions or water molecules.

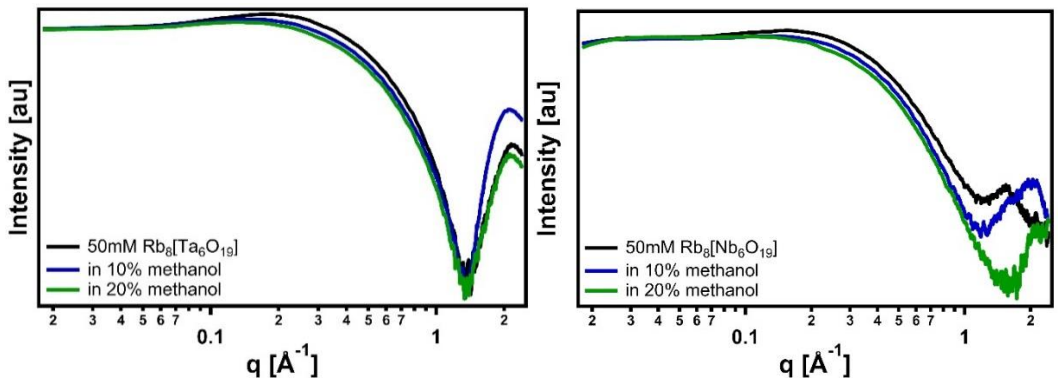

Figure 7.4. Small and wide angle scattering curves for 50 mM $Rb_8[Ta_6O_{19}]$ (left) and $Rb_8[Nb_6O_{19}]$ (right) in water-methanol solutions.

Table 7.1. Structure factors and radii of the scattering species from SWAXS data for 50mM samples of $A_8[Nb_6O_{19}]$ and $A_8[Ta_6O_{19}]$ (A = K, Rb, Cs, TMA).

50mM Samples	Structure Factor		Radius[1] (Å)
	# Nearest Neighbors	Distance (Å)	Guinier
$K_8[Nb_6O_{19}]$ in water	0.4	26.9	4.4
in 10% methanol	0.2	30.0	4.4
in 20% methanol	0.1	34.0	4.4
$Rb_8[Nb_6O_{19}]$ in water	0.3	26.1	4.9
in 10% methanol	0.2	26.8	4.9
in 20% methanol	0.1	33.9	5.1
$Cs_8[Nb_6O_{19}]$ in water	0.2	31.5	5.5
in 10% methanol	0.2	31.7	5.5
in 20% methanol	0.2	32.0	5.5
$TMA_5H_3[Nb_6O_{19}]$ in water	1.5	26.1	3.9
in 10% methanol	1.4	26.0	4.0
in 20% methanol	1.2	27.0	4.0
in 40% methanol	1.0	28.4	4.0
$K_8[Ta_6O_{19}]$ in water	0.3	25.8	4.0
in 10% methanol	0.2	30.3	4.0
in 20% methanol	na	na	na
$Rb_8[Ta_6O_{19}]$ in water	0.5	26.1	4.4
in 10% methanol	0.3	29.2	4.5
in 20% methanol	0.2	31.9	4.6
$Cs_8[Ta_6O_{19}]$ in water	0.3	25.6	5.0
in 10% methanol	0.4	26.0	4.7
in 20% methanol	0.4	26.9	4.9
$TMA_6H_2[Ta_6O_{19}]$ in water	0.8	36.2	3.8
in 10% methanol	0.8	35.8	3.8
in 20% methanol	0.5	41.4	3.8
in 40% methanol	0.5	42.4	3.8

[1]Radius was obtained from Guinier approximation which provides radius of gyration (R_g).

$$\textit{Radius of spherical particles} = \sqrt{5/3} * Rg$$

For each system, the 50 mM solutions have the least change in structure factor with addition of methanol. This is because higher concentration of ions leads to more

pairing, so the decreased solvent polarity has less effect. For example, 15 mM Cs hexatantalate and 50 mM Cs hexatantalate is shown in **figure 7.5** (also **table 7.1**). Comparing the 15 mM solutions of hexaniobate (**figure C.7**) and hexatantalate, we can see that there is a large difference in structure factor dampening for the hexatantalate solutions. The feature observed in the 50 mM Cs hexatantalate between q~0.6-2.0 Å is observed in both the 50 mM Cs hexametalate solutions (see also **figure C.7**), and diminishes with increased methanol in solution. Therefore, it must be related to free Cs in solution. Cs scatters X-rays most strongly of the studied alkalis, so it follows that it will be most apparent as a free cation, or several cations paired via shared hydration spheres. As Cs becomes more strongly associated with the cluster in less polar methanol-water mixes, scattering from the free ion diminishes. This is secondary evidence, in addition to the decreased conductivity, that the methanol is driving ion-pairing.

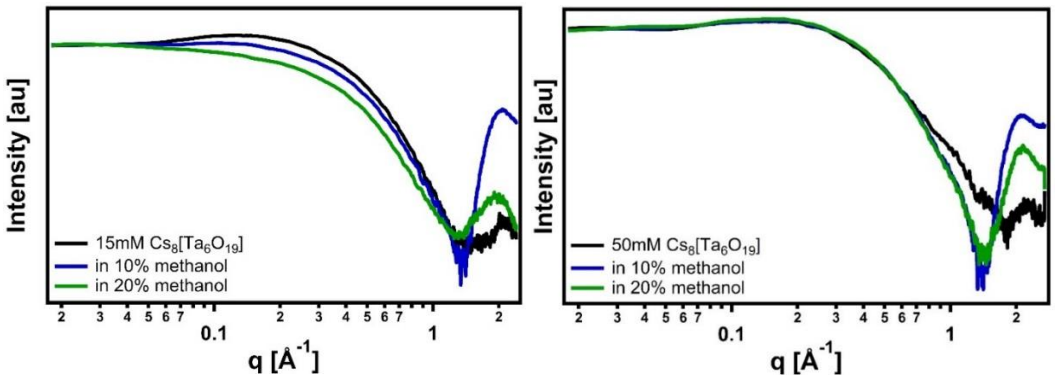

Figure 7.5. Small and wide angle scattering curves for 15 mM $Cs_8[Ta_6O_{19}]$ (left) and 50 mM $Cs_8[Ta_6O_{19}]$ (right) in water-methanol solutions.

The degree of ion pairing depends on the identity of the counter cation and the metal in the cluster. We expected to observe more ion-pairing for less charge dense alkali cations, because their hydration sphere is smaller and more easily displaced. However, this was not necessarily the case, based on the conductivity data. For hexatantalate solutions, the trend in molar conductivity increases from TMA<Rb<K<Cs, while for hexaniobate TMA<Cs<Rb<K. We observe minimal differences between hexatantalate

and hexaniobate molar conductivities for Rb salts at both concentrations. The molar conductivity for the K salt of hexaniobate is on average 6.5% higher than its tantalum analogue. However, the error for K hexatantalate is much larger due to the strong tendency for K hexatantalate to absorb carbonate. This carbonate absorption affects conductivity measurements since the number of ions in solution is increased. For the Cs salts, hexatantalate has on average 25% higher molar conductivity. This indicates that Cs is less associated with hexatantalate than it is for hexaniobate. We also observe a larger dependence on the methanol percentage for hexatantalate.

On the other hand, comparison of the size of scattering species in solution (**table 7.1**) shows they are consistently bigger on average for hexaniobate than hexatantalate. This suggests there is more dimerization in hexaniobate compared to hexatantalate. This is consistent with the observation that hexaniobate is a stronger base than hexatantalate,[19,20] meaning it more readily protonates, leading to dimerization by H-bonding. We were unable to fit the data with two populations (single cluster and dimer of clusters) due to the interference by the structure factor, however the larger radius indicates there is some extent of dimerization while monomeric clusters still dominate.

Cs undergoes exceptional ion association compared to other alkalis,[6] likely due to the Cs-effect that describes partial covalency in the ionic interactions of Cs^+ with anions. For this reason, the consistently higher conductivity of Cs hexatantalate compared to the other hexatantalate alkali salts was not expected. Meanwhile, the hexaniobates follow the expected trend: K>Rb>Cs for all water-methanol mixtures and concentrations. One plausible reason for the unexpected high conductivity of Cs hexatantalate is that the Cs-cluster association is strong enough to prevent dimerization, and this is coupled with the weaker tendency of hexatantalate to protonate, where protonation promotes dimerization.

We also compared the conductivity in log-linear plots to determine which solutions were most dependent on the change in solvent, reflected in the slopes of the plots (**figure C.13** and **table C.4**). For the hexatantalate solutions, there is a trend of increasing negative slope from TMA<Rb≤Cs<K, while for hexaniobate the trend is

TMA<Cs<Rb<K. The TMA salts exhibit the smallest dependence on the change in solvent. This is due to weak interactions between TMA counterions and the hexametalates. Weaker interactions and less ion pairing gives rise to lower dependence on the solvent change and agrees with previous studies on ion pairing.[6] The trend in the alkalis is expected. Higher charge density counterions undergo more ion association with the hexametalates even in neat water and would be less affected by addition of methanol. K shows the strongest dependence on changing solvent due to weaker ion association compared to Cs and Rb. The addition of methanol increases these ionic interactions and allows K to more readily associate with the hexametalate. Only half the amount of alcohol can be added to the K-hexametalate salts, due to poorer solubility. This is observed in the upswing of the scattering data below q=0.04 $Å^{-1}$ indicating aggregation and the onset of crystallization in the 20% methanol solution of 15 mM K hexatantalate. The 50 mM K hexatantalate solution could be prepared with a maximum of 10% methanol, due to crystallization. On the other hand, there is no such evidence of aggregation of the Rb and Cs salts of the hexametalates, in up to 40% methanol solutions.

7.5 CONCLUSIONS

Crystallization or forced precipitation of ions from solution is often induced by diffusion or rapid addition of a 'non-solvent' that has lower polarity than the aqueous solution in which the ions have high solubility. Understanding and optimizing crystallization pathways can be achieved by studies such as presented here, where incipient crystallization is probed in the water-alcohol mixes. A comparison can be made here with a recent study by Bera and Antonio,[18] where the evolution of the structure factor was documented with drying of aqueous solutions of POMs, another pathway to induce crystallization. In their study, ion interaction was forced by increasing concentration through evaporation. In our current study, ion interaction is forced by decreasing polarity of the solution. In Bera's studies, the coulombic peak trended in the opposite direction: in conditions of ion-pairing, the clusters moved closer together, forming a pre-crystallization dense liquid phase. In our study, alkalis and

clusters are forced to associate, and the alkali-cluster assemblies do not interact so strongly. Bera used heteropolyacids $[XW_{12}O_{40}]^{x-}$ (x=3-5) with charge densities (charge per atom) of 0.057- 0.094. The Lindqvist ions of Nb and Ta have considerably higher charge density, 0.32. These charge-densities correlate with their solubility behavior; the higher charge-density clusters are soluble with maximum ion-pairing (anomalous solubility). On the other hand, Cs-salts of heteropolyacids are extremely insoluble, a characteristic exploited in heterogeneous catalysis.[21] The comparison of these two studies could open the door to documenting an understanding of solubility trends. Upon forced ion-association of the group V hexametalates, the high charge of the clusters is neutralized and likewise provides stabilization of the Cs^+ charge. Therefore, the Cs^+ does not bridge to other clusters and solubility is retained. The proton counterions of the group VI clusters of low charge density do not associate strongly with a single cluster; rather they bridge clusters, driving the correlation observed by Bera. This hypothesis will be refined with studies on other cluster systems as well as simple oxoanion salts; in particular a direct comparison of cluster salts with opposite solubility trends under identical conditions, coupled with computational studies. The challenge in particular is characterizing ion associations in the poorly soluble cluster-alkali salts, in which the dissolved state is transient.

7.6 ACKNOWLEDGEMENTS

This work was supported by the U.S. Department of Energy, Office of Basic Energy Sciences, Division of Materials Sciences and Engineering under award DE-SC0010802.

(1) Nyman, M.; Alam, T. M.; Bonhomme, F.; Rodriguez, M. A.; Frazer, C. S.; Welk, M. E. *J. Clust. Sci.* **2006**, *17* (2), 197–219.
(2) Hou, Y.; Nyman, M.; Rodriguez, M. A. *Angew. Chemie* **2011**, *50* (52), 12514–12517.
(3) Lindqvist, I. *Ark. Kemi* **1953**, *5*, 247.
(4) Antonio, M. R.; Nyman, M.; Anderson, T. M. *Angew. Chemie* **2009**, *48* (33), 6136–6140.
(5) Fullmer, L. B.; Molina, P. I.; Antonio, M. R.; Nyman, M. *Dalt. Trans.* **2014**, *43*, 15295–15299.

(6) Sures, D. J.; Sahu , S. K.; Molina, P. I.; Navrotsky, A.; Nyman, M. *ChemistrySelect* **2016**, *1* (9), 1858–1862.
(7) Deblonde, G. J.-P.; Delaunay, N.; Lee, D.; Chagnes, A.; Cote, G.; Gareil, P. *RSC Adv.* **2015**, *5* (79), 64119–64124.
(8) Yin, P.; Li, D.; Liu, T. *Isr. J. Chem.* **2011**, *51* (2), 191–204.
(9) Pigga, J. M.; Liu, T. *Inorganica Chim. Acta* **2010**, *363* (15), 4230–4233.
(10) Liu, G.; Kistler, M. L.; Li, T.; Bhatt, A.; Liu, T. *J. Clust. Sci.* **2006**, *17* (2), 427–443.
(11) Nyman, M.; Burns, P. C. *Chem. Soc. Rev.* **2012**, *41* (22), 7354–7367.
(12) Kojima, T.; Antonio, M. R.; Ozeki, T. *J. Am. Chem. Soc.* **2011**, *133* (19), 7248–7251.
(13) Day, V. W.; Klemperer, W. G.; Maltbie, D. J. *J. Am. Chem. Soc.* **1987**, *109* (10), 2991–3002.
(14) Fullmer, L. B.; Mansergh, R. H.; Zakharov, L. N.; Keszler, D. A.; Nyman, M. *Cryst. Growth Des.* **2015**, *15* (8), 3885–3892.
(15) Anderson, T. M.; Rodriguez, M. A.; Bonhomme, F.; Bixler, J. N.; Alam, T. M.; Nyman, M. *Dalt. Trans.* **2007**, *9226* (40), 4517–4522.
(16) Ilavsky, J.; Jemian, P. R. *J. Appl. Crystallogr.* **2009**, *42* (2), 347–353.
(17) Zhang, N.; Shen, Z.; Chen, C.; He, G.; Hao, C. *J. Mol. Liq.* **2015**, *203* (2015), 90–97.
(18) Bera, M. K.; Antonio, M. R. *J. Am. Chem. Soc.* **2016**, jacs.5b13375.
(19) Balogh, E.; Anderson, T. M.; Rustad, J. R.; Nyman, M.; Casey, W. H. *Inorg. Chem.* **2007**, *46* (17), 7032–7039.
(20) Black, J. R.; Nyman, M.; Casey, W. H. *J. Am. Chem. Soc.* **2006**, *68* (14), 14712–14720.
(21) Soriano-López, J.; Goberna-Ferrón, S.; Vigara, L.; Carbó, J. J.; Poblet, J. M.; Galán-Mascarós, J. R. *Inorg. Chem.* **2013**, *52*, 4753–4755.

CONCLUSIONS

The work presented in this thesis is focused on synthesis and characterization of hexaniobate and hexatantalate. While these two anionic metal-oxide clusters are isostructural ($[Ta_6O_{19}]^{8-}$ and $[Nb_6O_{19}]^{8-}$), thorough characterization of the solution behavior indicates they are not chemically analogous. The tetramethylammonium salts of these clusters were synthesized as aqueous metal oxide thin film precursors. Upon film deposition, hexaniobate crystallized on the surface of the substrate producing a very low quality thin film. Hexatantalate, on the other hand formed an intermediate gel which translated into high quality, dense, and defect free tantalum oxide thin films. Small and wide angle x-ray scattering analysis of the precursors provided insights into the differences in film formation. The tri-protonation of hexaniobate induces hydrogen bonding and subsequent chain formation of the clusters preceding crystallization. Hexatantalate, being a weaker base than the niobium analogue, can only accommodate two protons, inducing dimer formation. This more random orientation of dimers compared to the highly ordered chains of hexaniobate is what controls the film morphology. Highly ordered solutions are more likely to crystallize whereas the disordered dimers of hexatantalate form an amorphous gel-like film layer, making it a substantially more effective precursor. Further work is underway on ion exchanging the tetramethylammonium counterions for protons to further increase the quality of the films. Electrical characterization as well as device performance is also of future interest.

The terminally bound oxygens on the hexametalates can be replaced by peroxide yielding a radiation sensitive $[H_xM_6(O_2)_6O_{13}]^{(8-x)-}$ cluster with applications in lithography. The peroxide substitution of the -yl oxygens can be controlled through stoichiometric additions. Density functional theory calculations concluded that the peroxide addition occurs in a *fac*-like arrangement with perpendicular peroxides as the lowest energy configurations. Analysis of the speciation by electrospray ionization mass spectrometry concluded that stepwise peroxylation is indeed occurring. Small and

wide angle x-ray scattering analysis indicated differences in the cluster-cluster interactions between peroxohexatantalate and peroxohexaniobate. The peroxylation reaction of hexatantalate proceeds at a faster rate than hexaniobate. Peroxohexatantalate also exhibits greater stability than the peroxylated hexaniobate, which reverts back to the parent hexaniobate over eight months. Future work on these species will include analysis of the decomposition of peroxohexaniobate into hexaniobate through loss of peroxide, as well as a study on film formation, characterization, and patternability for lithographic applications.

The tetramethylammonium salts of the hexametalates were compared to the alkali salts in an effort to understand the crystallization process through ion association. By changing concentration and solvent polarity, ion association can be induced and characterized via small and wide angle x-ray scattering as well as conductivity. Counterion to cluster association affects solution behavior by decreasing ionic mobility since the ions are no longer free in solution. Through x-ray scattering, we also observe an increase in the radius of scattering species with increase in ion association. The addition of a less polar solvent is a typical method for inducing precipitation or crystallization of polyoxometalates. By studying the ion association of these clusters with change in solvent, we can gain some insights into the crystallization process as well as the anomalous solubility of the group V polycoltanates.

REFERENCES

Alam, T. M., Nyman, M., Cherry, B. R., Segall, J. M., & Lybarger, L. E. (2004). Multinuclear NMR investigations of the oxygen, water, and hydroxyl environments in sodium hexaniobate. *Journal of the American Chemical Society*, *126*(17), 5610–20. http://doi.org/10.1021/ja0398159

Amador, J. M., Decker, S. R., Lucchini, S. E., Ruther, R. E., & Keszler, D. A. (2014). Patterning chemistry of HafSOx resist. *Proc. of SPIE*, *9051*, 90511A–90511A–6. http://doi.org/10.1117/12.2046605

Anderson, J. T., Munsee, C. L., Hung, C. M., Phung, T. M., Herman, G. S., Johnson, D. C., … Keszler, D. A. (2007). Solution-Processed HafSOx and ZircSOx Inorganic Thin-Film Dielectrics and Nanolaminates. *Advanced Functional Materials*, *17*(13), 2117–2124. article.

Anderson, J. T., Wang, W., Jiang, K., Gustafsson, T., Xu, C., Garfunkel, E. L., & Keszler, D. A. (2015). Chemically Amplified Dehydration of Thin Oxide Films. *ACS Sustainable Chemistry & Engineering*, (3), 1081–1085. http://doi.org/10.1021/sc500824a

Anderson, T. M., Rodriguez, M. A., Bonhomme, F., Bixler, J. N., Alam, T. M., & Nyman, M. (2007). An aqueous route to [Ta6O19]8- and solid-state studies of isostructural niobium and tantalum oxide complexes. *Dalton Transactions*, *9226*(40), 4517–22. http://doi.org/10.1039/b707636c

Antonio, M. R., Nyman, M., & Anderson, T. M. (2009). Direct observation of contact ion-pair formation in aqueous solution. *Angewandte Chemie*, *48*(33), 6136–40. http://doi.org/10.1002/anie.200805323

Baes, C. F., & Mesmer, R. E. (1976). *The Hydrolysis of Cations*. John Wiley & Sons, Inc.

Baetens, R., Jelle, B. P., & Gustavsen, A. (2010). Properties, requirements and possibilities of smart windows for dynamic daylight and solar energy control in buildings: A state-of-the-art review. *Solar Energy Materials and Solar Cells*, *94*(2), 87–105. http://doi.org/10.1016/j.solmat.2009.08.021

Balke, C. W. (1905). Double Fluorides of Tantalum. *Journal of the American Chemical Society*, 1689–1699. http://doi.org/10.1017/CBO9781107415324.004

Balke, C. W., & Smith, E. F. (1908). Observations on Columbium. *Journal of the American Chemical Society*, (11), 1637–1668. http://doi.org/10.1021/ja01953a001

Balogh, E., Anderson, T. M., Rustad, J. R., Nyman, M., & Casey, W. H. (2007). Rates of Oxygen-Isotope Exchange between Sites in the $[H_xTa_6O_{19}]^{(8-x)-}$ (aq) Lindqvist Ion and Aqueous Solutions : Comparisons to $[H_xNb_6O_{19}]^{(8-x)-}$ (aq). *Inorg. Chem.*, *46*(17), 7032–7039.

Bayot, D., & Devillers, M. (2006). Peroxo complexes of niobium(V) and tantalum(V). *Coordination Chemistry Reviews*, *250*(19–20), 2610–2626. http://doi.org/10.1016/j.ccr.2006.04.011

Bera, M. K., & Antonio, M. R. (2016). Crystallization of Keggin Heteropolyanions via a Two-Step Process in Aqueous Solutions. *Journal of the American Chemical Society*, *138*(23), 7282–7288. http://doi.org/10.1021/jacs.5b13375

Berzelius, J. J. (1826). Beitrag zur näheren Kenntniss des Molybdäns. *Annalen Der Physik*, *82*(4), 369–392. http://doi.org/10.1002/andp.18260820402

Black, J. R., Nyman, M., & Casey, W. H. (2006). Rates of Oxygen Exchange between the $[H_xNb_6O_{19}]^{8-x}$ (aq) Lindqvist Ion and Aqueous Solutions. *Journal of the American Chemical Society*, *68*(14), 14712–14720.

Borras-Almenar, J. J., Coronado, E., Muller, A., Pope, M. T., Müller, A., & Pope, M. T. (2003). *Polyoxometalate Molecular Science*. Kluwer Academic Publishers.

Brown, D. H. (1962). The preparation, properties, structure, and spectra of 12-tungstochromic(III) acid. *J. Chem. Soc.*, 3322.

Brown, D. H. (1962). The preparation, properties, structure, and spectra of 12-tungstomanganic(IV) acid and its stability relative to analogous 12-heteropolytungstates. *Journal of the Chemical Society*, 4408.

Brown, D. H. (1963). The ultraviolet and visible spectra of 12-tungstoferric (III) acid. *Spectrochimica Acta*, *19*(10), 1683–1685.

Busche, C., Vilà-Nadal, L., Yan, J., Miras, H. N., Long, D.-L., Georgiev, V. P., … Cronin, L. (2014). Design and fabrication of memory devices based on nanoscale polyoxometalate clusters. *Nature*, 1–5. http://doi.org/10.1038/nature13951

Cardineau, B., Del Re, R., Marnell, M., Al-Mashat, H., Vockenhuber, M., Ekinci, Y., … Brainard, R. L. (2014). Photolithographic properties of tin-oxo clusters using extreme ultraviolet light (13.5 nm). *Microelectronic Engineering*, *127*, 44–50. http://doi.org/10.1016/j.mee.2014.04.024

Chaneliere, C., Autran, J. L., Balland, B., Devine, R. A. B., & Balland, B. (1998). Tantalum pentoxide (Ta_2O_5) thin films for advanced dielectric applications. *Reports: A Review Journal*, *22*, 269–322.

Chiang, T., Yeh, B., & Wager, J. F. (2015). Amorphous IGZO Thin-Film Transistors With Ultrathin Channel Layers. *IEEE Transactions on Electron Devices*, *62*(11), 3692–3696.

Coronado, E., & Gómez-García, C. J. (1998). Polyoxometalate-Based Molecular Materials. *Chemical Reviews*, *98*(1), 273–296. Retrieved from http://www.ncbi.nlm.nih.gov/pubmed/22850732

Cruywagen, J. J. (2000). Protonation, oligomerization, and condensation reactions of vanadate(V), molybdate(VI), and tungstate(VI). *Advances in Inorganic Chemistry*, *49*, 127–182.

Day, V. W., Klemperer, W. G., & Maltbie, D. J. (1987). Where Are the Protons in $H_3V_{10}O_{28}^{3-}$? *Journal of the American Chemical Society*, *109*(10), 2991–3002.

Deblonde, G. J.-P., Delaunay, N., Lee, D., Chagnes, A., Cote, G., & Gareil, P. (2015). First investigation of polyoxoniobate and polyoxotantalate aqueous speciation by capillary zone electrophoresis. *RSC Adv.*, *5*(79), 64119–64124. http://doi.org/10.1039/C5RA11521C

Deshlahra, P., & Iglesia, E. (2014). Methanol Oxidative Dehydrogenation on Oxide Catalysts: Molecular and Dissociative Routes and Hydrogen Addition Energies as Descriptors of Reactivity. *Journal of Physical Chemistry C*, *118*(45), 26115–26129. http://doi.org/10.1021/jp507922u

Epifani, M., Zamani, R., Arbiol, J., Fabrega, C., Andreu, T., Pace, G. B., … Morante, J. R. (2014). Soft chemistry routes to transparent metal oxide thin films. The case of sol-gel synthesis and structural characterization of Ta_2O_5 thin films from tantalum chloromethoxide. *Thin Solid Films*, *555*, 39–41. http://doi.org/10.1016/j.tsf.2013.05.139

Ezhilvalavan, S., & Tseng, T.-Y. (1999). Preparation and properties of tantalum pentoxide (Ta_2O_5) thin films for ultra large scale integrated circuits (ULSIs) application - A review. *Journal of Materials Science: Materials in Electronics*, *10*, 9–31.

Fairbrother, F. (1967). *The Chemistry of Niobium and Tantalum*. Elsevier Publishing Company.

Fan, L., Degen, M., Bendle, S., Grupido, N., & Ilavsky, J. (2010). The Absolute Calibration of a Small-Angle Scattering Instrument with a Laboratory X-ray Source. *Journal of Physics: Conference Series*, *247*, 12005. http://doi.org/10.1088/1742-6596/247/1/012005

Feigin, L. A., & Svergun, D. I. (1987). *Structure Analysis by Small-Angle X-Ray and Neutron Scattering*. New York, New York: Springer Science.

Fullmer, L. B., Mansergh, R. H., Zakharov, L. N., Keszler, D. A., & Nyman, M. (2015). Nb2O5 and Ta2O5 thin films from polyoxometalate precursors: A single proton makes a difference. *Crystal Growth & Design*, *15*(8), 3885–3892. http://doi.org/10.1021/acs.cgd.5b00508

Fullmer, L. B., Molina, P. I., Antonio, M. R., & Nyman, M. (2014). Contrasting ion-association behaviour of Ta and Nb polyoxometalates. *Dalton Trans.*, *43*, 15295–15299. http://doi.org/10.1039/C4DT02394C

Gao, S.-Y., Lu, J., & Cao, R. (2015). Development of polyoxometalate-based material photocatalysts for organic dye degradation under visible light. In *Trends in Polyoxometalates Research* (pp. 265–280).

Gates, J. M., Sudowe, R., Stavsetra, L., Ali, M. N., Calvert, M. G., Dragojević, I., … Nitsche, H. (2009). Extraction of niobium and tantalum isotopes using organophosphorus compounds. Part I - Extraction of “carrier-free” metal concentrations from HCl solutions. *Radiochimica Acta*, *97*(3), 167–172. http://doi.org/10.1524/ract.2009.1583

Glatter, O., & Kratky, O. (1982). *Small Angle X-ray Scattering*.

Goberna-Ferrón, S., Park, D.-H., Amador, J. M., Keszler, D. A., & Nyman, M. (2016). Amphoteric Aqueous Hafnium Cluster Chemistry. *Angewandte Chemie International Edition*, 1–5. http://doi.org/10.1002/anie.201601134

Goberna-Ferrón, S., Soriano-López, J., Galán-Mascarós, J. R., & Nyman, M. (2015). Solution Speciation and Stability of Cobalt-Polyoxometalate Water Oxidation Catalysts by X-ray Scattering. *European Journal of Inorganic Chemistry*, *2015*(17), 2833–2840. http://doi.org/10.1002/ejic.201500404

Guinier, A., & Fournet, G. (1955). *Small-Angle Scattering of X-rays*.

Hou, Y., Fast, D. B., Ruther, R. E., Amador, J. M., Fullmer, L. B., Decker, S. R., … Nyman, M. (2015). The atomic level journey from aqueous polyoxometalate to metal oxide. *Journal of Solid State Chemistry*, *221*, 418–425. http://doi.org/10.1016/j.jssc.2014.09.039

Hou, Y., Nyman, M., & Rodriguez, M. A. (2011). Soluble heteropolyniobates from the bottom of Group IA. *Angewandte Chemie*, *50*(52), 12514–7. http://doi.org/10.1002/anie.201104478

Hou, Y., Zakharov, L. N., & Nyman, M. (2013). Observing assembly of complex inorganic materials from polyoxometalate building blocks. *Journal of the American Chemical Society*, *135*(44), 16651–7. http://doi.org/10.1021/ja4086484

Ilavsky, J., & Jemian, P. R. (2009). Irena : tool suite for modeling and analysis of small-angle scattering. *Journal of Applied Crystallography*, *42*(2), 347–353. http://doi.org/10.1107/S0021889809002222

Isobe, M., & Marumo, F. (1978). The Crystal Structure of Hexakis(isopropylammonium) Dihydrogenoctamolybdate(6-) Dihydrate, $(C_3H_{10}N)_6[H_2Mo_8O_{28}]$ $2H_2O$. *Acta Cryst.*, *34*(Sept), 2728–2731.

Jackson, M. N., Kamunde-Devonish, M. K., Hammann, B. A., Wills, L. A., Fullmer, L. B., Hayes, S. E., … Johnson, D. W. (2015). An overview of selected current approaches to the characterization of aqueous inorganic clusters. *Dalton Trans.*, *44*(39), 16982–17006. http://doi.org/10.1039/C5DT01268F

Jaeger, R. C. (2002). *Introduction to Microelectronic Fabrication* (2nd ed.). Upper Saddle River, NJ: Prentice Hall.

Ji, Y., Huang, L., Hu, J., Streb, C., & Song, Y.-F. (2015). Polyoxometalate-functionalized nanocarbon materials for energy conversion, energy storage and sensor systems. *Energy Environ. Sci.*, *8*(3), 776–789. http://doi.org/10.1039/C4EE03749A

Jiang, K., Zakutayev, A., Stowers, J., Anderson, M. D., Tate, J., McIntyre, D. H., … Keszler, D. A. (2009). Low-temperature, solution processing of TiO_2 thin films and fabrication of multilayer dielectric optical elements. *Solid State Sciences*, *11*(9), 1692–1699. article. http://doi.org/10.1016/j.solidstatesciences.2009.05.026

Joshi, P. C., & Cole, M. W. (1999). Influence of postdeposition annealing on the enhanced structural and electrical properties of amorphous and crystalline Ta_2O_5 thin films for dynamic random access memory applications. *Journal of Applied Physics*, *86*(2), 871. http://doi.org/10.1063/1.370817

Kaledin, A. L., Duin, A. C. T. Van, Hill, C. L., & Musaev, D. G. (2013). Parameterization of Reactive Force Field : Dynamics of the [Nb6O19Hx] (8−x)− Lindqvist Polyoxoanion in Bulk Water. *The Journal of Physical Chemistry A*, *117*, 6967–6974.

Katsoulis, D. E. (1998). A Survey of Applications of Polyoxometalates. *Chemical Reviews*, *98*(1), 359–388. Retrieved from http://www.ncbi.nlm.nih.gov/pubmed/11851510

Keggin, J. F. (1934). The structure and formula of 12-phosphotungstic acid. *Proceedings of the Royal Society A: Mathematical, Physical and Engineering Sciences*, *144*, 75–100. http://doi.org/10.1098/rspa.1934.0035

Kinnan, M. K., Creasy, W. R., Fullmer, L. B., Schreuder-Gibson, H. L., & Nyman, M. (2014). Nerve Agent Degradation with Polyoxoniobates. *European Journal of Inorganic Chemistry*, 2361–2367. http://doi.org/10.1002/ejic.201400016

Kojima, T., Antonio, M. R., & Ozeki, T. (2011). Solvent-driven association and dissociation of the hydrogen-bonded protonated decavanadates. *Journal of the American Chemical Society*, *133*(19), 7248–51. http://doi.org/10.1021/ja110781f

Lee, G. R., & Crayston, J. A. (1991). Electrochromic Nb_2O_5 and Nb_2O_5- Silicone Composite Thin Films prepared by Sol-Gel Processing. *J.Mater.Chem.*, *1*(3), 381–386.

Lenzmann, F., Shklover, V., Brooks, K., & Atzel, M. G. R. (2000). Mesoporous Nb_2O_5 Films : Influence of Degree of Crystallinity on Properties. *Journal of Sol-Gel Science and Technology*, *19*, 175–180.

Li, D., Yin, P., & Liu, T. (2012). Supramolecular architectures assembled from amphiphilic hybrid polyoxometalates. *Dalton Transactions*, *41*(10), 2853–61. http://doi.org/10.1039/c2dt11882c

Li, L., Chakrabarty, S., Spyrou, K., Ober, C. K., & Giannelis, E. P. (2015). Studying the Mechanism of Hybrid Nanoparticle Photoresists: Effect of Particle Size on Photo-Patterning. *Chemistry of Materials*, *27*, 5027–5031. http://doi.org/10.1021/acs.chemmater.5b01506

Lide, D. R., & Haynes, W. M. (Eds.). (2009). *CRC Handbook of Chemistry and Physics* (90th ed.). Boca Raton, FL: CRC Press (Taylor and Francis Group).

Lindqvist, I. (1953). No Title. *Ark. Kemi*, *5*, 247.

Lintanf-Salaün, A., Mantoux, A., Djurado, E., & Blanquet, E. (2010). Atomic layer deposition of tantalum oxide thin films for their use as diffusion barriers in microelectronic devices. *Microelectronic Engineering*, *87*(3), 373–378. http://doi.org/10.1016/j.mee.2009.06.015

Liu, G., Kistler, M. L., Li, T., Bhatt, A., & Liu, T. (2006). Counter-ion Association Effect in Dilute Giant Polyoxometalate [AsIII12CeIII16(H2O)36W148O524]76-({W148}) and [Mo132O372(CH3COO)30(H. *Journal of Cluster Science*, *17*(2), 427–443. http://doi.org/10.1007/s10876-006-0063-z

Llordés, A., Wang, Y., Fernandez-Martinez, A., Xiao, P., Lee, T., Poulain, A., … Milliron, D. J. (2016). Linear topology in amorphous metal oxide electrochromic

networks obtained via low-temperature solution processing. *Nature Materials*, *1*(August 2016). http://doi.org/10.1038/nmat4734

Long, D.-L., Burkholder, E., & Cronin, L. (2007). Polyoxometalate clusters, nanostructures and materials: from self assembly to designer materials and devices. *Chemical Society Reviews*, *36*(1), 105–21. http://doi.org/10.1039/b502666k

López, X., Carbó, J. J., Bo, C., & Poblet, J. M. (2012). Structure, properties and reactivity of polyoxometalates: a theoretical perspective. *Chemical Society Reviews*, *41*(22), 7537–71. http://doi.org/10.1039/c2cs35168d

Mansergh, R. H., Fullmer, L. B., Park, D.-H., Nyman, M., & Keszler, D. A. (2016). Reaction Pathway: Aqueous Hexatantalate Clusters to High-Density Tantalum Oxide Nanofilms. *Chemistry of Materials*, *28*(5), 1553–1558. http://doi.org/10.1021/acs.chemmater.6b00078

Masse, J. P., Szymanowski, H., Zabeida, O., Amassian, A., Klemberg-Sapieha, J. E., & Martinu, L. (2006). Stability and effect of annealing on the optical properties of plasma-deposited Ta_2O_5 and Nb_2O_5 films. *Thin Solid Films*, *515*(4), 1674–1682. http://doi.org/10.1016/j.tsf.2006.05.047

Matsumoto, M., Ozawa, Y., & Yagasaki, A. (2011). Which is the most basic oxygen in $[Ta_6O_{19}]^{8-}$? — Synthesis and structural characterization of $[H_2Ta_6O_{19}]^{6-}$. *Inorganic Chemistry Communications*, *14*(1), 115–117. http://doi.org/10.1016/j.inoche.2010.09.045

Matsumoto, M., Ozawa, Y., & Yagasaki, A. (2012). Long hydrogen-bonded rod of molecular oxide: a hexatantalate tetramer. *Inorganic Chemistry*, *51*(11), 5991–3. http://doi.org/10.1021/ic3004883

Matsumoto, M., Ozawa, Y., Yagasaki, A., & Zhe, Y. (2013). Decatantalate--the last member of the group 5 decametalate family. *Inorganic Chemistry*, *52*(14), 7825–7. http://doi.org/10.1021/ic400864e

Mensinger, Z. L., Wang, W., Keszler, D. A., & Johnson, D. W. (2012). Oligomeric Group 13 hydroxide compounds--a rare but varied class of molecules. *Chemical Society Reviews*, *41*(3), 1019–30. http://doi.org/10.1039/c1cs15216e

Meyers, S. T., Anderson, J. T., Hong, D., Hung, C. M., Wager, J. F., & Keszler, D. A. (2007). Solution-processed aluminum oxide phosphate thin-film dielectrics. *Chemistry of Materials*, *19*(16), 4023–4029. article.

Miao, F., Strachan, J. P., Yang, J. J., Zhang, M.-X., Goldfarb, I., Torrezan, A. C., … Williams, R. S. (2011). Anatomy of a nanoscale conduction channel reveals the

mechanism of a high-performance memristor. *Advanced Materials (Deerfield Beach, Fla.)*, *23*(47), 5633–40. http://doi.org/10.1002/adma.201103379

Miras, H. N., Yan, J., Long, D.-L., & Cronin, L. (2012). Engineering polyoxometalates with emergent properties. *Chemical Society Reviews*, *41*(22), 7403–30. http://doi.org/10.1039/c2cs35190k

Moffat, J. B. (2001). *Metal-Oxygen Clusters: The Surface and Catalytic Properties of Heteropoly Oxometalates*. New York, New York: Kluwer Academic/Plenum Publishers.

Molina, P. I., Sures, D. J., Miró, P., Zakharov, L. N., & Nyman, M. (2015). Bridging the opposite chemistries of tantalum and tungsten polyoxometalates. *Dalton Trans.*, (44), 15813–15822. http://doi.org/10.1039/C5DT02290H

Nelson, W. H., & Tobias, R. S. (1964). Polycondensed anions of the transition metals-Light scattering and ultracentrifugation with schlieren and interference optics of alkaline niobium (V) solutions. *Canadian Journal of Chemistry*, *42*, 731. http://doi.org/10.1017/CBO9781107415324.004

Nico, C., Monteiro, T., & Graça, M. P. F. (2016). Niobium oxides and niobates physical properties: Review and prospects. *Progress in Materials Science*, *80*, 1–37. http://doi.org/10.1016/j.pmatsci.2016.02.001

Nyman, M. (2011). Polyoxoniobate chemistry in the 21st century. *Dalton Transactions*, *40*(32), 8049–58. http://doi.org/10.1039/c1dt10435g

Nyman, M., Alam, T. M., Bonhomme, F., Rodriguez, M. A., Frazer, C. S., & Welk, M. E. (2006). Solid-state Structures and Solution Behavior of Alkali Salts of the [Nb6O19]8- Lindqvist Ion. *Journal of Cluster Science*, *17*(2), 197–219. http://doi.org/10.1007/s10876-006-0049-x

Nyman, M., & Burns, P. C. (2012). A comprehensive comparison of transition-metal and actinyl polyoxometalates. *Chemical Society Reviews*, *41*(22), 7354–67. http://doi.org/10.1039/c2cs35136f

Nyman, M., & Fullmer, L. B. (2015). Small Angle X-ray Scattering of Group V Polyoxometalates. In L. Ruhlmann & D. Schaming (Eds.), *Trends in Polyoxometalates Research* (pp. 151–170). Nova Science Publishers, Inc.

O'Boyle, N., Banck, M., James, C. A., Morley, C., Vandermeersch, T., & Hutchinson, G. R. (2011). Open Babel: An open chemical toolbox. *Journal of Cheminformatics*, *3*(33).

Ohlin, C. A. (2012). Reaction dynamics and solution chemistry of polyxoxmetalates by electrospray ionization mass spectrometry. *Chemistry An Asian Journal*, *7*, 262–270.

Ohlin, C. A., Villa, E. M., & Casey, W. H. (2009). One-pot synthesis of the decaniobate salt $[N(CH_3)_4]_6[Nb_{10}O_{28}]\cdot 6H_2O$ from hydrous niobium oxide. *Inorganica Chimica Acta*, *362*(4), 1391–1392. http://doi.org/10.1016/j.ica.2008.06.006

Ohlin, C. A., Villa, E. M., Fettinger, J. C., & Casey, W. H. (2008). Distinctly different reactivities of two similar polyoxoniobates with hydrogen peroxide. *Angewandte Chemie*, *47*(43), 8251–4. http://doi.org/10.1002/anie.200803688

Oleksak, R. P., Ruther, R. E., Luo, F., Fairley, K. C., Decker, S. R., Stickle, W. F., … Keszler, D. A. (2014). Chemical and Structural Investigation of High-Resolution Patterning with HafSOx. *Applied Materials & Interfaces*, *6*, 2917–2921.

Omwoma, S., Chen, W., Gore, C. T., & Song, Y. F. (2015). Polyoxometalate-containing multifunctional materials. In *Trends in Polyoxometalates Research* (pp. 281–354).

Pauw, B. R. (2014). Looking at Nothing-A weblog about small-angle scattering. Retrieved January 1, 2016, from http://www.lookingatnothing.com/index.php/archives/1309

Pigga, J. M., & Liu, T. (2010). Stability of Keplerate polyoxometalate macroanionic assemblies in salt-containing aqueous solutions. *Inorganica Chimica Acta*, *363*(15), 4230–4233. http://doi.org/10.1016/j.ica.2010.06.062

Pigga, J. M., Teprovich, J. A., Flowers, R. A., Antonio, M. R., & Liu, T. (2010). Selective monovalent cation association and exchange around Keplerate polyoxometalate macroanions in dilute aqueous solutions. *Langmuir*, *26*(12), 9449–56. http://doi.org/10.1021/la100467p

Plassmeyer, P. N., Archila, K., Wager, J. F., & Page, C. J. (2015). Lanthanum aluminum oxide thin-film dielectrics from aqueous solution. *ACS Applied Materials and Interfaces*, *7*(3), 1678–1684. http://doi.org/10.1021/am507271e

Prakash, A., Jana, D., & Maikap, S. (2013). TaOx-based resistive switching memories: prospective and challenges. *Nanoscale Research Letters*, *8*(1), 418. http://doi.org/10.1186/1556-276X-8-418

Proust, A., Matt, B., Villanneau, R., Guillemot, G., Gouzerh, P., & Izzet, G. (2012). Functionalization and post-functionalization: a step towards polyoxometalate-based materials. *Chemical Society Reviews*, *41*(22), 7605–22. http://doi.org/10.1039/c2cs35119f

Putnam, C. D., Hammel, M., Hura, G. L., & Tainer, J. A. (2007). X-ray solution scattering (SAXS) combined with crystallography and computation: defining accurate macromolecular structures, conformations and assemblies in solution. *Quarterly Reviews of Biophysics*, *40*(3), 191–285. http://doi.org/10.1017/S0033583507004635

Rani, R. A., Zoolfakar, A. S., O'Mullane, A. P., Austin, M. W., & Kalantar-Zadeh, K. (2014). Thin films and nanostructures of niobium pentoxide: fundamental properties, synthesis methods and applications. *Journal of Materials Chemistry A*, *2*, 15683–15703. http://doi.org/10.1039/C4TA02561J

Reisman, A., & Holtzberg, F. (1970). Nb_2O_5 and Ta_2O_5 structure and physical properties. In A. M. Alper (Ed.), *High Temperature Oxides Part II: Oxides of Rare Earths, Titanium, Zirconium, Hafnium, Niobium, and Tantalum* (pp. 217–255). New York, New York: Academic Press Inc.

Richter, P., Plassmeyer, P. N., Harzdorf, J., Rüffer, T., Lang, H., Kalbacova, J., … Salvan, G. (2016). High Quality Magnetic Oxide Thin Films Prepared via Aqueous Solution Processing. *Chemistry of Materials*, *28*(14), 4917–4927. http://doi.org/10.1021/acs.chemmater.6b01001

Ruther, R. E., Baker, B. M., Son, J.-H., Casey, W. H., & Nyman, M. (2014). Hafnium Sulfate Prenucleation Clusters and the Hf18 Polyoxometalate Red Herring. *Inorganic Chemistry*, *53*(8), 4234–4242. JOUR. http://doi.org/10.1021/ic500375v

Schaming, D., & Ruhlmann, L. (2015). Polyoxometalates associated with porphyrins used as efficient visible photosenstizers. In *Trends in Polyoxometalates Research* (pp. 237–264).

Schnablegger, H., & Singh, Y. (2011). *The SAXS Guide* (Second Rev). Anton Paar.

Sécheresse, F. (2013). *Polyoxometalate Chemistry: Some Recent Trends*. World Scientific Publishing.

Selezneva, K. I., & Nisel'son, L. A. (1968). Preparation and Properties of Ammonium Orthoperoxoniobate and Orthoperoxotantalate. *Russian Journal of Inorganic Chemistry*, *13*(1), 45–47.

Seshan, K. (2012). *Handbook of Thin Fim Deposition: Techniques, Processes, and Technologies*. William Andrew.

Shannon, R. D. (1976). Revised Effective Ionic Radii and Systematic Studies of Interatomic Distances in Halides and Chalcogenides. *Acta Cryst.*, *A32*, 751–767.

Sharpless, N. E., & Munday, J. S. (1957). Infrared Spectra of Some Heteropoly Acid Salts. *Analytical Chemistry*, *29*(11), 1619–1622.

Sheldrick, G. M. (1998). *Bruker/Siemens Area Detector Absorption Correction Program*. Madison, WI: Bruker AXS.

SHELXTL-6.10. (n.d.). *Program for Structure Solution, Refinement and Presentation*. Madison, WI: Bruker AXS Inc.

Si, Y.-L., & Wang, E.-B. (2009). Theoretical study of the electronic properties of peroxohexaniobate, $[H_2Nb_6O_{13}(O_2)_6]^{5-}$, by DFT. *Molecular Physics*, *107*(15), 1521–1526. http://doi.org/10.1080/00268970902953604

Smith, S. W., Wang, W., Keszler, D. A., & Conley, J. F. (2014). Solution based prompt inorganic condensation and atomic layer deposition of Al_2O_3 films: A side-by-side comparison. *Journal of Vacuum Science & Technology A: Vacuum, Surfaces, and Films*, *32*(4), 41501. http://doi.org/10.1116/1.4874806

Son, J.-H., Park, D.-H., Keszler, D. A., & Casey, W. H. (2015). Acid-Stable Peroxoniobophosphate Clusters To Make Patterned Films. *Chemistry - A European Journal*, *21*(18), 6727–6731. http://doi.org/10.1002/chem.201500684

Sone, Y., Kishimoto, A., Kudo, T., & Ikeda, K. (1996). Reversible electrochromic performance of Prussian blue coated with proton conductive $Ta_2O_5 \cdot nH_2O$ film. *Solid State Ionics*, *83*(1), 135–143. http://doi.org/10.1016/0167-2738(95)00226-X

Soriano-López, J., Goberna-Ferrón, S., Vigara, L., Carbó, J. J., Poblet, J. M., & Galán-Mascarós, J. R. (2013). Cobalt polyoxometalates as heterogeneous water oxidation catalysts. *Inorganic Chemistry*, *52*, 4753–4755. http://doi.org/10.1021/ic4001945

Sures, D. J., Molina, P. I., Miró, P., Zakharov, L. N., & Nyman, M. (2016). Cesium salts of niobo-tungstate isopolyanions with intermediate group V–group VI character. *New J. Chem.*, *40*, 928–936. http://doi.org/10.1039/C5NJ02914G

Sures, D. J., Sahu , S. K., Molina, P. I., Navrotsky, A., & Nyman, M. (2016). Distinctive Interactions of Cesium and Hexaniobate in Water. *ChemistrySelect*, *1*(9), 1858–1862. http://doi.org/10.1002/slct.201600493

Svergun, D. I. (1999). Restoring low resolution structure of biological macromolecules from solution scattering using simulated annealing. *Biophysical Journal*, 2879–2886.

Tsigdinos, G. A., & Hallada, C. J. (1968). Molybdovanadophosphoric acids and their salts. I. Investigation of methods of preparation and characterization. *Inorganic Chemistry*, *7*(3), 437–441.

Turkevich, J., & Hopkins Hubbell, H. (1951). Low Angle X-ray Diffraction of Colloidal Gold and Carbon Black. *Journal of the American Chemical Society*, *73*(1).

Tytko, K. H., Mehmke, J., Kurad, D., & Fischer, S. (1999). *Bonding and Charge Distribution in Polyoxometalates- A Bond Valence Approach*. (D. M. P. Mingos, Ed.). Springer.

Van der Sluis, P., & Spek, A. L. (1990). No Title. *Acta Cryst. Sect. A*, *A46*, 197–201.

Velten, D., Eisenbarth, E., Schanne, N., & Breme, J. (2004). Biocompatible Nb_2O_5 thin films prepared by means of the sol-gel process. *Journal of Materials Science: Materials in Medicine*, *15*, 457–461. http://doi.org/10.1023/B:JMSM.0000021120.86985.f7

Wikipedia Contributors. (2016). Coltan. Retrieved September 9, 2016, from https://en.wikipedia.org/w/index.php?title=Coltan&oldid=736973211

Yamase, T. (1998). Photo- and Electrochromism of Polyoxometalates and Related Materials. *Chemical Reviews*, *98*(1), 307–326. Retrieved from http://www.ncbi.nlm.nih.gov/pubmed/11851508

Yasaka, M. (2010). X-ray thin-film measurement techniques V. X-ray reflectivity measurement. *The Rigaku Journal*, *26*(2), 1–9.

Yin, P., Li, D., & Liu, T. (2011). Counterion Interaction and Association in Metal-Oxide Cluster Macroanionic Solutions and the Consequent Self-Assembly. *Israel Journal of Chemistry*, *51*(2), 191–204. http://doi.org/10.1002/ijch.201000079

Zhang, N., Shen, Z., Chen, C., He, G., & Hao, C. (2015). Effect of hydrogen bonding on self-diffusion in methanol / water liquid mixtures : A molecular dynamics simulation study. *Journal of Molecular Liquids*, *203*(2015), 90–97. http://doi.org/10.1016/j.molliq.2014.12.047

Zuo, X., Goshe, A., Zhang, R., & Tiede, D. M. SolX: A Computer Program for Solution Molecular X-ray Scattering Technique Simulations. *Journal of Applied Crystallography*.

Center for Sustainable Materials Chemistry. Retrieved June 28, 2016, from http://sustainablematerialschemistry.org/

www.materialsproject.org.

APPENDIX A: SUPPORTING INFORMATION FOR CHAPTER 5

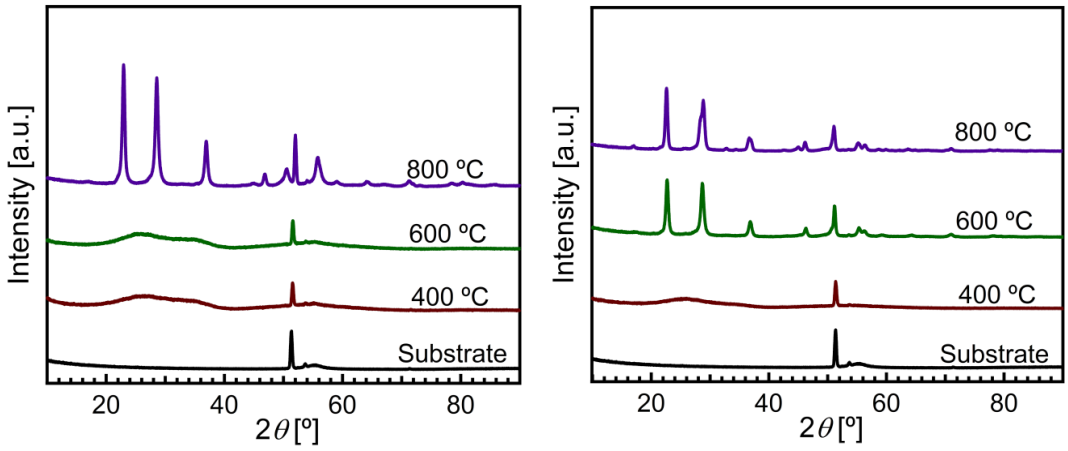

Figure A.1. Grazing Incidence XRD on thin films of Ta_2O_5 (left) and Nb_2O_5 (right).

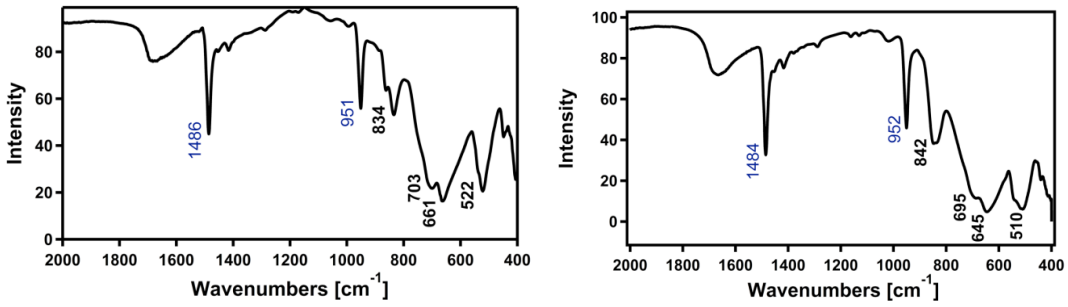

Figure A.2. IR spectra of **Ta6** (left) and **Nb6** (right) show sharp peaks at 1486, 951 cm^{-1} and 1484, 952 cm^{-1} respectively, which is characteristic of TMAOH. The peak at 834 for **Ta6** and 842 cm^{-1} for **Nb6** can be attributed to the vibration of a terminal M-O bond. The peaks at 703 and 661 for **Ta6** and 695 and 645 for **Nb6** can be attributed to bridging M-O-M vibrations.[22] The bond between a metal and the central oxygen is represented by peaks at 522 cm^{-1} and 510 cm^{-1} for **Ta6** and **Nb6** respectively.

Table A.1. Crystallographic data and structure refinement for **Ta6** and **Nb6**.

Complex	**Ta6**	**Nb6**
Empirical Formula	$Ta_6O_{42.5}C_{24}H_{74}N_6$	$Nb_6O_{25}C_{20}H_{63}N_5$
Formula Weight (g/mol)	2214.41	1668.15
Crystal System	triclinic	triclinic
Space Group	P -1 (2)	P -1 (2)
a (Å)	12.7073(7)	13.719(6)
*b (*Å)	14.0596(7)	14.024(7)
c (Å)	20.9034(12)	16.390(8)
α (˚)	71.310(1)	67.008(8)
β (˚)	76.972(2)	76.671(8)
γ (˚)	72.889(1)	84.904(9)
V (Å^3)	3345.40(32)	2825(2)
Z	2	2
T (K)	150	173
d (g·cm^{-3})	2.196	1.565
λ (Å)	0.71073	0.71073
μ (mm^{-1})	9.865	1.263
Reflections Measured	96486	44542
Independent	24199	13966
R_{int}	0.0514	0.1417
Independent Parameters	712	525
R1	0.0317	0.0609
wR2	0.0666	0.1041

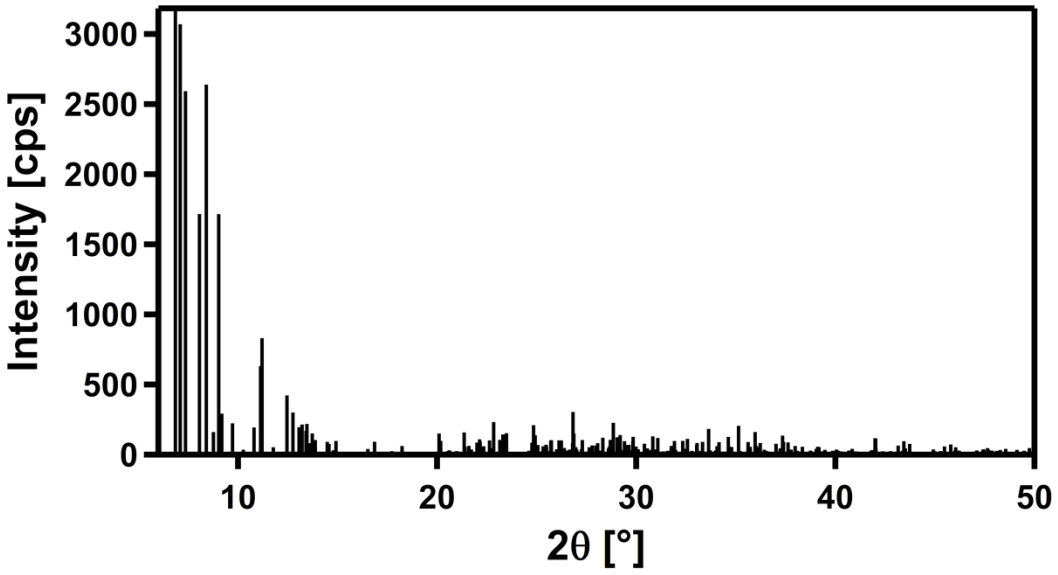

Figure A.3. Simulated XRD pattern from single crystal data of **Ta6**.

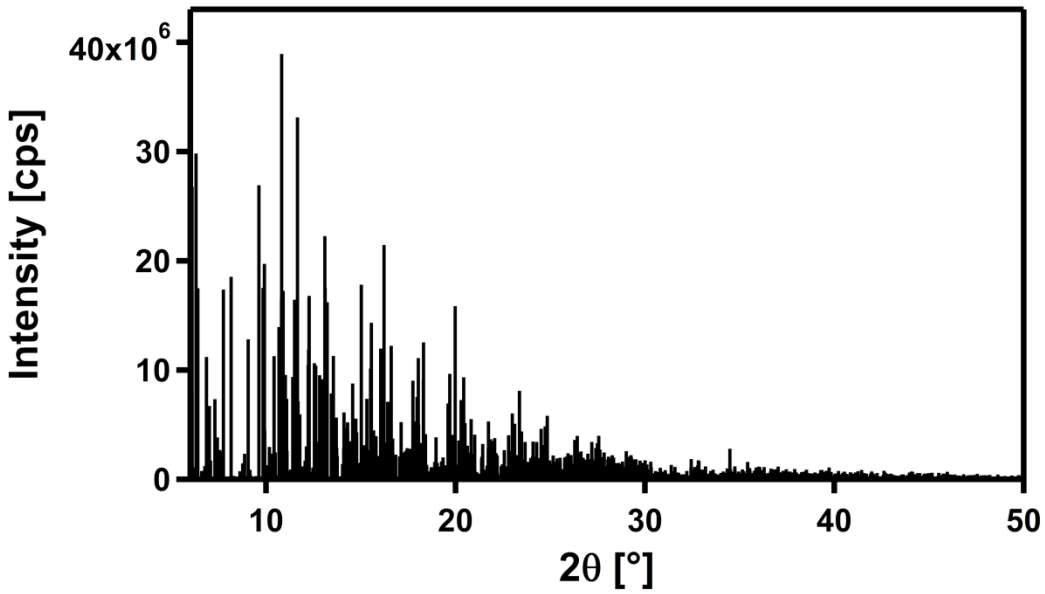

Figure A.4. Simulated XRD pattern from single crystal data of **Nb6**.

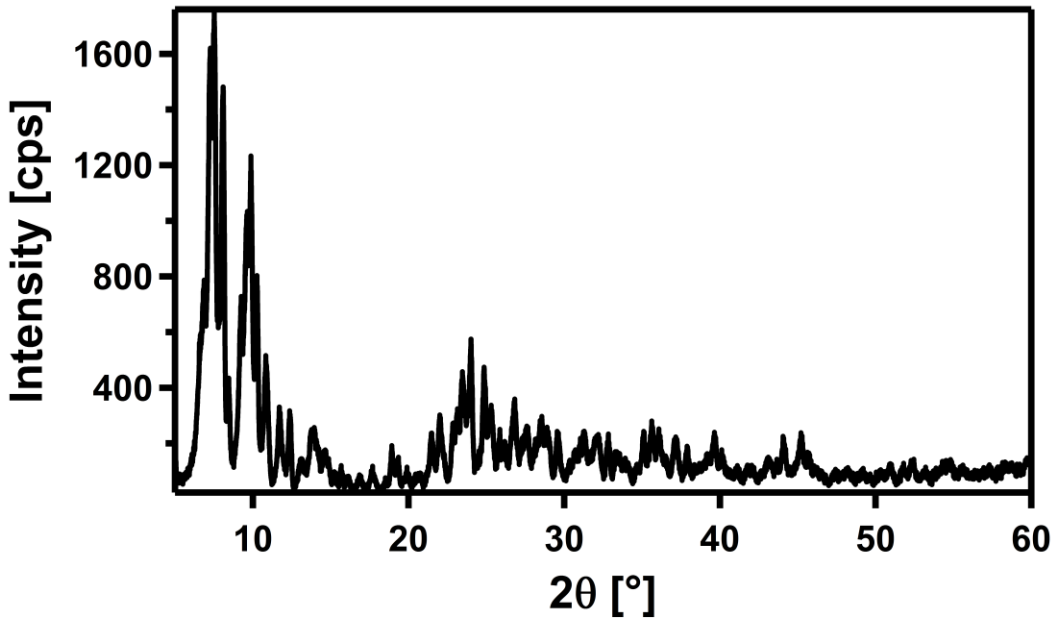

Figure A.5. Powder XRD pattern of **Nb6**.

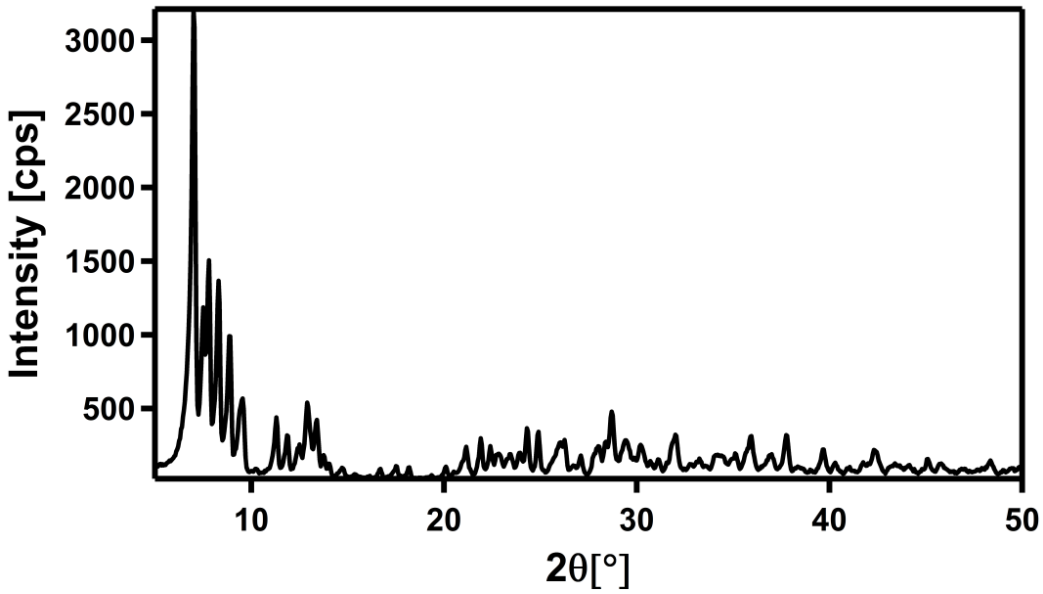

Figure A.6. Powder XRD pattern of **Ta6**.

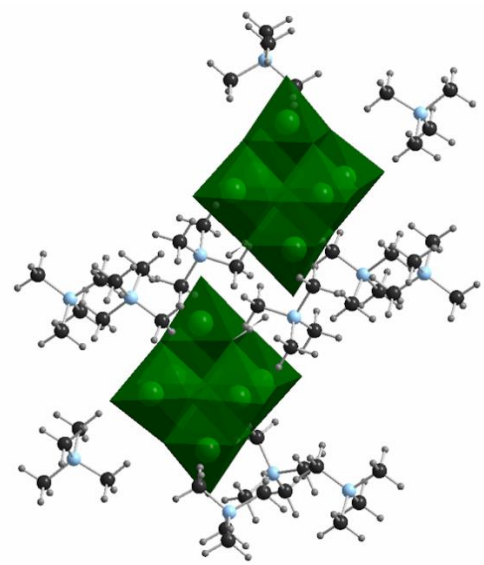

Figure A.7. Unit cell representation of tetramethylammonium salt of $[M_6O_{19}]^{8-}$

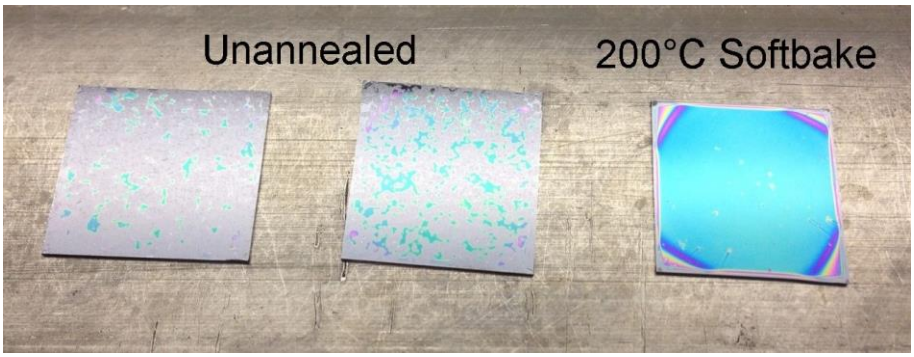

Figure A.8. Films deposited from **Nb6** precursor. Unannealed films showing crystallization of the precusor (left). Softbaked film showing smoother surface (right).

Table A.2. Size distribution results from Irena, **Ta6** and **Nb6** in water (left) and 0.2M TMAOH solution (right)

Water	***Diameter Pop 1(Å)***	***Diameter Pop 2 (Å)***
10 mM **Nb6**	6.25	--
10 mM **Ta6**	6.33	16.91
25 mM **Nb6**	6.41	--
25 mM **Ta6**	6.52	17.13
50 mM **Nb6**	6.77	15.94
50 mM **Ta6**	6.44	17.04

0.2M TMAOH	***Diameter Pop 1(Å)***	***Diameter Pop 2 (Å)***
10 mM **Nb6**	6.52	--
10 mM **Ta6**	6.07	--
25 mM **Nb6**	6.45	--
25 mM **Ta6**	6.50	--
50 mM **Nb6**	6.58	15.33
50 mM **Ta6**	6.89	16.58

APPENDIX B: SUPPORTING INFORMATION FOR CHAPTER 6

Table B.1. Theoretical and experimental Raman frequencies for peroxohexaniobate.

Mode	Observed Frequency [cm^{-1}]	Calculated Frequency [cm^{-1}]	Scaled Calculated Frequency [cm^{-1}]
M=O stretching	849, 817	874, 829	880, 834
O_2 vibration	865	920	865
M-O_2 stretching	617	604	568
M-O bending	456, 371	478, 430	450, 433

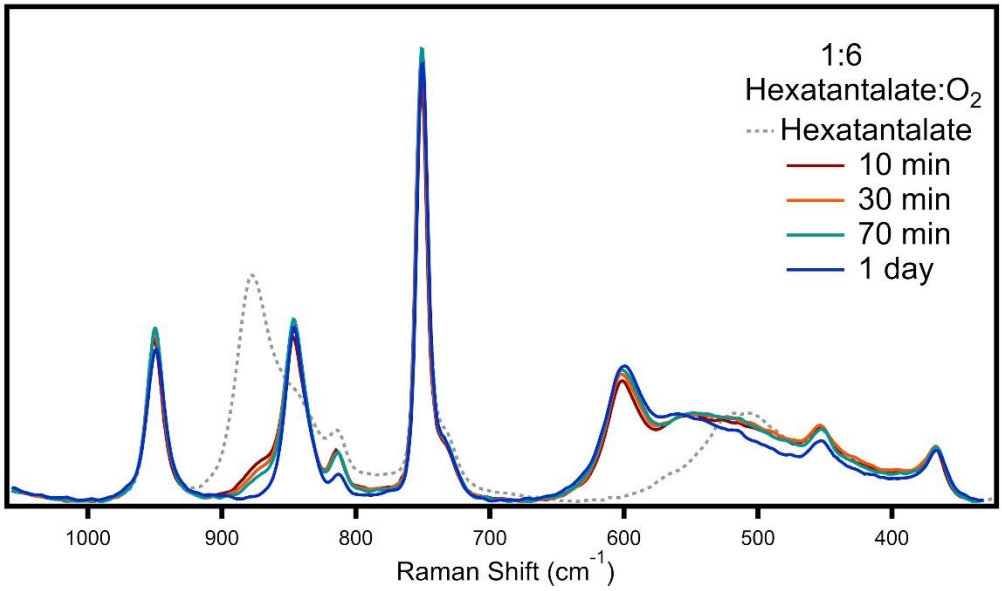

Figure B.1. Raman spectra monitoring the peroxylation of hexatantalate over time.

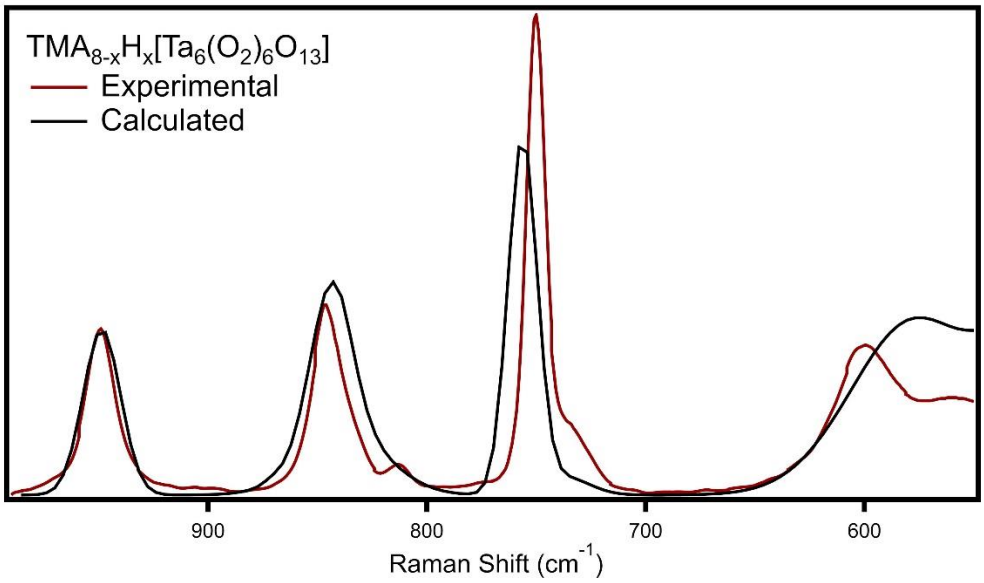

Figure B.2. Experimental and Calculated Raman spectra for peroxohexatantalate.

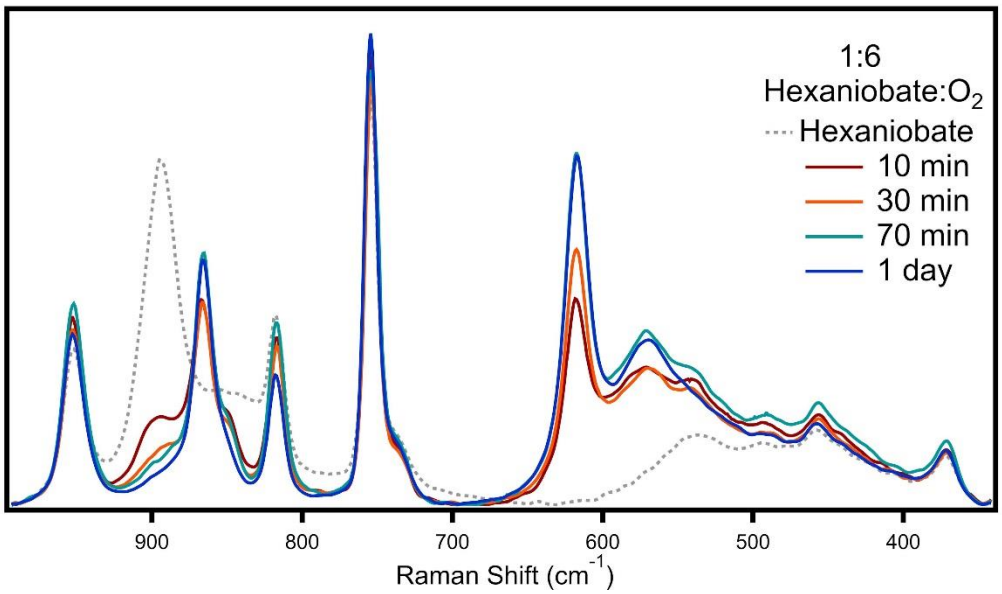

Figure B.3. Raman spectra monitoring the peroxylation of hexaniobate over time.

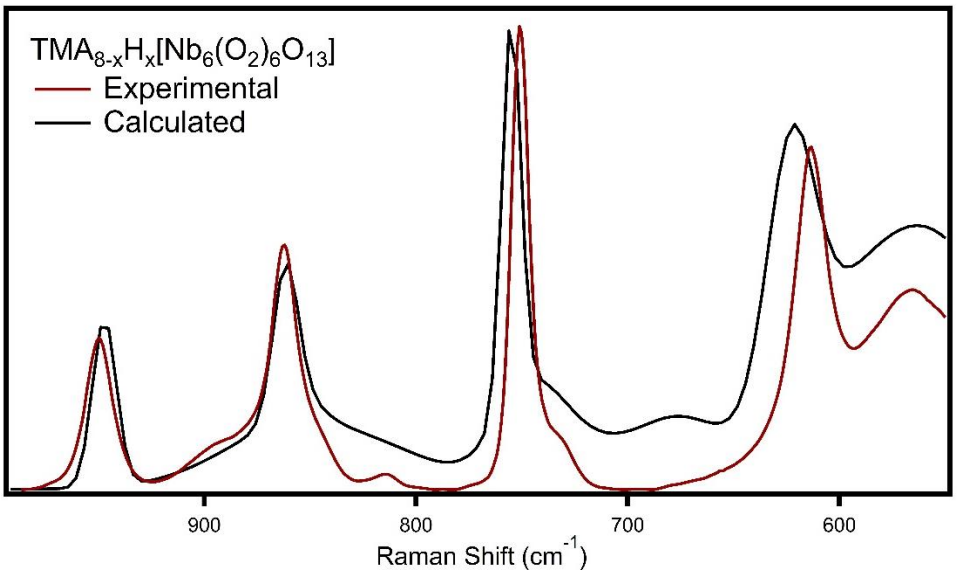

Figure B.4. Experimental and Calculated Raman spectra for peroxohexaniobate.

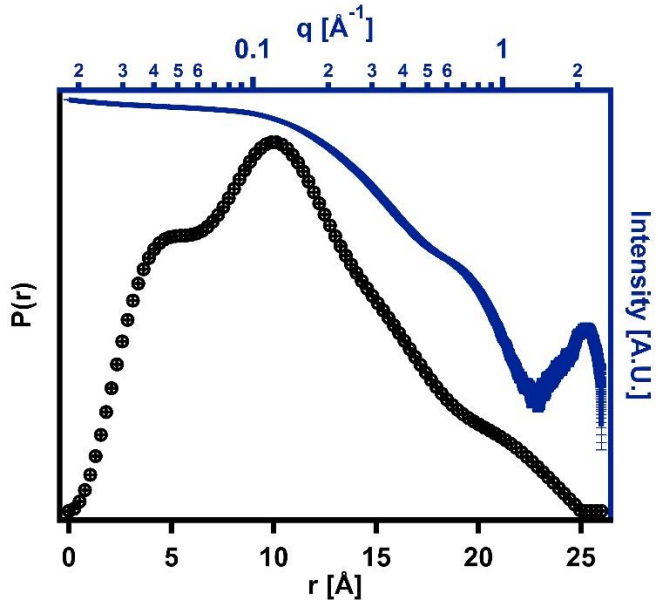

Figure B.5. Pair distance distribution function analysis (black) of peroxohexatantalate, with scattering curve (blue) overlaid.

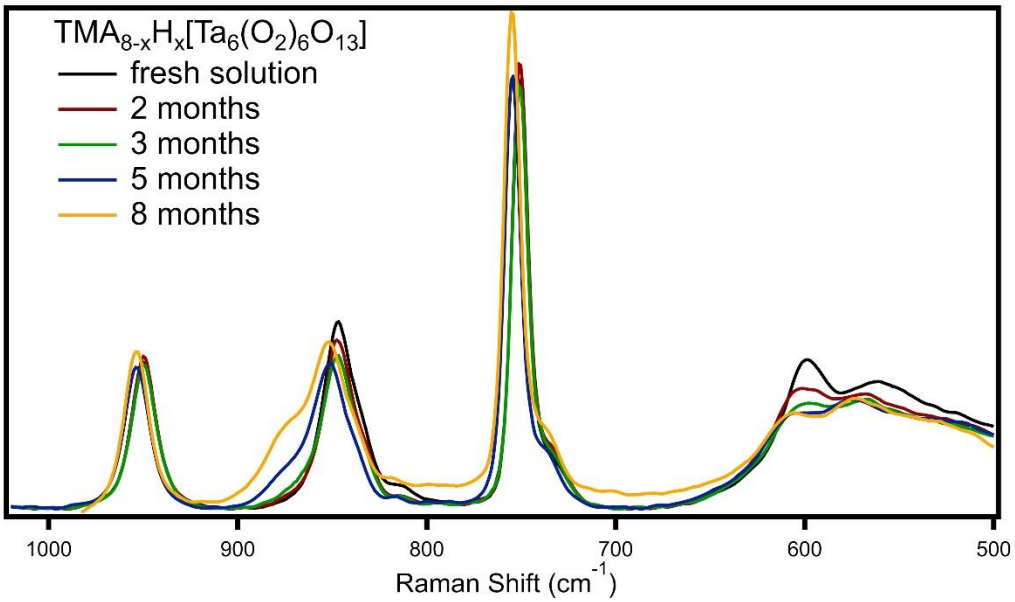

Figure B.6. Raman spectra of peroxohexatantalate dissolved in water.

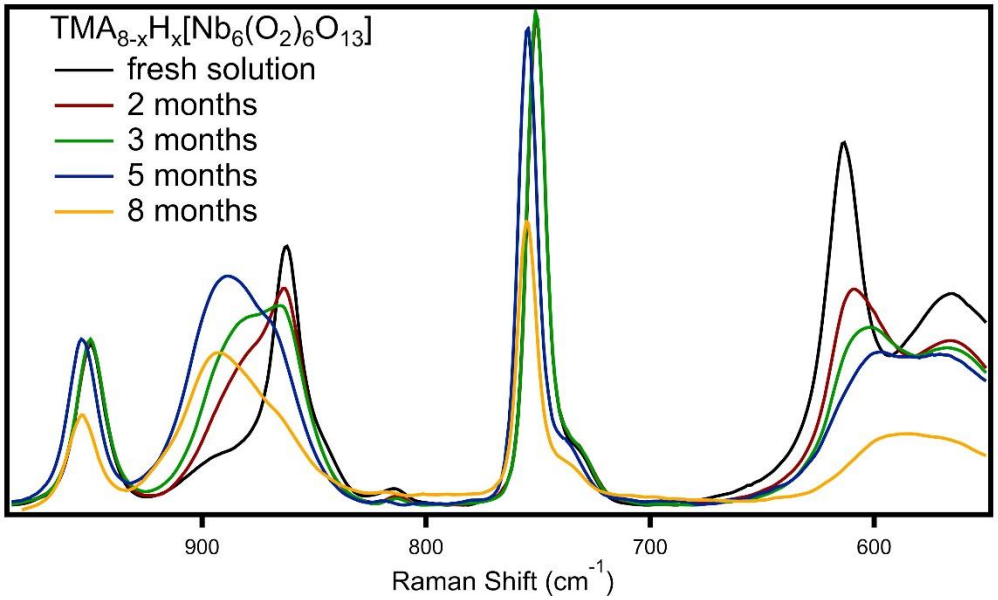

Figure B.7. Raman spectra of peroxohexaniobate dissolved in water.

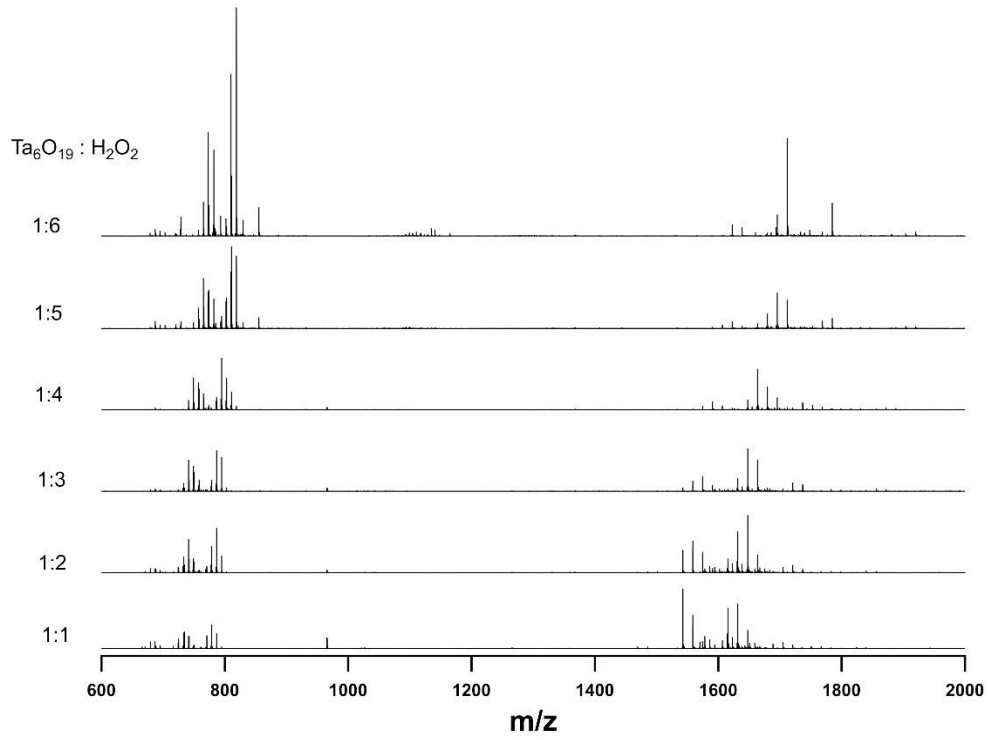

Figure B.8. ESI-MS of reaction solutions of peroxylated hexatantalate.

Table B.2. All species identified by ESI-MS for mono-peroxylated hexatantalate.

Mono-peroxylated hexatantalate reaction solution			
Species	**Experimental m/z**	**Calculated m/z**	**Relative Abundance (%)**
$Ta_6(O_2)_2O_{14}^{-2}$	686.795	686.789	12.97
$TMAHTa_6(O_2)O_{16}^{-2}$	724.329	724.351	10.02
$TMAH_3Ta_6O_{18}^{-2}$	725.336	725.358	16.69
$TMAHTa_6(O_2)O_{16}^{-2} \cdot H_2O$	733.333	733.356	26.77
$TMAH_5Ta_6O_{19}^{-2}$	734.341	734.364	28.11
$TMAH_3Ta_6(O_2)_2O_{16}^{-2}$	741.335	741.343	21.34
$TMAH_5Ta_6(O_2)O_{18}^{-2}$	742.339	742.351	20.79
$TMA_2H_4Ta_6O_{19}^{-2}$	770.884	770.908	22.10

$TMA_2H_4Ta_6(O_2)O_{18}^{-2}$	778.882	778.906	40.44
$TMA_2H_4Ta_6(O_2)_2O_{17}^{-2}$	786.879	786.893	25.34
$TMATa_3(O_2)_6\ (OH)_5^{-1} \cdot 4H_2O$	965.974	965.936	18.39
$TMA_2H_5Ta_6O_{19}^{-1}$	**1542.788**	**1542.825**	**100**
$TMA_2H_5Ta_6(O_2)O_{18}^{-1}$	1558.782	1558.819	56.89
$TMA_2H_5Ta_6(O_2)_2O_{17}^{-1}$	1574.773	1574.814	13.10
$TMA_3H_4Ta_6(O_2)O_{18}^{-1}$	1631.872	1631.909	75.71
$TMA_3H_4Ta_6(O_2)_2O_{17}^{-1}$	1647.864	1647.904	30.72
$TMA_4H_3Ta_6(O_2)O_{18}^{-1}$	1704.958	1704.998	11.32

Table B.3. All species identified by ESI-MS for di-peroxylated hexatantalate.

Di-peroxylated hexatantalate reaction solution			
Species	**Experimental m/z**	**Calculated m/z**	**Relative Abundance (%)**
$TMAHTa_6(O_2)O_{16}^{-2}$	724.328	724.351	10.50
$TMAHTa_6(O_2)_2O_{15}^{-2}$	732.326	732.348	11.50
$TMAHTa_6(O_2)O_{16}^{-2} \cdot H_2O$	733.333	733.356	28.65
$TMAH_5Ta_6O_{19}^{-2}$	734.341	734.364	14.44
$TMAH_3Ta_6(O_2)_2O_{16}^{-2}$	741.332	741.343	57.66
$TMAH_5Ta_6(O_2)O_{18}^{-2}$	742.338	742.351	23.25
$TMAH_3Ta_6(O_2)_3O_{15}^{-2}$	749.331	749.351	25.30
$TMAH_5Ta_6(O_2)_2O_{17}^{-2}$	750.336	750.359	19.32
$TMA_2H_4Ta_6O_{19}^{-2}$	770.884	770.906	11.02
$TMA_2H_2Ta_6(O_2)_2O_{16}^{-2}$	777.874	777.898	13.93
$TMA_2H_4Ta_6(O_2)O_{18}^{-2}$	778.882	778.896	45.64
$TMA_2H_4Ta_6(O_2)_2O_{17}^{-2}$	786.880	786.903	78.31

$TMA_2H_4Ta_6(O_2)_3O_{16}^{-2}$	794.876	794.901	30.06
$TMA_2H_5Ta_6O_{19}^{-1}$	1542.786	1542.825	39.36
$TMA_2H_5Ta_6(O_2)O_{18}^{-1}$	1558.781	1558.819	54.91
$TMA_2H_5Ta_6(O_2)_2O_{17}^{-1}$	1574.778	1574.794	36.37
$TMA_3H_4Ta_6(O_2)O_{18}^{-1}$	1631.870	1631.888	71.83
$TMA_3H_4Ta_6(O_2)_2O_{17}^{-1}$	**1647.865**	**1647.904**	**100**
$TMA_3H_4Ta_6(O_2)_3O_{16}^{-1}$	1663.857	1663.898	31.80
$TMA_4H_3Ta_6(O_2)_2O_{17}^{-1}$	1720.954	1720.993	13.53

Table B.4. All species identified by ESI-MS for tri-peroxylated hexatantalate.

Tri-peroxylated hexatantalate reaction solution			
Species	**Experimental m/z**	**Calculated m/z**	**Relative Abundance (%)**
$TMAHTa_6(O_2)O_{16}^{-2} \cdot H_2O$	733.332	733.356	19.72
$TMAH_3Ta_6(O_2)_2O_{16}^{-2}$	741.331	741.343	75.05
$TMAH_5Ta_6(O_2)O_{18}^{-2}$	742.337	742.351	27.36
$TMAH_3Ta_6(O_2)_4O_{14}^{-2}$	757.328	757.348	14.22
$TMAH_5Ta_6(O_2)_3O_{16}^{-2}$	758.332	758.356	27.60
$TMA_2H_2Ta_6(O_2)_2O_{16}^{-2}$	777.873	777.898	12.86
$TMA_2H_2Ta_6(O_2)_3O_{15}^{-2}$	785.870	785.895	18.21
$TMA_2H_4Ta_6(O_2)_2O_{17}^{-2}$	786.880	786.903	97.30
$TMA_2H_4Ta_6(O_2)_3O_{16}^{-2}$	794.877	794.901	80.61
$TMA_2H_5Ta_6(O_2)O_{18}^{-1}$	1558.780	1558.819	24.86
$TMA_2H_5Ta_6(O_2)_2O_{17}^{-1}$	1574.775	1574.794	34.86
$TMA_2H_5Ta_6(O_2)_3O_{16}^{-1}$	1590.773	1590.809	14.95
$TMA_3H_4Ta_6(O_2)O_{18}^{-1}$	1631.869	1631.888	32.19
$TMA_3H_4Ta_6(O_2)_2O_{17}^{-1}$	**1647.865**	**1647.904**	**100**

$TMA_3H_4Ta_6(O_2)_3O_{16}^{-1}$	1663.859	1663.898	75.37
$TMA_4H_3Ta_6(O_2)_2O_{17}^{-1}$	1720.953	1720.993	20.33
$TMA_4H_3Ta_6(O_2)_3O_{16}^{-1}$	1736.950	1736.988	16.06

Table B.5. All species identified by ESI-MS for tetra-peroxylated hexatantalate.

Tetra-peroxylated hexatantalate reaction solution			
Species	**Experimental m/z**	**Calculated m/z**	**Relative Abundance (%)**
$TMAH_3Ta_6(O_2)_2O_{16}^{-2}$	741.330	741.343	18.88
$TMAH_3Ta_6(O_2)_3O_{15}^{-2}$	749.328	749.351	62.78
$TMAH_5Ta_6(O_2)_2O_{17}^{-2}$	750.334	750.359	15.14
$TMAH_3Ta_6(O_2)_5\ O_{13}^{-2}$	765.324	765.346	32.03
$TMAH_5Ta_6(O_2)_4\ O_{15}^{-2}$	766.329	766.354	23.75
$TMA_2H_2Ta_6(O_2)_3O_{15}^{-2}$	785.872	785.895	17.50
$TMA_2H_4Ta_6(O_2)_2O_{17}^{-2}$	786.879	786.903	24.43
$TMA_2Ta_6(O_2)_4O_{13}^{-2} \cdot H_2O$	793.870	793.893	21.59
$TMA_2H_4Ta_6(O_2)_3O_{16}^{-2}$	**794.877**	**794.901**	**100**
$TMA_2H_2Ta_6(O_2)_5O_{13}^{-2}$	801.866	801.890	18.02
$TMA_2H_4Ta_6(O_2)_4O_{15}^{-2}$	802.874	802.898	61.31
$TMA_2H_4Ta_6(O_2)_5O_{14}^{-2}$	810.871	810.896	35.39
$TMA_2H_5Ta_6(O_2)_3O_{16}^{-1}$	1590.770	1590.809	16.41
$TMA_3H_4Ta_6(O_2)_2O_{17}^{-1}$	1647.862	1647.904	19.89
$TMA_3H_4Ta_6(O_2)_3O_{16}^{-1}$	1663.860	1663.898	79.39
$TMA_3H_4Ta_6(O_2)_4O_{15}^{-1}$	1679.854	1679.893	45.52

$TMA_3H_4Ta_6(O_2)_5O_{14}^{-1}$	1695.847	1695.888	24.07
$TMA_4H_3Ta_6(O_2)_3O_{16}^{-1}$	1736.943	1736.988	14.43
$TMA_4H_3Ta_6(O_2)_4O_{15}^{-1}$	1752.941	1752.982	10.18

Table B.6. All species identified by ESI-MS for penta-peroxylated hexatantalate.

Penta-peroxylated hexatantalate reaction solution			
Species	**Experimental m/z**	**Calculated m/z**	**Relative Abundance (%)**
$TMAH_3Ta_6(O_2)_4O_{14}^{-2}$	757.325	757.348	25.42
$TMAH_3Ta_6(O_2)_5\ O_{13}^{-2}$	765.323	765.346	61.41
$TMAH_5Ta_6(O_2)_4\ O_{15}^{-2}$	766.330	766.354	26.23
$H_8Ta_6(O_2)_6O_{14}^{-2} \cdot 2H_2O$	772.816	772.820	33.13
$TMAH_3Ta_6(O_2)_6O_{12}^{-2}$	773.321	773.343	45.49
$TMAH_5Ta_6(O_2)_5\ O_{14}^{-2}$	774.327	774.351	47.26
$TMAHTa_6(O_2)_6O_{11}^{-2} \cdot 2H_2O$	782.325	782.349	36.48
$TMA_2H_2Ta_6(O_2)_5O_{13}^{-2}$	801.866	801.890	33.07
$TMA_2H_4Ta_6(O_2)_4O_{15}^{-2}$	802.873	802.898	37.80
$TMA_2H_2Ta_6(O_2)_6O_{12}^{-2}$	809.863	809.888	69.45
$TMA_2H_4Ta_6(O_2)_5O_{14}^{-2}$	**810.871**	**810.896**	**100**
$TMA_2H_4Ta_6(O_2)_6O_{13}^{-2}$	818.869	818.893	88.69
$TMA_3H_4Ta_6(O_2)_4O_{15}^{-1}$	1679.854	1679.893	18.04
$TMA_3H_4Ta_6(O_2)_5O_{14}^{-1}$	1695.850	1695.888	43.96
$TMA_3H_4Ta_6(O_2)_6O_{13}^{-1}$	1711.843	1711.883	34.98
$TMA_4H_3Ta_6(O_2)_6O_{13}^{-1}$	1784.931	1784.972	12.80

Table B.7. All species identified by ESI-MS for hexa-peroxylated hexatantalate.

Hexa-peroxylated hexatantalate reaction solution			
Species	**Experimental m/z**	**Calculated m/z**	**Relative Abundance (%)**
$TMAH_3Ta_6(O_2)_5\ O_{13}^{-2}$	765.323	765.346	14.87
$H_8Ta_6(O_2)_6O_{14}^{-2} \cdot 2H_2O$	772.816	772.820	32.76
$TMAH_3Ta_6(O_2)_6O_{12}^{-2}$	773.321	773.343	45.51
$TMAH_5Ta_6(O_2)_5\ O_{14}^{-2}$	774.328	774.351	13.66
$TMAHTa_6(O_2)_6O_{11}^{-2} \cdot 2H_2O$	782.325	782.349	37.65
$TMA_2H_2Ta_6(O_2)_6O_{12}^{-2}$	809.865	809.888	70.95
$TMA_2H_4Ta_6(O_2)_5O_{14}^{-2}$	810.871	810.896	26.40
$TMA_2H_4Ta_6(O_2)_6O_{13}^{-2}$	**818.870**	**818.893**	**100**
$TMA_3H_3Ta_6(O_2)_6O_{13}^{-2}$	855.413	855.438	12.53
$TMA_3H_4Ta_6(O_2)_6O_{13}^{-1}$	1711.845	1711.883	42.87
$TMA_4H_3Ta_6(O_2)_6O_{13}^{-1}$	1784.931	1784.972	14.53

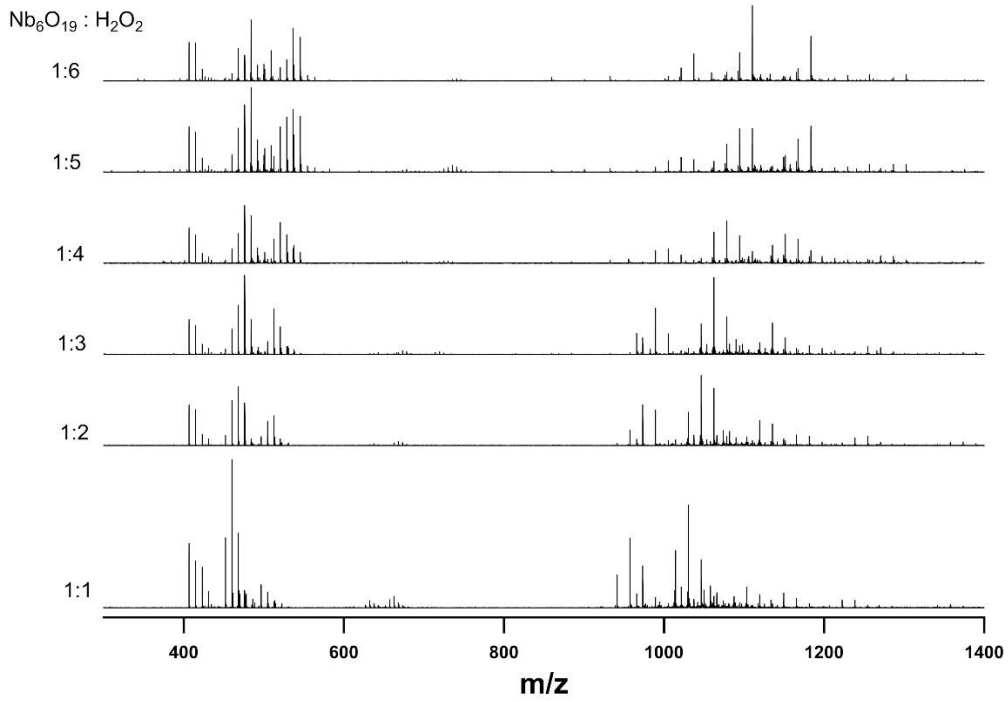

Figure B.9. ESI-MS of reaction solutions of peroxylated hexaniobate.

Table B.8. All species identified by ESI-MS for mono-peroxylated hexaniobate.

Mono-peroxylated hexaniobate reaction solutions			
Species	**Experimental m/z**	**Calculated m/z**	**Relative Abundance (%)**
$Nb_3O_8^{-1}$	406.666	406.678	43.73
$TMA_6H_4Nb_2O_{11}^{-2} \cdot 2H_2O$	423.164	423.196	27.58
$TMA_2Nb(OH)_8^{-1} \cdot 3H_2O$	431.161	431.154	11.23
$TMAHNb_6O_{17}^{-2}$	452.214	452.228	47.42
$TMAHNb_6(O_2)O_{16}^{-2}$	**460.212**	**460.226**	**100**
$TMAHNb_6(O_2)_2O_{15}^{-2}$	468.210	468.223	50.80

$TMAHNb_6(O_2)_3O_{14}^{-2}$	476.207	476.221	11.72
$TMA_2Nb_6(O_2)O_{16}^{-2}$	496.756	496.770	15.81
$TMA_2Nb_6(O_2)_2O_{15}^{-2}$	504.752	504.768	10.54
$TMANb_6O_{16}^{-1} \cdot 3H_2O$	941.460	941.486	22.35
$TMANb_6(O_2)O_{15}^{-1} \cdot 3H_2O$	957.456	957.480	47.07
$TMAH_2Nb_6(O_2)_2O_{15}^{-1} \cdot 2H_2O$	973.450	973.475	28.50
$TMA_2HNb_6O_{17}^{-1} \cdot 2H_2O$	1014.548	1014.575	38.79
$TMA_2HNb_6(O_2)O_{16}^{-1} \cdot 2H_2O$	1030.535	1030.570	69.63
$TMA_2H_3Nb_6(O_2)_2O_{16}^{-1} \cdot H_2O$	1046.539	1046.565	32.69
$TMA_{15}H_8Nb_5(O_2)_6O_{19}^{-2} \cdot 2H_2O$	1058.083	1057.956	15.04
$TMA_3Nb_6(O_2)_5O_{12}^{-1} \cdot H_2O$	1149.635	1149.628	10.06

Table B.9. All species identified by ESI-MS for di-peroxylated hexaniobate.

Di-peroxylated hexaniobate reaction solutions			
Species	**Experimental m/z**	**Calculated m/z**	**Relative Abundance (%)**
$Nb_3O_8^{-1}$	406.667	406.678	57.94
$TMA_6H_4Nb_2O_{11}^{-2} \cdot 2H_2O$	423.165	423.196	16.18
$TMA_2Nb(OH)_8^{-1} \cdot 3H_2O$	431.161	431.154	10.31
$TMAHNb_6O_{17}^{-2}$	452.214	452.228	14.82
$TMAHNb_6(O_2)O_{16}^{-2}$	460.212	460.226	64.34
$TMAHNb_6(O_2)_2O_{15}^{-2}$	468.210	468.223	84.04
$TMAHNb_6(O_2)_3O_{14}^{-2}$	476.207	476.221	60.36
$TMA_2Nb_6(O_2)O_{16}^{-2}$	496.755	496.770	13.01
$TMA_2Nb_6(O_2)_2O_{15}^{-2}$	504.753	504.768	35.36
$TMA_2Nb_6(O_2)_3O_{14}^{-2}$	512.750	512.765	37.77
$TMANb_6(O_2)O_{15}^{-1} \cdot 3H_2O$	957.456	957.480	22.10

$TMAH_2Nb_6(O_2)_2O_{15}^{-1} \cdot 2H_2O$	973.451	973.475	58.15
$TMAH_4Nb_6(O_2)_3O_{15}^{-1} \cdot H_2O$	989.446	989.470	51.19
$TMA_2HNb_6(O_2)O_{16}^{-1} \cdot 2H_2O$	1030.542	1030.570	47.92
$TMA_{14}Nb_4O_{18}^{-2} \cdot 21H_2O$	1037.532	1037.557	15.59
$TMA_2H_3Nb_6(O_2)_2O_{16}^{-1} \cdot H_2O$	**1046.537**	**1046.565**	**100**
$TMA_2HNb_6(O_2)_3O_{14}^{-1} \cdot 2H_2O$	1062.533	1062.559	81.32
$TMA_2HNb_6(O_2)_4O_{13}^{-1} \cdot 2H_2O$	1078.528	1078.554	13.67
$TMA_3H_2Nb_6(O_2)_2O_{16}^{-1} \cdot H_2O$	1119.625	1119.654	35.60
$TMA_3Nb_6(O_2)_3O_{14}^{-1} \cdot 2H_2O$	1135.621	1135.649	31.16
$TMA_3Nb_6(O_2)_5O_{12}^{-1} \cdot H_2O$	1149.628	1149.628	10.01
$TMA_3H_2Nb_6(O_2)_6O_{12}^{-1}$	1165.630	1165.623	15.77
$TMA_3Nb_6(O_2)_7O_{10}^{-1} \cdot H_2O$	1181.624	1181.618	13.11
$TMA_4HNb_6(O_2)_6O_{12}^{-1}$	1238.717	1238.712	11.70
$TMA_4HNb_6(O_2)_7O_{11}^{-1}$	1254.711	1254.707	13.79

Table B.10. All species identified by ESI-MS for tri-peroxylated hexaniobate.

Tri-peroxylated hexaniobate reaction solutions			
Species	**Experimental m/z**	**Calculated m/z**	**Relative Abundance (%)**
$Nb_3O_8^{-1}$	406.667	406.678	44.52
$TMA_6H_4Nb_2O_{11}^{-2} \cdot 2H_2O$	423.164	423.196	13.36
$TMAHNb_6(O_2)O_{16}^{-2}$	460.212	460.226	32.64
$TMAHNb_6(O_2)_2O_{15}^{-2}$	468.210	468.223	62.50
$TMAHNb_6(O_2)_3O_{14}^{-2}$	**476.206**	**476.221**	**100**
$TMAHNb_6(O_2)_4O_{13}^{-2}$	484.204	484.218	44.12
$TMA_2Nb_6(O_2)_2O_{15}^{-2}$	504.752	504.768	16.75
$TMA_2Nb_6(O_2)_3O_{14}^{-2}$	512.751	512.765	57.90

$TMA_2Nb_6(O_2)_4O_{13}^{-2}$	520.747	520.763	35.27
$TMA_2Nb_6(O_2)_5O_{12}^{-2}$	528.742	528.760	10.36
$TMA_5Nb_4(O_2)O_{12}^{-1}$	965.975	966.039	26.74
$TMAH_2Nb_6(O_2)_2O_{15}^{-1} \cdot 2H_2O$	973.450	973.475	21.34
$TMAH_4Nb_6(O_2)_3O_{15}^{-1} \cdot H_2O$	989.445	989.470	58.66
$TMA_2H_3Nb_6(O_2)_2O_{16}^{-1} \cdot H_2O$	1046.538	1046.565	39.09
$TMA_{14}H_2Nb_4(O_2)_2O_{17}^{-2} \cdot 20H_2O$	1053.530	1053.552	13.07
$TMA_2HNb_6(O_2)_3O_{14}^{-1} \cdot 2H_2O$	1062.533	1062.559	97.21
$TMA_2HNb_6(O_2)_4O_{13}^{-1} \cdot 2H_2O$	1078.527	1078.554	47.90
$TMA_2HNb_6(O_2)_5O_{12}^{-1} \cdot 2H_2O$	1094.521	1094.549	11.33
$TMA_3H_2Nb_6(O_2)_2O_{16}^{-1} \cdot H_2O$	1119.624	1119.654	15.49
$TMA_3Nb_6(O_2)_3O_{14}^{-1} \cdot 2H_2O$	1135.621	1135.649	40.11
$TMA_3Nb_6(O_2)_4O_{13}^{-1} \cdot 2H_2O$	1151.614	1151.644	21.75
$TMA_3Nb_6(O_2)_7O_{10}^{-1} \cdot H_2O$	1181.623	1181.618	11.53
$TMA_4HNb_6(O_2)_7O_{11}^{-1}$	1254.715	1254.707	10.77

Table B.11. All species identified by ESI-MS for tetra-peroxylated hexaniobate.

Tetra-peroxylated hexaniobate reaction solutions			
Species	**Experimental m/z**	**Calculated m/z**	**Relative Abundance (%)**
$Nb_3O_8^{-1}$	406.667	406.678	61.48
$TMA_6H_4Nb_2O_{11}^{-2} \cdot 2H_2O$	423.166	423.196	17.71
$TMA_2Nb(OH)_8^{-1} \cdot 3H_2O$	431.161	431.154	11.51
$TMAHNb_6(O_2)O_{16}^{-2}$	460.212	460.226	25.68
$TMAHNb_6(O_2)_2O_{15}^{-2}$	468.210	468.223	52.02
$TMAHNb_6(O_2)_3O_{14}^{-2}$	**476.206**	**476.221**	**100**
$TMAHNb_6(O_2)_4O_{13}^{-2}$	484.203	484.218	82.39

$TMANb_6(O_2)_5O_{12}^{-2}$	492.201	492.216	27.40
$TMAH_3Nb_6(O_2)_5O_{13}^{-2}$	501.205	501.221	18.93
$TMA_2Nb_6(O_2)_3O_{14}^{-2}$	512.749	512.765	41.74
$TMA_2Nb_6(O_2)_4O_{13}^{-2}$	520.747	520.763	71.09
$TMA_2Nb_6(O_2)_5O_{12}^{-2}$	528.745	528.760	50.06
$TMA_2Nb_6(O_2)_6O_{11}^{-2}$	536.741	536.758	26.33
$TMA_2H_2Nb_6(O_2)_5O_{13}^{-2}$	537.750	537.765	31.38
$TMA_2H_2Nb_6(O_2)_6O_{12}^{-2}$	545.746	545.763	19.30
$TMAH_4Nb_6(O_2)_3O_{15}^{-1} \cdot H_2O$	989.444	989.470	22.69
$TMAH_6Nb_6(O_2)_4O_{15}^{-1}$	1005.438	1005.465	25.08
$TMANb_6(O_2)_5O_{11}^{-1} \cdot 3H_2O$	1021.432	1021.460	14.52
$TMA_2HNb_6(O_2)_3O_{14}^{-1} \cdot 2H_2O$	1062.532	1062.559	54.49
$TMA_2HNb_6(O_2)_4O_{13}^{-1} \cdot 2H_2O$	1078.527	1078.554	73.68
$TMA_2HNb_6(O_2)_5O_{12}^{-1} \cdot 2H_2O$	1094.521	1094.549	48.15
$TMA_2HNb_6(O_2)_6O_{11}^{-1} \cdot 2H_2O$	1110.516	1110.544	21.23
$TMA_3Nb_6(O_2)_3O_{14}^{-1} \cdot 2H_2O$	1135.620	1135.649	31.76
$TMA_3Nb_6(O_2)_5O_{12}^{-1} \cdot H_2O$	1149.599	1149.628	13.94
$TMA_3Nb_6(O_2)_4O_{13}^{-1} \cdot 2H_2O$	1151.614	1151.644	50.52
$TMA_3H_2Nb_6(O_2)_5O_{13}^{-1} \cdot H_2O$	1167.608	1167.638	41.84
$TMA_3Nb_6(O_2)_7O_{10}^{-1} \cdot H_2O$	1181.617	1181.618	11.59
$TMA_3H_2Nb_6(O_2)_6O_{12}^{-1} \cdot H_2O$	1183.604	1183.633	22.85
$TMA_4HNb_6(O_2)_8O_{10}^{-1}$	1270.705	1270.702	13.46
$TMA_4HNb_6(O_2)_9O_9^{-1}$	1286.700	1286.697	12.56

Table B.12. All species identified by ESI-MS for penta-peroxylated hexaniobate.

Penta-peroxylated hexaniobate reaction solutions			
Species	**Experimental**	**Calculated**	**Relative**

	m/z	m/z	Abundance (%)
$Nb_3O_8^{-1}$	406.665	406.678	54.20
$TMA_6H_4Nb_2O_{11}^{-2} \cdot 2H_2O$	423.163	423.196	23.00
$TMAHNb_6(O_2)O_{16}^{-2}$	460.212	460.226	20.78
$TMAHNb_6(O_2)_2O_{15}^{-2}$	468.209	468.223	52.36
$TMAHNb_6(O_2)_3O_{14}^{-2}$	476.206	476.221	80.09
$TMAHNb_6(O_2)_4O_{13}^{-2}$	**484.203**	**484.218**	**100**
$TMANb_6(O_2)_5O_{12}^{-2}$	492.200	492.216	38.33
$TMAHNb_6(O_2)_6O_{11}^{-2}$	500.197	500.213	20.28
$TMAH_3Nb_6(O_2)_5O_{13}^{-2}$	501.204	501.221	28.42
$TMAH_3Nb_6(O_2)_6O_{12}^{-2}$	509.203	509.218	31.71
$TMA_2Nb_6(O_2)_3O_{14}^{-2}$	512.750	512.765	19.02
$TMA_2Nb_6(O_2)_4O_{13}^{-2}$	520.747	520.765	54.05
$TMA_2Nb_6(O_2)_5O_{12}^{-2}$	528.744	528.763	65.25
$TMA_2Nb_6(O_2)_6O_{11}^{-2}$	536.741	536.758	74.53
$TMA_2H_2Nb_6(O_2)_5O_{13}^{-2}$	537.748	537.765	44.31
$TMA_2H_2Nb_6(O_2)_6O_{12}^{-2}$	545.746	545.763	66.51
$TMANb_6(O_2)_4O_{12}^{-1} \cdot 3H_2O$	1005.438	1005.465	13.63
$TMANb_6(O_2)_5O_{11}^{-1} \cdot 3H_2O$	1021.433	1021.460	17.91
$TMANb_6(O_2)_6O_{10}^{-1} \cdot 3H_2O$	1037.426	1037.455	15.34
$TMA_2HNb_6(O_2)_3O_{14}^{-1} \cdot 2H_2O$	1062.532	1062.559	13.23
$TMA_2HNb_6(O_2)_4O_{13}^{-1} \cdot 2H_2O$	1078.526	1078.554	33.66
$TMA_2HNb_6(O_2)_5O_{12}^{-1} \cdot 2H_2O$	1094.521	1094.549	51.53
$TMA_2HNb_6(O_2)_6O_{11}^{-1} \cdot 2H_2O$	1110.516	1110.544	51.90
$TMA_3Nb_6(O_2)_5O_{12}^{-1} \cdot H_2O$	1149.598	1149.628	17.62
$TMA_3Nb_6(O_2)_4O_{13}^{-1} \cdot 2H_2O$	1151.613	1151.644	20.22
$TMA_3H_2Nb_6(O_2)_6O_{12}^{-1}$	1165.595	1165.623	13.24

$TMA_3H_2Nb_6(O_2)_5O_{13}^{-1} \cdot H_2O$	1167.609	1167.638	39.67
$TMA_3H_2Nb_6(O_2)_6O_{12}^{-1} \cdot H_2O$	1183.604	1183.633	54.70

Table B.13. All species identified by ESI-MS for hexa-peroxylated hexaniobate.

Hexa-peroxylated hexaniobate reaction solutions			
Species	**Experimental m/z**	**Calculated m/z**	**Relative Abundance (%)**
$Nb_3O_8^{-1}$	406.667	406.678	51.57
$TMA_6H_4Nb_2O_{11}^{-2} \cdot 2H_2O$	423.165	423.196	16.16
$TMAHNb_6(O_2)O_{16}^{-2}$	460.214	460.226	10.10
$TMAHNb_6(O_2)_2O_{15}^{-2}$	468.208	468.223	43.82
$TMAHNb_6(O_2)_3O_{14}^{-2}$	476.207	476.221	34.71
$TMAHNb_6(O_2)_4O_{13}^{-2}$	484.204	484.218	81.34
$TMANb_6(O_2)_5O_{12}^{-2}$	492.200	492.216	21.38
$TMAHNb_6(O_2)_6O_{11}^{-2}$	500.197	500.213	22.63
$TMAH_3Nb_6(O_2)_5O_{13}^{-2}$	501.205	501.221	15.75
$TMAH_3Nb_6(O_2)_6O_{12}^{-2}$	509.203	509.218	40.72
$TMA_2Nb_6(O_2)_4O_{13}^{-2}$	520.745	520.765	18.06
$TMA_2Nb_6(O_2)_5O_{12}^{-2}$	528.744	528.763	28.51
$TMA_2Nb_6(O_2)_6O_{11}^{-2}$	536.742	536.758	70.68
$TMA_2H_2Nb_6(O_2)_5O_{13}^{-2}$	537.748	537.765	21.41
$TMA_2H_2Nb_6(O_2)_6O_{12}^{-2}$	545.747	545.763	58.20
$TMANb_6(O_2)_5O_{11}^{-1} \cdot 3H_2O$	1021.431	1021.460	17.76
$TMANb_6(O_2)_6O_{10}^{-1} \cdot 3H_2O$	1037.427	1037.455	36.33
$TMA_2HNb_6(O_2)_4O_{13}^{-1} \cdot 2H_2O$	1078.527	1078.554	12.10
$TMA_2HNb_6(O_2)_5O_{12}^{-1} \cdot 2H_2O$	1094.520	1094.549	38.02
$TMA_2HNb_6(O_2)_6O_{11}^{-1} \cdot 2H_2O$	**1110.517**	**1110.544**	**100**

$TMA_3H_2Nb_6(O_2)_6O_{12}^{-1}$	1165.593	1165.623	11.98
$TMA_3H_2Nb_6(O_2)_5O_{13}^{-1} \cdot H_2O$	1167.608	1167.638	16.92
$TMA_3H_2Nb_6(O_2)_6O_{12}^{-1} \cdot H_2O$	1183.604	1183.633	59.89

APPENDIX C: SUPPORTING INFORMATION FOR CHAPTER 7

Table C.1. Solutions prepared for SWAXS study.

15mM Samples		50mM Samples	
$K_8[Nb_6O_{19}]$ in water	$K_8[Ta_6O_{19}]$ in water	$K_8[Nb_6O_{19}]$ in water	$K_8[Ta_6O_{19}]$ in water
$K_8[Nb_6O_{19}]$ in 10% methanol	$K_8[Ta_6O_{19}]$ in 10% methanol	$K_8[Nb_6O_{19}]$ in 10% methanol	$K_8[Ta_6O_{19}]$ in 10% methanol
$K_8[Nb_6O_{19}]$ in 20% methanol	$K_8[Ta_6O_{19}]$ in 20% methanol	$K_8[Nb_6O_{19}]$ in 20% methanol	
$Rb_8[Nb_6O_{19}]$ in water	$Rb_8[Ta_6O_{19}]$ in water	$Rb_8[Nb_6O_{19}]$ in water	$Rb_8[Ta_6O_{19}]$ in water
$Rb_8[Nb_6O_{19}]$ in 10% methanol	$Rb_8[Ta_6O_{19}]$ in 10% methanol	$Rb_8[Nb_6O_{19}]$ in 10% methanol	$Rb_8[Ta_6O_{19}]$ in 10% methanol
$Rb_8[Nb_6O_{19}]$ in 20% methanol	$Rb_8[Ta_6O_{19}]$ in 20% methanol	$Rb_8[Nb_6O_{19}]$ in 20% methanol	$Rb_8[Ta_6O_{19}]$ in 20% methanol
$Rb_8[Nb_6O_{19}]$ in 40% methanol			
$Cs_8[Nb_6O_{19}]$ in water	$Cs_8[Ta_6O_{19}]$ in water	$Cs_8[Nb_6O_{19}]$ in water	$Cs_8[Ta_6O_{19}]$ in water
$Cs_8[Nb_6O_{19}]$ in 10% methanol	$Cs_8[Ta_6O_{19}]$ in 10% methanol	$Cs_8[Nb_6O_{19}]$ in 10% methanol	$Cs_8[Ta_6O_{19}]$ in 10% methanol
$Cs_8[Nb_6O_{19}]$ in 20% methanol	$Cs_8[Ta_6O_{19}]$ in 20% methanol	$Cs_8[Nb_6O_{19}]$ in 20% methanol	$Cs_8[Ta_6O_{19}]$ in 20% methanol
$Cs_8[Nb_6O_{19}]$ in 40% methanol			
$TMA_5H_3[Nb_6O_{19}]$ in water	$TMA_6H_2[Ta_6O_{19}]$ in water	$TMA_5H_3[Nb_6O_{19}]$ in water	$TMA_6H_2[Ta_6O_{19}]$ in water
$TMA_5H_3[Nb_6O_{19}]$ in 10% methanol	$TMA_6H_2[Ta_6O_{19}]$ in 10% methanol	$TMA_5H_3[Nb_6O_{19}]$ in 10% methanol	$TMA_6H_2[Ta_6O_{19}]$ in 10% methanol
$TMA_5H_3[Nb_6O_{19}]$ in 20% methanol	$TMA_6H_2[Ta_6O_{19}]$ in 20% methanol	$TMA_5H_3[Nb_6O_{19}]$ in 20% methanol	$TMA_6H_2[Ta_6O_{19}]$ in 20% methanol
$TMA_5H_3[Nb_6O_{19}]$ in 40% methanol	$TMA_6H_2[Ta_6O_{19}]$ in 40% methanol	$TMA_5H_3[Nb_6O_{19}]$ in 40% methanol	$TMA_6H_2[Ta_6O_{19}]$ in 40% methanol

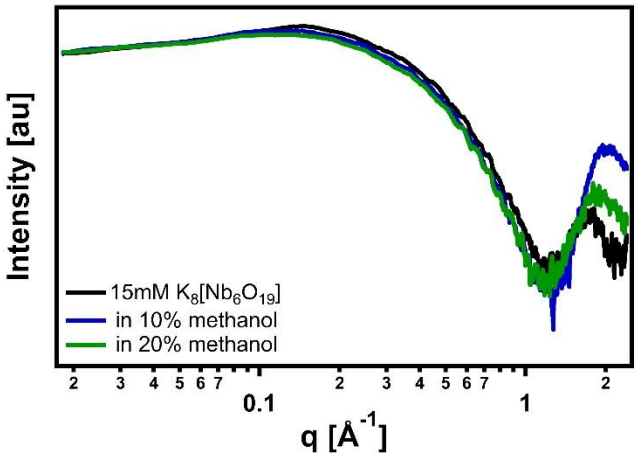

Figure C.1. Log(Intensity) vs log(q) scattering plot for 15 mM $K_8[Nb_6O_{19}]$ in water, 10% methanol, and 20% methanol solutions.

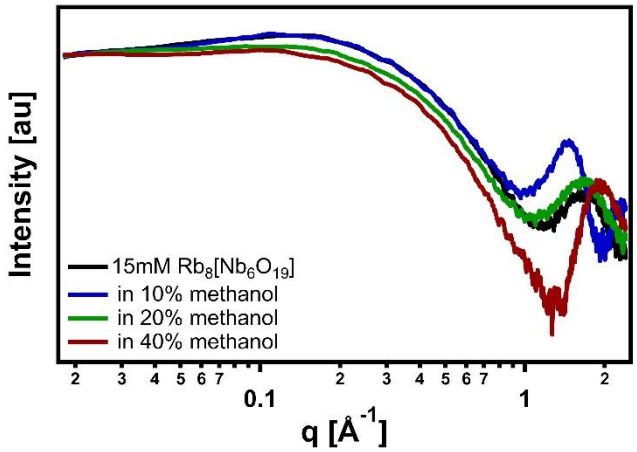

Figure C.2. Log(Intensity) vs log(q) scattering plot for 15 mM $Rb_8[Nb_6O_{19}]$ in water, 10% methanol, 20% methanol, and 40% methanol solutions.

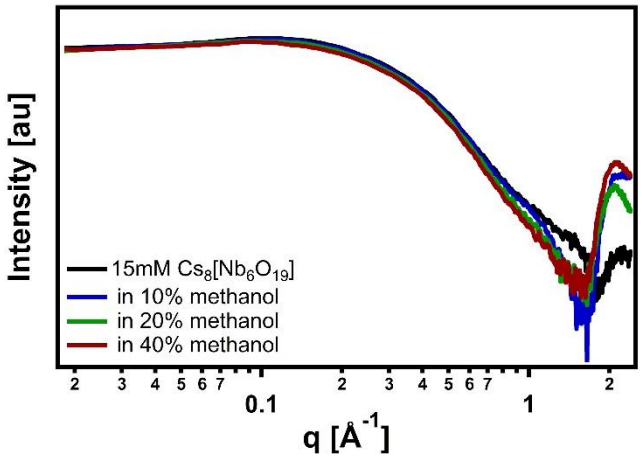

Figure C.3. Log(Intensity) vs log(q) scattering plot for 15 mM $Cs_8[Nb_6O_{19}]$ in water, 10% methanol, 20% methanol, and 40% methanol solutions.

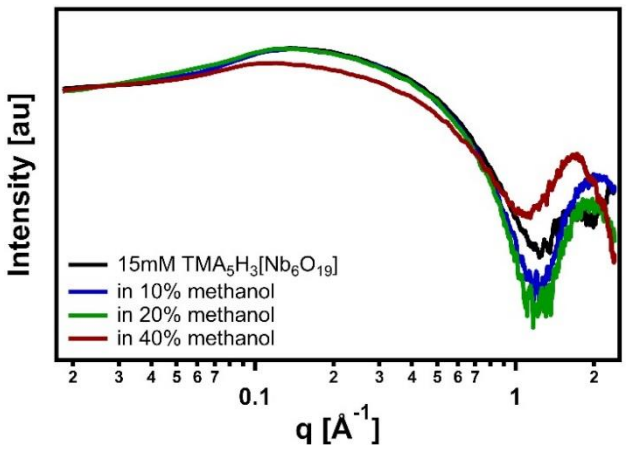

Figure C.4. Log(Intensity) vs log(q) scattering plot for 15 mM $TMA_5H_3[Nb_6O_{19}]$ in water, 10% methanol, 20% methanol, and 40% methanol solutions.

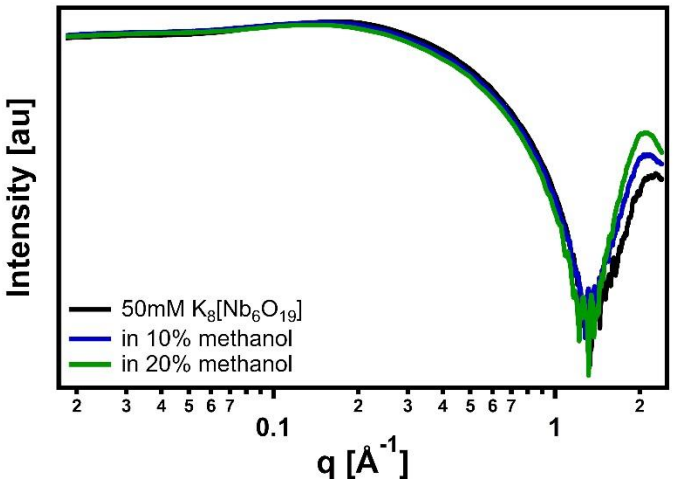

Figure C.5. Log(Intensity) vs log(q) scattering plot for 50 mM $K_8[Nb_6O_{19}]$ in water, 10% methanol, and 20% methanol solutions.

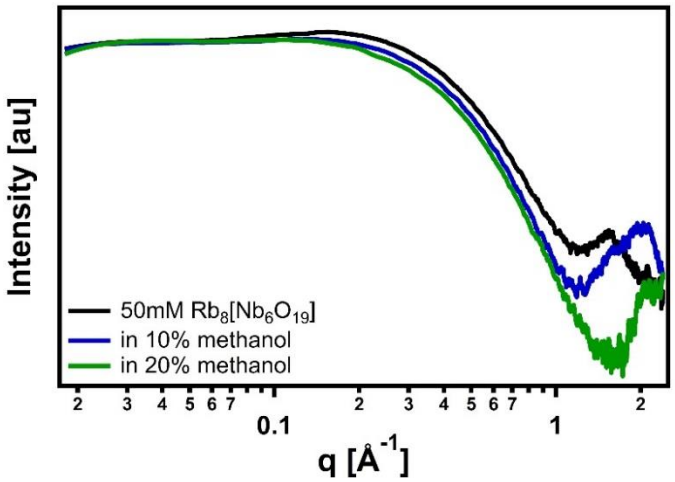

Figure C.6. Log(Intensity) vs log(q) scattering plot for 50 mM $Rb_8[Nb_6O_{19}]$ in water, 10% methanol, and 20% methanol solutions.

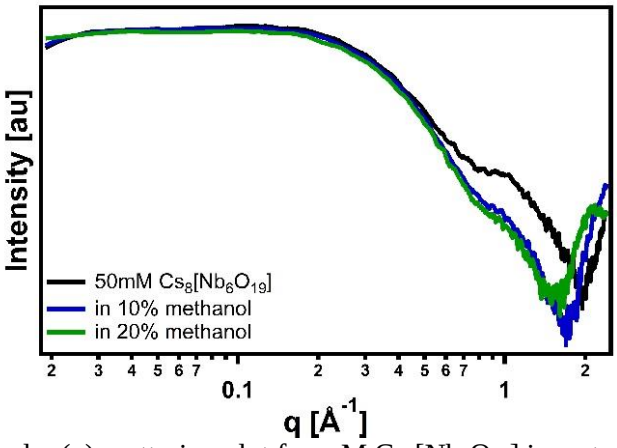

Figure C.7. Log(Intensity) vs log(q) scattering plot for mM $Cs_8[Nb_6O_{19}]$ in water, 10% methanol, and 20% methanol solutions.

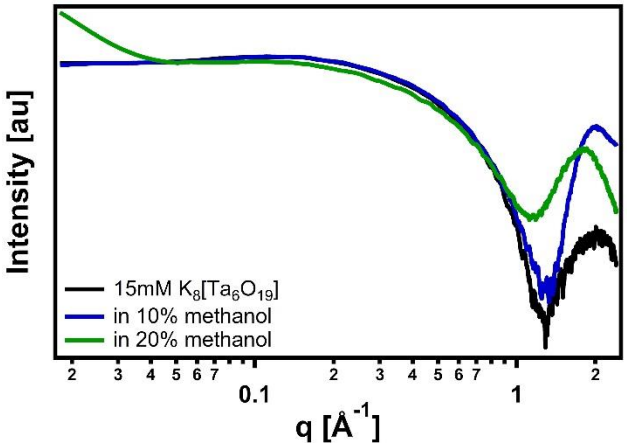

Figure C.8. Log(Intensity) vs log(q) scattering plot for 15 mM $K_8[Ta_6O_{19}]$ in water, 10% methanol, and 20% methanol solutions.

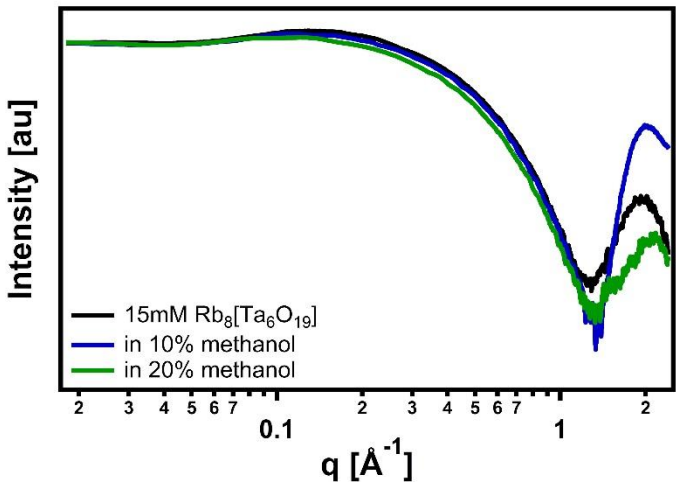

Figure C.9. Log(Intensity) vs log(q) scattering plot for 15 mM $Rb_8[Ta_6O_{19}]$ in water, 10% methanol, and 20% methanol solutions.

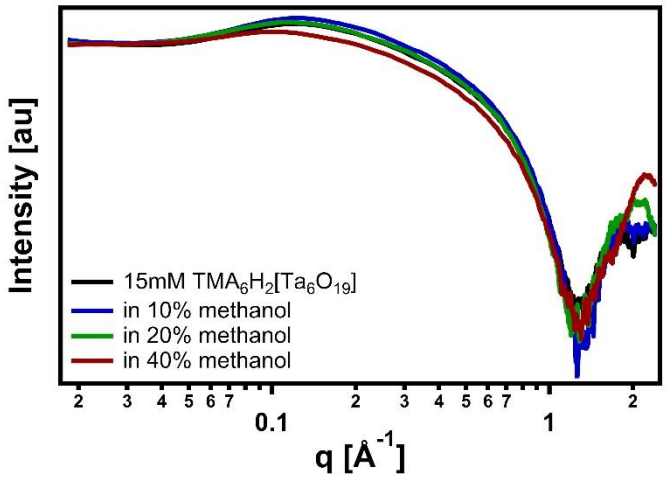

Figure C.10. Log(Intensity) vs log(q) scattering plot for 15 mM $TMA_6H_2[Ta_6O_{19}]$ in water, 10% methanol, 20% methanol, and 40% methanol solutions.

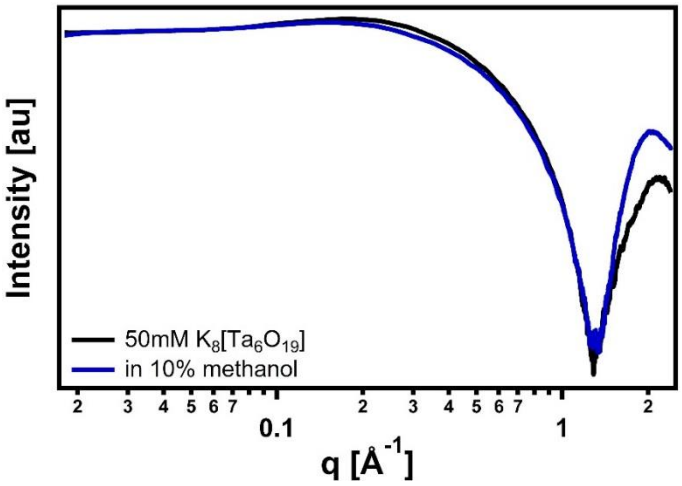

Figure C.11. Log(Intensity) vs log(q) scattering plot for 50 mM $K_8[Ta_6O_{19}]$ in water, and 10% methanol solution.

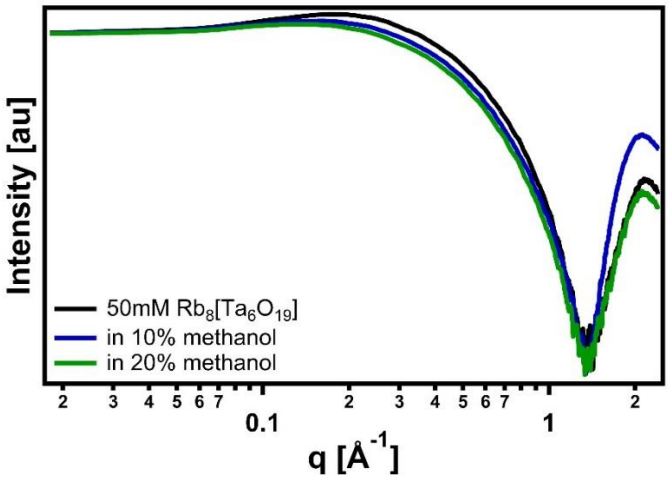

Figure C.12. Log(Intensity) vs log(q) scattering plot for 50 mM $Rb_8[Ta_6O_{19}]$ in water, 10% methanol, and 20% methanol solutions.

Table C.2. Structure factor and radius from Modeling II and radius from Guinier approximation of SAXS data for 15mM samples of $A_8[Nb_6O_{19}]$ (A = K, Rb, Cs, TMA)

15mM Samples	Structure Factor		Radius (Å)
	# Nearest Neighbors	Distance (Å)	Guinier
$K_8[Nb_6O_{19}]$ in water	0.4	35.8	4.5
$K_8[Nb_6O_{19}]$ in 10% methanol	0.3	40.6	4.7
$K_8[Nb_6O_{19}]$ in 20% methanol	0.3	41.8	5.0
$Rb_8[Nb_6O_{19}]$ in water	0.3	37.6	4.7
$Rb_8[Nb_6O_{19}]$ in 10% methanol	0.3	38.1	5.1
$Rb_8[Nb_6O_{19}]$ in 20% methanol	0.1	38.4	5.1
$Rb_8[Nb_6O_{19}]$ in 40% methanol	0.1	48.2	5.1
$Cs_8[Nb_6O_{19}]$ in water	0.3	40.8	5.4
$Cs_8[Nb_6O_{19}]$ in 10% methanol	0.1	40.4	5.3
$Cs_8[Nb_6O_{19}]$ in 20% methanol	0.1	45.3	5.4
$Cs_8[Nb_6O_{19}]$ in 40% methanol	0.1	45.4	5.5
$TMA_5H_3[Nb_6O_{19}]$ in water	0.8	37.6	4.0
$TMA_5H_3[Nb_6O_{19}]$ in 10% methanol	0.7	38.6	4.0
$TMA_5H_3[Nb_6O_{19}]$ in 20% methanol	0.6	39.1	4.1
$TMA_5H_3[Nb_6O_{19}]$ in 40% methanol	0.4	45.7	4.2

Table C.3. Structure factor and radius from Modeling II and radius from Guinier approximation of SAXS data for 15mM samples of $A_8[Ta_6O_{19}]$ (A = K, Rb, Cs, TMA)

15mM Samples	Structure Factor		Radius (Å)
	# Nearest Neighbors	Distance (Å)	Guinier
$K_8[Ta_6O_{19}]$ in water	0.2	42.3	4.2
$K_8[Ta_6O_{19}]$ in 10% methanol	0.2	40.5	4.1
$K_8[Ta_6O_{19}]$ in 20% methanol	0.04	52.3	4.2
$Rb_8[Ta_6O_{19}]$ in water	0.3	35.1	4.5
$Rb_8[Ta_6O_{19}]$ in 10% methanol	0.3	38.3	4.5
$Rb_8[Ta_6O_{19}]$ in 20% methanol	0.2	45.8	4.5
$Rb_8[Ta_6O_{19}]$ in 40% methanol	na	na	na
$Cs_8[Ta_6O_{19}]$ in water	0.3	35.4	4.7
$Cs_8[Ta_6O_{19}]$ in 10% methanol	0.1	40.6	4.8
$Cs_8[Ta_6O_{19}]$ in 20% methanol	--	--	4.8
$Cs_8[Ta_6O_{19}]_9$ in 40% methanol	--	--	na
$TMA_6H_2[Ta_6O_{19}]$ in water	0.5	46.2	3.8
$TMA_6H_2[Ta_6O_{19}]$ in 10% methanol	0.6	45.6	3.9
$TMA_6H_2[Ta_6O_{19}]$ in 20% methanol	0.5	47.8	3.9
$TMA_6H_2[Ta_6O_{19}]_9$ in 40% methanol	0.3	56.8	3.9

na: samples were not suitable for SAXS data collection either due to insolubility or high x-ray absorption.

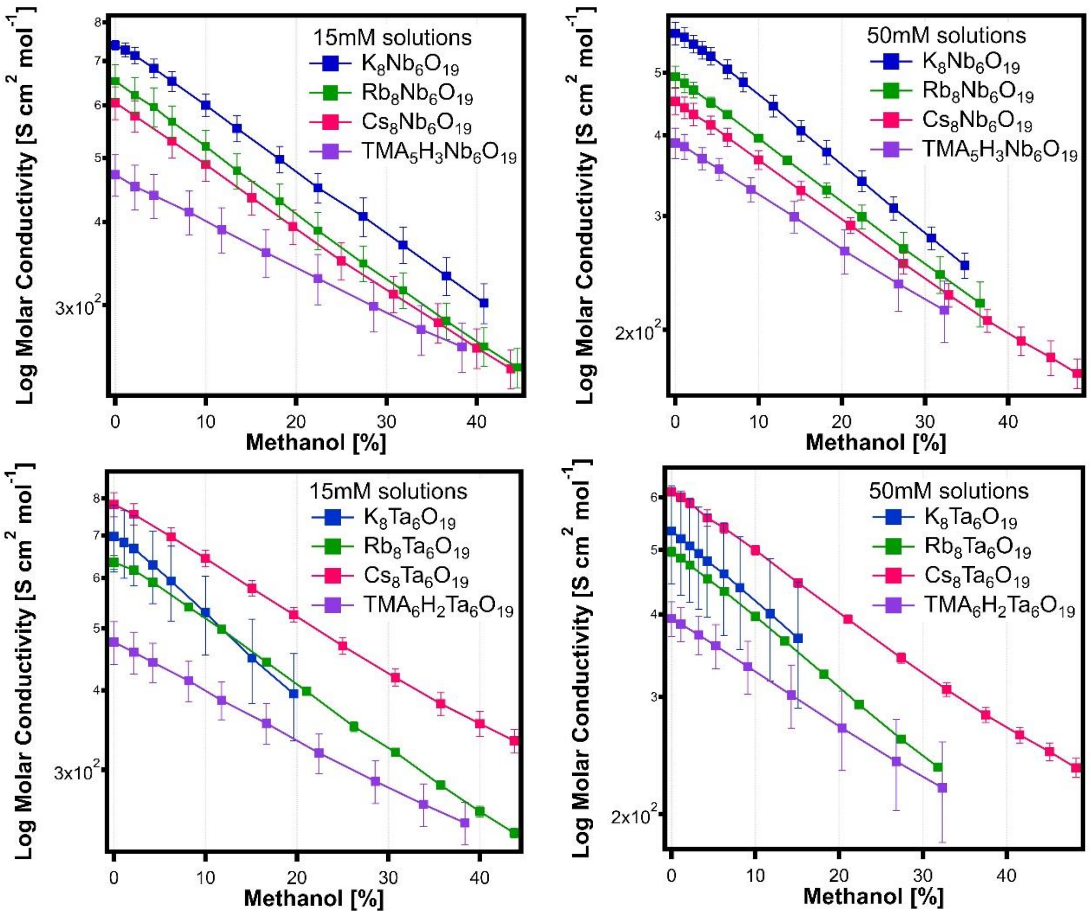

Figure C.13. Log of molar conductivity vs. percentage of methanol for 15 and 50 mM $A_8[Nb_6O_{19}]$ on the top and $A_8[Ta_6O_{19}]$ on the bottom (A = K, Rb, Cs, TMA). These data were used in the determination of slope.

Table C.4. Slopes of 15 and 50 mM $A_8[Nb_6O_{19}]$ and $A_8[Ta_6O_{19}]$ (A = K, Rb, Cs, TMA) determined from log-linear plots.

Ta_6O_{19}		**Nb_6O_{19}**	
15mM	**Slope**	**15mM**	**Slope**
K	-15.9	K	-11
Rb	-9.4	Rb	-9.3
Cs	-10.5	Cs	-8.4
TMA	-6	TMA	-5.7
50mM		**50mM**	
K	-11	K	-9.7
Rb	-8.4	Rb	-7.6
Cs	-8	Cs	-5.9
TMA	-5.5	TMA	-5.6

Table C.5. Conductivity of $K_8[Nb_6O_{19}]$ nH_2O solutions

.015M					.05M				
Concentration (mol/L)	% Methanol	Average Conductivity (mS/cm)	Standard Deviation	Calculated Conductivity (mS/cm)	Concentration (mol/L)	% Methanol	Average Conductivity (mS/cm)	Standard Deviation	Calculated Conductivity (mS/cm)
0.015	0	11.09	0.18	28.21	0.05	0	28.77	1.15	94.03
0.0148	1.1	10.78	0.26	27.90	0.0495	1.1	28.06	1.02	93.00
0.0147	2.2	10.47	0.31	27.60	0.0489	2.2	27.08	0.84	91.99
0.0144	4.3	9.80	0.32	27.01	0.0484	3.2	26.22	0.81	91.00
0.0141	6.3	9.17	0.31	26.45	0.0479	4.3	25.39	0.79	90.03
0.0135	10	8.10	0.31	25.39	0.0469	6.3	23.74	0.81	88.15
0.0130	13.5	7.19	0.33	24.41	0.0459	8.2	22.19	0.74	86.35
0.0123	18.2	6.10	0.28	23.08	0.0441	11.8	19.59	0.76	82.97
0.0116	22.4	5.24	0.27	21.89	0.0425	15.1	17.27	0.62	79.84
0.0109	27.4	4.44	0.30	20.47	0.0409	18.2	15.43	0.66	76.93
0.0102	31.8	3.78	0.24	19.23	0.0388	22.4	13.17	0.49	72.95
0.0095	36.6	3.15	0.21	17.88	0.0369	26.2	11.39	0.48	69.37
0.0089	40.8	2.68	0.19	16.70	0.0346	30.8	9.61	0.39	65.10
					0.0326	34.8	8.21	0.37	61.32

Table C.6. Conductivity of $Rb_8[Nb_6O_{19}]$ nH_2O solutions

.015M					.05M				
Concentration (mol/L)	% Methanol	Average Conductivity (mS/cm)	Standard Deviation	Calculated Conductivity (mS/cm)	Concentration (mol/L)	% Methanol	Average Conductivity (mS/cm)	Standard Deviation	Calculated Conductivity (mS/cm)
0.015	0	9.79	0.58	27.60	0.05	0	24.65	0.93	91.99
0.0147	2.2	9.12	0.57	27.00	0.0495	1.1	23.82	0.78	90.98
0.0144	4.3	8.56	0.58	26.42	0.0489	2.2	23.00	0.64	89.99
0.0141	6.3	7.97	0.45	25.87	0.0479	4.3	21.53	0.39	88.08
0.0135	10	7.02	0.41	24.84	0.0469	6.3	20.2	0.28	86.24
0.0130	13.5	6.21	0.38	23.88	0.045	10	17.82	0.12	82.79
0.0123	18.2	5.28	0.32	22.58	0.0433	13.5	15.84	0.20	79.61
0.0116	22.4	4.52	0.29	21.41	0.0409	18.2	13.47	0.36	75.27
0.0109	27.4	3.77	0.23	20.03	0.0388	22.4	11.61	0.49	71.37
0.0102	31.8	3.23	0.20	18.82	0.0363	27.4	9.70	0.58	66.77
0.0095	36.6	2.70	0.17	17.49	0.0341	31.8	8.30	0.54	62.72
0.0089	40.8	2.31	0.15	16.34	0.0317	36.6	6.97	0.56	58.31
0.0083	44.4	2.01	0.14	15.33					

Table C.7. Conductivity of $Cs_8[Nb_6O_{19}]\ nH_2O$ solutions

.015M					.05M				
Concentration (mol/L)	% Methanol	Average Conductivity (mS/cm)	Standard Deviation	Calculated Conductivity (mS/cm)	Concentration (mol/L)	% Methanol	Average Conductivity (mS/cm)	Standard Deviation	Calculated Conductivity (mS/cm)
0.015	0	9.08	0.52	27.05	0.05	0	22.58	1.06	90.17
0.0147	2.2	8.48	0.46	26.46	0.0495	1.1	21.84	0.86	89.17
0.0141	6.3	7.45	0.42	25.36	0.0489	2.2	21.08	0.84	88.21
0.0135	10	6.60	0.38	24.34	0.0479	4.3	19.88	0.64	86.33
0.0127	15.1	5.54	0.32	22.97	0.0469	6.3	18.63	0.60	84.53
0.0121	19.6	4.75	0.28	21.74	0.045	10	16.50	0.55	81.15
0.0113	25	3.93	0.26	20.29	0.0425	15.1	13.95	0.46	76.56
0.0104	30.8	3.23	0.20	18.73	0.0395	21.1	11.46	0.33	71.18
0.0096	35.7	2.72	0.19	17.39	0.0363	27.4	9.20	0.34	65.44
0.009	40	2.32	0.16	16.23	0.0336	32.8	7.61	0.32	60.56
0.0084	43.8	2.03	0.13	15.22	0.0313	37.5	6.46	0.27	56.35
					0.0292	41.6	5.62	0.29	52.69
					0.0274	45.1	4.97	0.31	49.48
					0.0259	48.3	4.43	0.24	46.64

Table C.8. Conductivity of $TMA_5H_3[Nb_6O_{19}]\ nH_2O$ solutions

.015M					.05M				
Concentration (mol/L)	% Methanol	Average Conductivity (mS/cm)	Standard Deviation	Calculated Conductivity (mS/cm)	Concentration (mol/L)	% Methanol	Average Conductivity (mS/cm)	Standard Deviation	Calculated Conductivity (mS/cm)
0.015	0	6.94	0.51	23.69	0.05	0	19.47	1.04	78.95
0.0147	2.2	6.56	0.51	23.17	0.0496	1.1	19.06	0.83	78.30
0.0144	4.3	6.16	0.48	22.68	0.0488	3.2	17.97	0.71	77.03
0.0138	8.2	5.54	0.43	21.75	0.048	5.3	17.02	0.67	75.80
0.0132	11.8	5.00	0.41	20.90	0.0465	9.1	15.35	0.67	73.45
0.0125	16.7	4.33	0.37	19.74	0.0444	14.3	13.30	0.74	70.18
0.0116	22.4	3.66	0.33	18.38	0.0420	20.4	11.11	0.88	66.25
0.0107	28.6	3.05	0.27	16.92	0.0392	26.8	9.24	0.86	61.92
0.0099	33.8	2.61	0.24	15.67	0.0368	32.3	7.90	0.86	58.13
0.0092	38.4	2.29	0.20	14.60					

Table C.9. Conductivity of $K_8[Ta_6O_{19}]$ nH_2O solutions

.015M					.05M				
Concentration (mol/L)	% Methanol	Average Conductivity (mS/cm)	Standard Deviation	Calculated Conductivity (mS/cm)	Concentration (mol/L)	% Methanol	Average Conductivity (mS/cm)	Standard Deviation	Calculated Conductivity (mS/cm)
0.015	0	10.46	1.25	28.21	0.05	0	26.71	4.50	94.03
0.0148	1.1	10.12	1.23	27.90	0.0495	1.1	25.72	4.58	93.00
0.0147	2.2	9.79	1.23	27.60	0.0489	2.2	24.80	4.42	91.99
0.0145	4.3	9.13	1.19	27.30	0.0484	3.2	23.90	4.19	91.00
0.0144	6.3	8.53	1.16	27.01	0.0479	4.3	23.03	4.08	90.03
0.0141	10	7.45	1.05	26.45	0.0469	6.3	21.57	4.16	88.15
0.0138	15.1	6.19	0.94	25.91	0.0459	8.2	20.15	3.90	86.35
0.0132	19.6	5.23	0.82	24.89	0.0441	11.8	17.69	3.70	82.97
					0.0425	15.1	15.62	3.37	79.84

Table C.10. Conductivity of $Rb_8[Ta_6O_{19}]$ nH_2O solutions

.015M					.05M				
Concentration (mol/L)	% Methanol	Average Conductivity (mS/cm)	Standard Deviation	Calculated Conductivity (mS/cm)	Concentration (mol/L)	% Methanol	Average Conductivity (mS/cm)	Standard Deviation	Calculated Conductivity (mS/cm)
0.0150	0.0	9.52	0.24	27.60	0.0500	0.0	24.85	0.39	91.99
0.0147	2.2	9.06	0.07	27.00	0.0495	1.1	24.04	0.24	90.98
0.0144	4.3	8.48	0.04	26.42	0.0489	2.2	23.20	0.14	89.99
0.0138	8.2	7.44	0.03	25.35	0.0479	4.3	21.66	0.12	88.08
0.0132	11.8	6.60	0.09	24.35	0.0469	6.3	20.30	0.07	86.24
0.0125	16.7	5.53	0.08	23.00	0.0450	10.0	17.87	0.08	82.79
0.0118	21.1	4.72	0.05	21.79	0.0433	13.5	15.78	0.08	79.61
0.0111	26.2	3.88	0.07	20.36	0.0409	18.2	13.29	0.09	75.27
0.0104	30.8	3.32	0.04	19.11	0.0388	22.4	11.34	0.11	71.37
0.0096	35.7	2.74	0.04	17.74	0.0363	27.4	9.41	0.14	66.77
0.0090	40.0	2.32	0.05	16.56	0.0341	31.8	8.02	0.08	62.72
0.0084	43.8	2.01	0.04	15.52					

Table C.11. Conductivity of $Cs_8[Ta_6O_{19}]\ nH_2O$ solutions

.015M					.05M				
Concentration (mol/L)	% Methanol	Average Conductivity (mS/cm)	Standard Deviation	Calculated Conductivity (mS/cm)	Concentration (mol/L)	% Methanol	Average Conductivity (mS/cm)	Standard Deviation	Calculated Conductivity (mS/cm)
0.015	0	11.74	0.51	27.05	0.05	0	30.6	0.17	90.17
0.0147	2.2	11.08	0.43	26.46	0.0495	1.1	29.71	0.44	89.17
0.0141	6.3	9.79	0.33	25.36	0.0489	2.2	28.80	0.48	88.21
0.0135	10	8.7	0.26	24.34	0.0479	4.3	26.76	0.75	86.33
0.0127	15.1	7.36	0.20	22.97	0.0469	6.3	25.31	0.46	84.53
0.0121	19.6	6.34	0.17	21.74	0.045	10	22.50	0.37	81.15
0.0113	25	5.28	0.15	20.29	0.0425	15.1	18.94	0.28	76.56
0.0104	30.8	4.35	0.14	18.73	0.0395	21.1	15.52	0.24	71.18
0.0096	35.7	3.67	0.15	17.39	0.0363	27.4	12.47	0.22	65.44
0.009	40	3.19	0.14	16.23	0.0336	32.8	10.34	0.24	60.56
0.0084	43.8	2.81	0.12	15.22	0.0313	37.5	8.81	0.23	56.35
					0.0292	41.6	7.69	0.21	52.69
					0.0274	45.1	6.81	0.21	49.48
					0.0259	48.3	6.07	0.20	46.64

Table C.12. Conductivity of $TMA_6H_2[Ta_6O_{19}]\ nH_2O$ solutions

.015M					.05M				
Concentration (mol/L)	% Methanol	Average Conductivity (mS/cm)	Standard Deviation	Calculated Conductivity (mS/cm)	Concentration (mol/L)	% Methanol	Average Conductivity (mS/cm)	Standard Deviation	Calculated Conductivity (mS/cm)
0.015	0	7.14	0.55	23.69	0.05	0	19.71	1.18	78.95
0.0147	2.2	6.73	0.51	23.17	0.0496	1.1	19.17	1.13	78.30
0.0144	4.3	6.35	0.45	22.68	0.0488	2.2	18.16	1.22	77.03
0.0138	8.2	5.70	0.42	21.75	0.048	4.3	17.21	1.31	75.80
0.0132	11.8	5.10	0.35	20.90	0.0465	6.3	15.52	1.43	73.45
0.0125	16.7	4.44	0.33	19.74	0.0444	10	13.43	1.47	70.18
0.0116	22.4	3.71	0.26	18.38	0.0420	13.5	11.30	1.55	66.25
0.0107	28.6	3.08	0.24	16.92	0.0392	18.2	9.41	1.48	61.92
0.0099	33.8	2.63	0.20	15.67	0.0368	22.4	8.06	1.39	58.13
0.0092	38.4	2.29	0.17	14.60					

APPENDIX D: SYNTHETIC DETAILS

D.1 HEXANIOBATES

$K_8Nb_6O_{19}\cdot nH_2O$. KOH (100 mL, 4M) is heated to ~90°C. Hydrous Nb_2O_5 (20 g) is slowly added in ~1-2 g scoops. Each addition of Nb_2O_5 should dissolve before adding more. Once all Nb_2O_5 is dissolved, the solution is filtered through a 0.45 µm syringe filter. Evaporate for crystallization. Tip: The solution may be heated longer to reduce the volume which speeds up the crystallization process. Using alcohol for precipitation is also an option. 100% yield

$Rb_8Nb_6O_{19}\cdot nH_2O$. RbOH (100 mL, 2M) is heated to ~90°C. Hydrous Nb_2O_5 (20 g) is slowly added in ~1-2 g scoops. Each addition of Nb_2O_5 should dissolve before adding more. Once all Nb_2O_5 is dissolved, the solution is filtered through a 0.45 µm syringe filter. Evaporate for crystallization. Tip: The solution may be heated longer to reduce the volume which speeds up the crystallization process. Using alcohol for precipitation is also an option. 100% yield

$Cs_8Nb_6O_{19}\cdot nH_2O$. CsOH (100 mL, 2M) is heated to ~90°C. Hydrous Nb_2O_5 (20 g) is slowly added in ~1-2 g scoops. Each addition of Nb_2O_5 should dissolve before adding more. Once all Nb_2O_5 is dissolved, the solution is filtered through a 0.45 µm syringe filter. Evaporate for crystallization. Tip: The solution may be heated longer to reduce the volume which speeds up the crystallization process. Using alcohol for precipitation is also an option. 100% yield

$TMA_5H_3Nb_6O_{19}\cdot nH_2O$. TMAOH (100 mL, 2.8M) is heated to ~90°C. Hydrous Nb_2O_5 (20 g) is slowly added in ~1-2 g scoops. Each addition of Nb_2O_5 should dissolve before adding more. Once all Nb_2O_5 is dissolved, the solution is filtered through a 0.45 µm syringe filter. Precipitate instead of crystallizing. Tip: TMA hexaniobate is very soluble so isopropanol is needed for precipitation. Initial precipitation is very sticky. Repeated washings with isopropanol is necessary. Precipitating in centrifuge tubes is helpful for thorough agitation. 100% yield

D.2 HEXATANTALATES

Hexatantalate syntheses start with peroxotantalate, $Ta(O_2)_4^{3-}$.

$K_3Ta(O_2)_4$. H_2O_2 (40 mL, 30%) is cooled to under 10°C in an ice bath. $TaCl_5$ (4.6 g) is carefully added. Once the solution has cooled again to under 10°C, KOH (35 mL, 4M) is added in small aliquots while keeping the temperature below 20°C. The solution should be clear after all KOH is added. Once the solution has cooled again to under 10°C, sufficient methanol is added for precipitation. The white powder is isolated by vacuum filtration and washed with more methanol. 100% yield

$Rb_3Ta(O_2)_4$. H_2O_2 (40 mL, 30%) is cooled to under 10°C in an ice bath. $TaCl_5$ (4.6 g) is carefully added. Once the solution has cooled again to under 10°C, RbOH (18 mL, 50 wt%) is added in small aliquots while keeping the temperature below 20°C. The solution should be clear after all RbOH is added. Once the solution has cooled again to under 10°C, sufficient methanol is added for precipitation. The white powder is isolated by vacuum filtration and washed with more methanol. 100% yield

$Cs_3Ta(O_2)_4$. H_2O_2 (40 mL, 30%) is cooled to under 10°C in an ice bath. $TaCl_5$ (4.6 g) is carefully added. Once the solution has cooled again to under 10°C, CsOH (35 mL, 4M) is added in small aliquots while keeping the temperature below 20°C. The solution should be clear after all CsOH is added. Once the solution has cooled again to under 10°C, sufficient methanol is added for precipitation. The white powder is isolated by vacuum filtration and washed with more methanol. 100% yield

$(NH_4)_3Ta(O_2)_4$. H_2O_2 (80 mL, 30%) is cooled to under 10°C in an ice bath. $TaCl_5$ (4.8 g) is carefully added. Once the solution has cooled again to under 10°C, NH_4OH (24 mL, 2.8M) is added in small aliquots while keeping the temperature below 20°C. The solution should be clear after all NH_4OH is added. Once the solution has cooled again to under 10°C, sufficient ethanol is added for precipitation. The white powder is isolated by vacuum filtration and washed with more ethanol. 100% yield

$K_8Ta_6O_{19}\cdot nH_2O$. KOH (9.6 g) is dissolved in H_2O (25 mL) with $K_3Ta(O_2)_4$ (4 g). The suspension is heated to reflux until completely dissolved. The solution is cooled

and filtered through a 0.45 µL syringe filter. Evaporate for crystallization. 100% yield. Tip: This solution very quickly absorbs CO_2 and potassium carbonate will crystallize along with the product. Alcohol precipitation is a better option to avoid carbonate impurities.

$Rb_8Ta_6O_{19}\cdot nH_2O$. RbOH (17.6 g) is dissolved in H_2O (25 mL) with $Rb_3Ta(O_2)_4$ (5.3 g). The suspension is heated to reflux until completely dissolved. The solution is cooled and filtered through a 0.45 µL syringe filter. Evaporate for crystallization. 100% yield. Tip: This solution tends to absorb CO_2. The solution can be heated to reduce the volume which speeds up the crystallization process. Alcohol precipitation is also an option to avoid carbonate impurities.

$Cs_8Ta_6O_{19}\cdot nH_2O$. CsOH (26 g) is dissolved in H_2O (25 mL) with $Cs_3Ta(O_2)_4$ (5.5 g). The suspension is heated to reflux until completely dissolved. The solution is cooled and filtered through a 0.45 µL syringe filter. Evaporate for crystallization. 100% yield. Tip: This solution tends to absorb CO_2. The solution can be heated to reduce the volume which speeds up the crystallization process. Alcohol precipitation is also an option to avoid carbonate impurities.

$TMA_6H_2Ta_6O_{19}\cdot nH_2O$. $(NH_4)_3Ta(O_2)_4$ (4.75 g) is added to TMAOH (30 mL, 1.4M). The suspension is heated to reflux for 5 hours. The solution is cooled and filtered through a 0.45 µL syringe filter. Precipitate and thoroughly wash with isopropanol. 30% yield. Tips: The product is very soluble and it takes a lot to precipitate. To increase the yield, continue heating until the volume is reduced by half. Use 50mL centrifuge tubes for precipitation. Add 5-10mL of the solution to the centrifuge tube then fill with isopropanol. After agitating and centrifuging, there will be a separation of a small dense layer which is the product. Discard the top layer and continue washing with isopropanol in this fashion until a non-sticky white powder is obtained. Cooling the solution in the fridge between washes will also help increase the yield.

D.3 PEROXOHEXAMETALATES

$[(CH_3)_4N]_6H_2Ta_6O_{19} \cdot 21H_2O$. A solution of $[(CH_3)_4N]_6H_2Ta_6O_{19} \cdot 21H_2O$ (0.35 g) in H_2O (5 mL) was stirred in an ice bath. H_2O_2 (30%) was added in stoichiometric equivalents from one to six (ie: 16 µL H_2O_2 for monoperoxylated hexatantalate). The final product can be precipitated through addition of isopropanol. Thorough washing with isopropanol yields a hygroscopic, amorphous, white powder.

$[(CH_3)_4N]_5H_3Nb_6O_{19} \cdot 20H_2O$. A solution of $[(CH_3)_4N]_5H_3Nb_6O_{19} \cdot 20H_2O$ (0.25 g) in H_2O (5 mL) was stirred in an ice bath. H_2O_2 (30%) was added in stoichiometric equivalents from one to six (ie: 15 µL H_2O_2 for monoperoxylated hexaniobate). The final product can be precipitated through addition of isopropanol. Thorough washing with isopropanol yields a hygroscopic, amorphous, white powder.